

# Eccentric binaries of compact objects in strong-field gravity

Dissertation

zur Erlangung des akademischen Grades  
doctor rerum naturalium (Dr. rer. nat.)

vorgelegt dem Rat der Physikalisch-Astronomischen Fakultät  
der Friedrich-Schiller-Universität Jena

von Dipl.-Phys. Roman Gold  
geboren am 10.07.1981 in Bad Soden (am Taunus)

Gutachter:

1. Prof. Bernd Brüggemann, FSU Jena
2. Prof. Luis Lehner, Perimeter Institute Waterloo
3. Prof. Deirdre Shoemaker, Georgia Tech Atlanta

Tag der Disputation: 27. September 2011

# Exzentrische Binärsysteme kompakter Objekte im starken Gravitationsfeld

## *Zusammenfassung*

In dieser Arbeit untersuchen wir die Dynamik exzentrischer Binärsysteme kompakter Objekte und die resultierende Gravitationswellenstrahlung im nicht-linearen Regime der Allgemeinen Relativitätstheorie. Hierzu lösen wir die Einsteinschen Feldgleichungen numerisch in einer 3+1 Zerlegung mit der bewegten-Punktur Methode.

Wir konzentrieren uns hierbei auf spezielle Orbits, die im Zusammenhang mit nicht-stabilen Kreisbahnen entstehen, und einen rein relativistischen Effekt des Zweikörperproblems der Allgemeinen Relativitätstheorie darstellen. Diese werden bestimmt durch schnelle, quasi-zirkuläre Umläufe bei kleinen Abständen, gefolgt von langsamen radialen Bewegung auf quasi-elliptischen Trajektorien. Auf Grund der besonderen Gestalt dieser Bahnen werden sie als "Zoom-Whirl-Orbits" bezeichnet.

Wir analysieren, wie sich diese besondere Dynamik in der emittierten Gravitationswellenstrahlung äußert, und inwieweit sich aus Beobachtungen dieser Strahlung auf die Eigenschaften der Orbits schließen lässt.

Im ersten Teil betrachten wir Binärsysteme Schwarzer Löcher. Wir führen eine umfassende Parameterstudie durch, indem wir die Anfangsexzentrizität variieren, und die entstehende Gravitationswellenform berechnen und charakterisieren. Hier befassen wir uns insbesondere mit Aspekten, die nur mit Hilfe nicht-störungstheoretischer Methoden analysiert werden können, und für die astrophysikalische Relevanz dieser Orbits entscheidend sind. Insbesondere implizieren unsere Resultate, dass Zoom-Whirl-Orbits ohne einen hohen Grad von Feinabstimmung erzeugt werden können. Wir finden, dass die Werte der Exzentrizität, für die solche Orbits entstehen, in disjunkten Intervallen zu finden sind, die bis zu niedrigen Werten der Exzentrizität reichen. Weiterhin zeigen wir, dass Wirbeleffekte unmittelbar vor der Verschmelzung der Schwarzen Löcher zu Signalen mit signifikanter Amplitude führen.

Im zweiten Teil untersuchen wir Binärsysteme von Neutronensternen auf exzentrischen Orbits in Allgemeiner Relativitätstheorie, was einen bisher unerforschten Bereich darstellt. Wir untersuchen deren Phänomenologie und studieren die Folgen einer Verschmelzung für die übrigbleibende Sternmaterie. Die verschmolzenen Neutronensterne kollabieren stets zu einem Schwarzen Loch. Währenddessen akkretiert die meiste übriggebliebene Materie auf das Schwarze Loch. Allerdings bleibt im Allgemeinen eine Akkretionsscheibe nicht zu vernachlässigender Masse zurück.

In Abhängigkeit der Anfangsexzentrizität finden wir eine Scheibe von beträchtlicher Masse. Wir sammeln aussagekräftige Anhaltspunkte dafür, dass die Masse der Scheibe für einen erheblichen Bereich von Exzentrizitäten groß genug ist, um einen kurzen Gammastrahlenblitz zu speisen. Weiterhin finden wir starke Gezeiteneffekte, wenn die Neutronensterne sich eng umkreisen, und so eine starke Störung auf ihre innere Dynamik ausüben. Wir demonstrieren, dass dieser Effekt die Gravitationswellenform in charakteristischer Weise modifiziert. Unsere Resultate heben hervor, wie Gravitationswellenformen Hinweise auf die unbekanntere Zustandsgleichung der Kernmaterie im Inneren von Neutronensternen geben können.

# Eccentric binaries of compact objects in strong-field gravity

## *Summary*

In this thesis we study the dynamics as well as the resulting gravitational radiation from eccentric binaries of compact objects in the non-linear regime of General Relativity. For this purpose we solve Einstein's field equation numerically in a 3+1 decomposition using the moving-puncture technique.

We focus our study on very particular orbits, arising as a purely relativistic phenomenon of the two-body problem in General Relativity, which are associated with unstable circular orbits. They are governed by a fast, nearly circular revolution at a short distance followed by a slow, radial motion on a nearly elliptic trajectory. Due to the unique features of their orbital trajectories they are called *zoom-whirl orbits*.

We analyze how the peculiar dynamics manifests itself in the emitted gravitational radiation and to which extent one can infer the orbital properties from observations of the gravitational waves.

In the first part, we consider black hole binaries. We perform a comprehensive parameter study by varying the initial eccentricity, computing and characterizing the resulting gravitational waveforms. We address aspects, which can only be obtained from non-perturbative methods, and which are crucial to the astrophysical relevance of these orbits. In particular, our results imply a fairly low amount of fine-tuning necessary to spot zoom-whirl effects. We find whirl orbits for values of the eccentricities, which fall in disjunct intervals extending to rather low values. Furthermore, we show that whirl effects just before merger cause a signal with significant amplitude.

In the second part, we investigate neutron star binaries on eccentric orbits in full General Relativity, which has not been studied so far. We explore their phenomenology and study the consequences for the matter after the neutron stars have merged. In these evolutions the merged neutron stars sooner or later collapse to form a black hole. During the collapse most of the matter is accreted on to the black hole, but in general a non-negligible amount may form an accretion disk around the merger remnant.

Depending on the initial eccentricity, we find that a disk of substantial mass is left behind. We give strong evidence that the disk masses for a considerable range of eccentricities are generically large enough to power a short gamma-ray burst. Furthermore we find strong tidal interactions, when the neutron stars orbit close to each other, exerting a strong perturbation on the internal dynamics of the stars. We demonstrate that this effect modifies the gravitational waveform in a characteristic way. Our results emphasize the potential of gravitational waves from eccentric neutron star binaries to constrain models for the unknown equation of state of the neutron star material.

# Contents

<b>1</b>	<b>Introduction: General Relativity and Gravitational Wave Astronomy</b>	<b>3</b>
<b>2</b>	<b>The 3+1 decomposition of Einstein's equation and numerical relativity</b>	<b>9</b>
2.1	Splitting space and time . . . . .	9
2.2	Free vs constrained evolution . . . . .	10
2.2.1	3+1 split . . . . .	10
2.2.2	ADM . . . . .	11
2.3	Initial data . . . . .	12
2.3.1	Bowen-York solution . . . . .	13
2.3.2	Puncture Initial data . . . . .	14
2.4	Gauge freedom of GR, implications . . . . .	15
2.4.1	Gauge conditions . . . . .	15
2.4.2	Singularity treatment . . . . .	17
2.5	Hyperbolicity and Well-posedness . . . . .	18
2.6	Formulations . . . . .	20
2.6.1	BSSN . . . . .	21
2.6.2	Z4c . . . . .	22
2.7	Boundary conditions . . . . .	23
2.8	Discretization, computational infrastructure and the BAM-code . . . . .	24
2.8.1	Adaptive mesh-refinement (AMR) . . . . .	24
2.8.2	Parallelization . . . . .	25
2.8.3	Berger-Oliger timestepping . . . . .	25
<b>3</b>	<b>Physical observables</b>	<b>27</b>
3.1	Gravitational waves . . . . .	27
3.2	Wave-extraction . . . . .	28
3.2.1	Newman-Penrose formalism . . . . .	28
3.2.2	Implications for the accuracy of numerical waveforms . . . . .	29
3.2.3	Sphere integration - Simpson vs. Gauss-Legendre . . . . .	30
3.3	Convergence and error estimates . . . . .	31
<b>4</b>	<b>Black hole binaries on eccentric orbits</b>	<b>33</b>
4.1	The two-body problem of GR . . . . .	33
4.1.1	Relevance to GW astronomy . . . . .	34
4.1.2	Higher-order perturbation theory . . . . .	36
4.1.3	Relevance of eccentric binaries . . . . .	36

4.2	Results for quasi-circular orbits from Numerical Relativity . . . . .	38
4.3	Beyond quasi-circular orbits . . . . .	39
4.4	Zoom-whirl regime . . . . .	39
4.4.1	Definition and origin . . . . .	39
4.4.2	Relevance of zoom-whirls . . . . .	40
4.4.3	Illustration using geodesics . . . . .	41
4.4.4	Eccentric binaries . . . . .	42
4.5	Black hole parameters . . . . .	43
4.6	Numerical results . . . . .	45
4.6.1	Orbital phenomenology . . . . .	47
4.6.2	Radiation properties . . . . .	54
4.6.3	Phase space . . . . .	68
<b>5</b>	<b>Binary neutron stars on eccentric orbits</b>	<b>73</b>
5.1	The matter scheme . . . . .	73
5.1.1	Equation of state . . . . .	75
5.1.2	High Resolution Shock Capturing methods . . . . .	75
5.1.3	Vacuum treatment . . . . .	76
5.2	Binary neutron stars on eccentric orbits . . . . .	77
5.2.1	Initial data . . . . .	77
5.2.2	Test cases . . . . .	79
5.3	Binary case: Results . . . . .	81
5.3.1	Setup . . . . .	81
5.3.2	Global outcome and orbital dynamics . . . . .	82
5.3.3	Effects of truncation error during evolution . . . . .	83
5.3.4	A representative case . . . . .	85
<b>6</b>	<b>Conclusions and outlook</b>	<b>97</b>

# 1 Introduction: General Relativity and Gravitational Wave Astronomy

The theory of General Relativity (GR) since proposed by Einstein in 1915 [1, 2] successfully passed *all* experimental tests so far and therefore provides one of our most accurate and best understanding of gravity. There are alternative theories of gravity in agreement with observations. These measurements include the classical solar system tests in the weak-field regime, the orbital decay of the Hulse-Taylor pulsar, or observations of quasi-periodic oscillations around accreting neutron stars [3]. The ability of these tests to discriminate between different theories of gravity depends on the accuracy of the measurement but also most importantly on the diversity of the theoretical predictions. The largest discrepancies among theories are generically found in the strong field regime.

One basic prediction of GR which has not yet been directly verified is the existence of gravitational waves (GWs), i.e. strains in spacetime propagating at the speed of light. GWs are generated by non-stationary gravitational fields with strong signals only to be expected from the most compact and dynamical objects such as black holes, neutron stars, etc. Measurable GWs are thus expected to originate only from strong field regions governed by non-linear dynamics and therefore test our understanding of gravity in a regime with the most predictive impact. GWs emitted from other sources will be weak, which can be traced back to the weakness of the gravitational interaction (for a binary it is roughly proportional to Newton's constant squared  $\propto G^2$ ). By the time GWs arrive at earth even those produced in the most violent astrophysical events are likely to be tiny.

The weakness of GWs is both a blessing and a curse. On the one hand detection is challenging. On the other, it reduces any interactions along the line-of-sight after the emission process which yields a cleaner probe of strong curvature spacetimes. Furthermore the physical observable is the wave strain, i.e. the amplitude, which drops as  $1/d$  instead of the electromagnetic flux which behaves as  $1/d^2$  where  $d$  is the

distance from the source. That is to say once the threshold sensitivity is achieved measurements soon will reach out to large distances.

For these reasons GW observations will open up an entirely new window on the universe. Regions previously inaccessible to electromagnetic observations, such as the interior of dense compact objects, or the early universe (i.e. prior to the surface of last photon-scatter yielding the cosmic microwave background) may be studied with remarkable accuracy out to large distances.

The required sensitivity to measure the relative length change on km scale, even in an optimistic case, is<sup>1</sup>  $h = \Delta L/L \approx 10^{-22}$ . Nevertheless comparisons of future detector sensitivities with estimates for typical signal strengths suggest that such an ambitious measurement is within reach using cutting-edge technology.

The enormous precision required is achievable with laser interferometry or pulsar timing. Let us only introduce their basic aspects. In pulsar timing the passage of a gravitational wave can be inferred from a *correlated* change in the time of arrival of the otherwise extremely regular pulses of a magnetized, rotating neutron star. Laser interferometers use typically high-intensity ( $\lesssim 200W$ ) laser light which is split and sent through an L-shaped Michelson-Morley interferometer with a Fabry-Perot cavity. The main idea behind this apparatus is that when a gravitational wave passes through the detector it will periodically alter the path lengths of the individual interferometer arms. A key point is that the change in length of the two light travel paths is different, hence causing a phase shift and constructive interference when the beams are recombined. The technical challenges include to keep the arm length constant and thus e.g. the position of the mirrors to within the desired accuracy in relative length change and to keep the laser intensity constant. The high sensitivity of current detectors spawns noise sources as inevitable as quantum noise, seismic noise or surge of the sea shore, but also some of man-made origin such as fluctuations in the power lines and nearby lumbering. Those and many other noise sources have their own frequency dependence which has to be modelled. All effects combined result in a frequency dependent sensitivity of the detector. Proposed space missions for the next decade [4, 5] have design sensitivity to detect expected signals well above the detectors noise. For current ground based detectors first signals are expected to have small signal-to-noise ratios. This implies that source modelling and data processing are crucial to enhance detectability. In essence, the knowledge of the

---

<sup>1</sup>This accuracy corresponds to a displacement of the 4km path of the LIGO detector by a thousandth of a proton diameter or measuring the distance between the earth and the sun to the accuracy of an atom diameter.



waveform prior to detection allows the extraction of weak signals from the noise.

In case of a binary signal the wave will look to lowest order like a chirp signal, i.e. frequency and amplitude increase followed by the ring-down, i.e. constant frequency and exponentially decaying amplitude. The wavelength is set by the (dynamical) spatial extent of the source. In summary the signal will enter the sensitivity band of the detector from low frequencies in the early inspiral, gradually drift towards higher frequencies, and peak at the merger. Depending on the wavelength in relation to the size of the detector the inspiral may mostly not be seen.

Due to the non-linearity of GR source modelling is a delicate task. Different approaches have been developed each having their strengths and weaknesses. Perturbative methods *alone* such as the Post-Newtonian expansion [6, 7, 8] or the Effective-One-Body method [9, 10] can accurately and efficiently model the early inspiral when velocities are small compared to the speed of light. Predicting the gravitational waveform throughout the merger requires non-perturbative information which can only be obtained self-consistently by expensive numerical evolutions. There is a large overlap between these approaches that allows to combine the non-perturbative information from simulations with both analytic methods. In the case of the Post-Newtonian theory the numerically computed waveform is appended to the perturbative waveform [11]. In the Effective-One-Body framework the non-perturbative information is included by specifying free parameters [12]. Both procedures result in waveforms which can be used as templates which have been shown [13] to be accurate enough for current detectors.

Soon after the publication of general relativity the famous Schwarzschild solution was found [14]. It is the unique isotropic and static vacuum solution describing the external gravitational field of a spherical body[15]. In [16] it was found that a black hole is a generic outcome of a spherical collapse of a sufficiently massive gas cloud. In order to describe gravitational wave emission one seeks for non-stationary solutions. A long standing problem in GR and also one of considerable interest for GW astronomy is to predict the dynamics of two orbiting bodies under their mutual gravitational interaction and the associated gravitational radiation. The computational task consists in solving the field equation of GR for the metric field. In general the non-linearity of the field equation does not admit the superposition principle as in Newtonian gravity. Furthermore black-hole spacetimes give rise to singularities in the solution rendering this problem a considerable challenge.

Since several breakthroughs beginning with [17, 18, 19, 20] binary black-hole evo-

lution can be computed numerically. Hence, for a large volume of the underlying parameter space the black-hole two-body problem has been converted to the challenge of sampling a huge parameter space. Many studies [21] include spin and unequal masses. Further research is needed for achieving higher spins, momenta and mass ratios [22, 23, 24, 25]. In the pioneering work [19] a pure GR effect related to extreme precession effects and unstable circular orbits was found: *Zoom-whirl* orbits. However, despite the early discovery of zoom-whirl orbits that paralleled breakthroughs in the binary black hole problem still most studies assume *quasi-circular* orbits. There is, however, a growing literature on numerical studies of eccentric binaries.

The reason for this focus on quasi-circular binaries is founded on [26, 27] in which gravitational radiation was shown to circularize orbits of isolated binaries in the weak-field regime. This suggests that any primordial population of binaries that merge with significant eccentricity should be negligible. In the literature several mechanisms to dynamically form tight, eccentric binaries have been studied in Newtonian- and perturbative GR dynamics [28, 29, 30, 31, 32]. These mechanisms are thought to occur in dense stellar environments such as globular clusters or in the vicinity of supermassive black holes where contributions from a third body (or more) may drive eccentricity and the shrinking of the orbit, commonly referred to as hardening. Another important class of suggested scenarios leading to eccentric mergers is formed by capture events in gaseous environments which occur when galaxies collide. It is nowadays assumed there is a supermassive black hole at the center of almost every galaxy. The usual outcome of a collision between two galaxies (which is a frequently observed phenomenon) is a tight, eccentric binary of two supermassive black holes. The well-known quasar source OJ287, a so-called “BL Lac” object<sup>2</sup>, may be an example of such a system. Current models [33] calibrated to observations, dating back to the year 1881 [33], suggest a highly eccentric, tight binary system consisting of two supermassive black holes.

Besides black holes, neutron stars also curve spacetime in a strong manner with the advantage that neutron stars are known to exist. Thus neutron stars and neutron star binaries are promising GW sources. In the case of neutron stars there is the intriguing prospect of learning about QCD via GW observations. The equation of state of the neutron-star material is essentially unknown. There are many proposed models which in principle should be obtained from QCD at finite temperature

---

<sup>2</sup>A BL Lac (Lacertae) object consists of an active galactic nucleus whose emission axis is directed towards the earth.

and chemical potential. The equation of state describes the neutron star’s internal dynamics and consequently also dictates how the neutron star reacts to external perturbations. In scenarios where this perturbation due to tidal interaction becomes large enough (compared to the bulk dynamics) this establishes a link between the equation of state and the gravitational radiation of the binary. In particular, either for a black-hole neutron-star or neutron-star neutron-star binary system one expects that both the dynamics near merger and the subsequent wave emission depend on the equation of state. The stronger the imprints left in the waveform the better one can draw conclusions on the QCD phase diagram from GW observations [34]. While neutron star binaries on quasi-circular orbits are studied extensively, see e.g. [35] and references therein, the eccentric regime is untouched in full GR, so far.

One way of enhancing the imprints of the equation of state on the waveform is to consider neutron stars in binary systems on eccentric orbits. The orbital dynamics of eccentric binaries may lead to multiple close encounters and orbital “hang-up”, i.e. a delay of the inspiral, just before merger. This effects occur also in the regime of severe radiation losses because an eccentric orbit at pericenter has excessive angular momentum compared to a quasi-circular inspiral at the same separation. Close encounters and orbital hang-up both amplify tidal interactions. Each encounter gives rise to a characteristic burst signal with potential influences on the internal dynamics of the star. An increased duration in which the neutron star material is subject to strong tidal interaction, resisting gravitational collapse strongly affects the gravitational waveform during the onset of merger. In addition one expects that the properties of the resulting system (e.g. disk mass, black hole mass/spin, etc.) depend crucially on the eccentricity (or additional angular momentum, equivalently).

In general whenever matter is present in the strong field region around compact objects a combined observation of GWs and the electromagnetic counterpart offers a promising tool for cosmology. From the GW frequency change during inspiral and merger one can derive the luminosity distance and from the electromagnetic signal the redshift of the source. The entire data set of multiple sources at different distances would allow to redraw a gravitational analog of a Hubble diagram. Any discrepancies to the classical Hubble diagram would give rise to a wealth of theoretical interpretations [34].

In certain regimes such as the weak field limit where the companions move slowly compared to the speed of light or in the case where one of the bodies is much more massive than the other the dynamics can be predicted analytically. However the

case where the two masses are comparable and radiation losses cause a significant contribution to the orbital dynamics (and vice-versa) is in the main interest for GW astronomy (especially strong field tests of GR). In this regime descriptions which attempt to predict the resulting dynamics as a perturbation around a known analytical solution break down. They must be replaced by a non-perturbative description. So far the only tool capable of providing this is numerical relativity. A foliation of the four dimensional spacetime into families of three dimensional hypersurfaces of constant time allows the computation of the metric as a solution of an initial-boundary-value-problem subject to time independent constraints. The fundamental sets of equations arising from Einstein's field equation, the choice of independent variables as well as the appropriate addition of terms proportional to the constraints to the evolution equations result in a particular *formulation* of Einstein's field equation. Of the many known ones we will for the most part adopt the BSSN- but also the recently proposed Z4c formulation.

The numerical solution of Einstein's field equation of GR for a compact object binary spacetime is a computationally expensive task. The different length scales in the problem, namely the radii of the compact objects, the orbital separation and the wavelength of the GWs require special techniques to render the task achievable. There has been considerable effort in casting the continuum system in a form particularly useful for numerical purposes, but still there are many variables and terms that have to be evaluated for every timestep. For a usual production run this results in roughly 2000Gflop/s. Thus in general, such an evolution requires the use of modern supercomputers and a parallelized code. The computational domain is divided up into partially overlapping local patches on which the solution can be computed on a single computational node. The additional information needed for the local computation is then communicated over a high-speed network within an Message-Passing-Interface (MPI) environment.

The structure of this thesis is as follows: In chapter 2 we begin by introducing the 3+1 split, different formulations of GR and suitable choices of gauge conditions. The description of the continuum problem is completed by the initial data and boundary conditions. The considerations include aspects of the implementation. Chapter 3 outlines the extraction of physical observables and introduces gravitational waves. In chapter 4 we discuss the GR two-body problem and the results obtained for eccentric black-hole black-hole binaries. Finally, in chapter 5 we report our findings on the evolution of eccentric neutron-star neutron-star binaries.

# 2 The 3+1 decomposition of Einstein's equation and numerical relativity

In this chapter I will review basic aspects of the 3+1 decomposition as well as selected formulations of Einstein's equation. The focus will be on aspects most relevant to a numerical evolution and the link to mathematical properties of the underlying continuum PDE system. These considerations form the basis of understanding the methods adopted as well as the results of this thesis. All of the facts contained here can be found in standard literature (e.g. [36, 37, 38, 39, 40]).

## 2.1 Splitting space and time

One of the first concepts commonly taught about relativity is the unification of space and time to a single entity called *spacetime*. Spacetime is a 4D pseudo-Riemannian manifold equipped with a metric with a Lorentzian signature  $(-, +, +, +)$  that obeys Einsteins field equation

$$R_{\mu\nu}(g, \partial g, \partial\partial g) - \frac{1}{2}g_{\mu\nu}R(g, \partial g, \partial\partial g) = 8\pi T_{\mu\nu} \quad (2.1)$$

In many cases, in particular in the absence of symmetries, however, the 4D covariant form though theoretically elegant in general does not reveal an obvious, systematic approach to find a solution. One systematic approach to the solution of differential equation is to reformulate it as an initial-value problem (IVP or Cauchy problem). In [41] it was shown that for GR the solution to the IVP exists and is unique.

The approach commonly adopted in numerical relativity<sup>1</sup> is to revert the unifica-

---

<sup>1</sup>The 3+1 formalism is also widely used in other fields including analytical relativity, Loop-Quantum Gravity as well as cosmology.

tion of space and time by foliating spacetime into sequences of 3D spatial slices of constant time. Thereby one restates equation 2.1 as an IVP of a system of non-linear, coupled partial differential equations [42, 43, 44] commonly referred to as the ADM equations. They split into elliptic, constraint (i.e. time- and gauge-independent) and hyperbolic, evolution equations (see Sec. 2.2.2).

Solving Einstein's equation then corresponds to finding initial conditions for the IVP (i.e. the initial data problem) and evolve it forward in time. To obtain initial data one needs to solve the elliptic constraint equations as explained in 2.3. Solving the set of hyperbolic evolution equations yields the solution for all times.

## 2.2 Free vs constrained evolution

Assuming the existence of appropriate initial data that by definition fulfil the constraint equations there are two fundamental routes to proceed on. One can evolve the system either by strictly enforcing the constraints on every time slice (the constrained evolution approach [40, 45, 46]) or by not solving the constraints after the initial slice (the free evolution approach). In the latter approach the constraints are computed and monitored as an error diagnostic. This strategy is possible thanks to the Bianchi identities, which guarantee preservation of the constraints at the continuum level at all times provided they are fulfilled initially. When we introduce formulations in 2.2.2 one should keep in mind that they are implemented without solving the constraints at each timestep.

### 2.2.1 3+1 split

Introduce an arbitrary scalar function  $t = t(x^a)$  whose non-intersecting level surfaces defined by  $t = \text{const}$  form the hypersurfaces  $\Sigma_t$  with normal vector  $n_a = -\alpha \nabla_a t$  where the lapse  $\alpha$  is determined by the normalization  $n_a n^a = -1$ . The 3+1 split is a projection of the 4D quantities along  $n_a$  (the time direction) and  $\Sigma_t$  with the induced spatial 3D metric  $\gamma_{ij}$ .  $\Sigma_t$  is orthogonal to  $n_a$  (i.e.  $n_a \gamma^a_b = 0$ ). When the  $\Sigma_t$  are smooth level surfaces of  $t$  this slicing is called a *foliation*. The 4D spacetime is thereby stacked up into families of spatial hypersurfaces labelled by the coordinate time. In coordinates adapted to the foliation  $n_a = (-\alpha, 0, 0, 0)$ .

Our starting point is the construction of two projection operators

$$N_a^b \equiv -n_a n^b \quad \text{and} \quad \gamma_a^b \equiv g_a^b + n_a n^b. \quad (2.2)$$

Applied to the 4D metric this leads to the standard 3+1 decomposition

$$ds^2 = (-\alpha^2 + \beta_i \beta^i) dt^2 + 2\beta_i dt dx^i + \gamma_{ij} dx^i dx^j \quad (2.3)$$

with the lapse  $\alpha$  and the shift  $\beta^i = \gamma_{ij} t^j$ . The latter two quantities represent the freedom of choosing coordinates in a 3+1 framework<sup>2</sup>. The lapse measures how much proper time has elapsed for an observer along  $n^a$  from one slice to the next. The shift determines by how much a coordinate point has moved from one slice to the next. The relation between the 4D metric and the 3D metric and the unit normal vector then is

$$\gamma_{ab} = g_{ab} + n_a n_b. \quad (2.4)$$

There is freedom in how the hypersurfaces are embedded in the higher dimensional manifold which is expressed in a spatial tensor living on  $\Sigma$  called the extrinsic curvature

$$K_{ab} := -\nabla_a n_b = \mathcal{L}_{\vec{n}} \gamma_{ab} \quad (2.5)$$

Here  $\nabla$  denotes the covariant derivative with respect to  $\gamma_{ab}$  and  $\mathcal{L}$  the Lie-derivative.  $K_{ab}$  is closely related to canonical conjugate momenta  $\pi^{ij} = \sqrt{\gamma}(K^{\gamma ij} - K^{ij})$  within a Hamiltonian treatment, and replaces the latter due to its clear geometrical interpretation.

By contracting the Riemann tensor against the different combinations of  $n_a$  and  $\gamma_a^b$  one can then derive the equations by Gauss, Codazzi and Ricci which relate the 4D geometry to the spatial geometry intrinsic to the hypersurface and the extrinsic curvature. So far we have only introduced purely geometrical concepts independent of GR and the different reformulations. From these relations the projections of all quantities appearing in Einsteins field equation follow. The result are the ADM equations.

### 2.2.2 ADM

Arnold Deser and Misner (ADM-) in [44] derived a 3+1 decomposition of Einsteins field equations although these equations have been derived earlier. While the focus in [47, 43, 42] has been on the initial value problem of GR in [48, 44] the equations were derived using a Hamiltonian formulation in an attempt to quantize gravity. They differ from the equations we will give below by a term  $-\alpha \gamma_{ij}/2H$  in

---

<sup>2</sup>A different notation for the lapse  $N$  and for the shift  $N_i$  is also frequently used.

the evolution equation for  $K_{ij}$ <sup>3</sup>. The following version is due to York [49] and is commonly referred to as the ADM equations in the numerical relativity community, despite the fact that they differ from the ones derived earlier. They read

$$\left(\frac{\partial}{\partial t} - \mathcal{L}_\beta\right)\gamma_{ij} = -2\alpha K_{ij} \quad (2.6)$$

$$\begin{aligned} \left(\frac{\partial}{\partial t} - \mathcal{L}_\beta\right)K_{ij} &= -D_i D_j \alpha + \alpha(R_{ij} + K K_{ij} - 2K_{ik} K_j^k + \\ &+ 4\pi[(S - E)\gamma_{ij} - 2S_{ij}]) \end{aligned} \quad (2.7)$$

$$R + K^2 - K_{ij} K^{ij} = 16\pi E \quad (2.8)$$

$$D_j K_i^j - D_i K = 8\pi p_i. \quad (2.9)$$

York's version essentially leads to better-behaved constraint subsystem and uses  $K_{ij}$  instead of  $\pi_{ij}$  as independent variables. To avoid confusion with the standard literature we will also refer to York's version as the ADM equations. We will discuss in Sec. 2.6 continuum properties of this and other formulations of GR in more detail.

One can see they form a set of coupled first-order in time second-order in space, non-linear system of PDEs for the unknowns  $(\gamma_{ij}, K_{ij}, \alpha, \beta^i)$ . They were used for a long time in numerical relativity codes, but simulations lacked the necessary numerical stability and so, e.g. the binary black hole problem remained unsolved. The issue was related to an undesirable mathematical structure in the ADM equations which we will discuss together with other reformulations of ADM in Sec. 2.6.

## 2.3 Initial data

In this section we give a brief introduction to initial data. For a more detailed description the reader is referred to [36].

In order to obtain initial conditions for the IVP one has to solve the constraint equations which are in general coupled non-linear elliptic equations for  $\gamma_{ab}$  and  $K_{ab}$ .

The constraint subsystem of GR is an under-determined system, i.e. there are only four equations for the twelve unknowns. While the mathematical problem of finding an initial data set that satisfies the Einstein equation is usually achieved with remarkable accuracy it is a much harder problem to spot which additional conditions to impose in addition to the constraint equations in order to both *close*

---

<sup>3</sup>The difference can be traced back to the choice of fixing  $\alpha$  or the  $\alpha\sqrt{\gamma}$  (the densitized lapse) when varying the Hamiltonian w.r.t.  $\gamma_{ij}$  [38]



the system and to obtain initial data that corresponds to the *physics* one had in mind. The latter problem can only be studied by numerically evolving the initial data and analyzing its properties. One should note, that some undesirable features in the initial data can be hidden in a subtle way only revealing themselves after a considerable amount of evolution time.

We point out that other ways of setting up initial data are also in frequent use [36]. The most important framework is the conformal thin-sandwich framework. It is used both with the Generalized-Harmonic formulation as well as with the BSSN formulation. In contrast to puncture initial data the conformal thin-sandwich formalism does not provide data for the black hole interior. Consequently one either has to excise the black hole interior or instead fill it artificially by extrapolating from data outside. Both approaches are built on the property of an event horizon that nothing can leak out of it.

**Conformal decomposition** It has been a popular choice in numerical relativity to perform a conformal decomposition, i.e. one splits a conformal factor  $\Psi$  off the metric<sup>4</sup>

$$g_{\mu\nu} = \Psi^4 \tilde{g}_{\mu\nu}. \quad (2.10)$$

Additionally, the extrinsic curvature is often decomposed further into its trace and its trace-free part

$$\tilde{K}_{ij} = \tilde{A}_{ij} + \frac{1}{3} \tilde{\gamma}_{ij} \tilde{K} \quad (2.11)$$

$$\tilde{K}_{ij} = \Psi^{-2} K_{ij}. \quad (2.12)$$

### 2.3.1 Bowen-York solution

Under sufficiently simplifying assumptions the constraints can be solved analytically, but in general they have to be solved numerically. The simplest approach is based on the work by Bowen & York [50]. In the Bowen-York solution eight conditions are fixed by assuming a conformally flat metric and time-symmetry <sup>5</sup> $K_{ij} = 0$ . The latter choice implies maximal slicing  $K = 0$ .

<sup>4</sup>The power can be chosen freely, but we set it for matter of convenience to 4.

<sup>5</sup>The latter notion of "time-symmetric" originates from the identity  $K_{ij} = \mathcal{L}_{\tilde{n}} \gamma_{ij}$  and the interpretation of the Lie-derivative as a generalized time derivative. Thus,  $K_{ij} = -\mathcal{L}_t \gamma_{ij} = 0$  is like a turning point for the spatial metric.

In this case the constraints decouple from each other. The momentum constraint becomes linear thus admitting the superposition principle. The solution is analytical and reads

$$\begin{aligned} \tilde{A}^{ij} = & \frac{3}{2r^2}(P^i n^j + P^j n^i + (\eta^{ij} + n^i n^j)P_k n^k) \\ & + \frac{3}{r^3}(\epsilon^{icd} S_c n_d n^j + \epsilon^{jcd} S_c n_d n^i) \end{aligned} \quad (2.13)$$

where  $P^i$  and  $S^i$  for small values can be identified with the ADM-momentum and the spin (ADM-angular momentum) of a single black hole. The remaining equation for the conformal factor reads

$$\Delta\Psi = -\frac{1}{8}\Psi^{-7}\tilde{A}_{ij}\tilde{A}^{ij} \quad (2.14)$$

This non-linear elliptic equation is all that is left to solve numerically. The solution to the boundary value problem composed of equation 2.14 and Dirichlet-boundary conditions, in particular,  $\Psi = 1$  at  $r = 0$  and  $r = \infty$  exists and is unique [51].

### 2.3.2 Puncture Initial data

Building on the Bowen-York solution the remaining Hamiltonian constraint on  $\Psi$  equation 2.14 can be solved [52] for multiple conformally flat solutions in the following way: First one writes the conformal factor as

$$\Psi = 1 + \sum_i \frac{m_i}{2r_i} + u \quad (2.15)$$

The idea behind this step is that the singular part of  $\Delta\Psi$  is absorbed in an analytic expression while the unknown correction is regular on  $R^3$ .

For a single black hole written in isotropic coordinates

$$ds^2 = -\left(\frac{1 - \frac{M}{2r}}{1 + \frac{M}{2r}}\right)^2 dt^2 + \Psi^4 dx_i dx^i \quad (2.16)$$

the correction  $u = 0$  vanishes and the Hamiltonian constraint is solved analytically. In addition  $K_{ij} = 0$  solves the momentum constraint. Adding another black hole  $u = 0$  does not solve the Hamiltonian constraint anymore, thus one must solve it numerically for  $u$ .

It was shown by [53] that there exists no slicing of the Kerr spacetime which is conformally flat. There is evidence that the boosted Schwarzschild solution and any physical solution containing multiple black holes share that property. This implies that binary spacetimes with Bowen-York momentum and spin cannot be stationary (they cannot be described the Kerr metric because they are conformally flat) and thus necessarily contain some spurious amount of junk radiation which reduces for larger initial separations but which grows with the momentum and spin.

Despite these known consequences of fixing the undetermined degrees of freedom in the initial data this description is heavily used in black-hole-binary initial data including in this thesis.

## 2.4 Gauge freedom of GR, implications

It is well known that the gauge freedom of GR is the invariance under diffeomorphisms and forms one of the guiding principles in Einstein's theory of gravity. Like in other gauge theories the fundamental fields (in GR the metric  $g_{\mu\nu}$ ) are not uniquely determined, but observer dependent and as such cannot be physical observables. However, for an actual computation it may be technically necessary to specify (or "fix") the gauge condition.

Also in analytic calculations the fact that results are obtained by fixing the gauge condition is not in contradiction with gauge invariance, but rather exemplifies the fact that certain gauge choices can be beneficial over others for mathematical/computational methods.

These considerations immediately lead to three questions: (1) What are the physical observables of the spacetime? (2) To what extent do these computations carry over to other gauge choices? (3) In the case of a numerical solution, what gauge conditions lead to desirable properties, like for instance numerical stability?

Post-poning questions (1) to chapter 3 and (2) to section 4.6.3 here we only address question (3).

### 2.4.1 Gauge conditions

When discretizing Einstein's eq. (especially when solving for spacetimes containing singularities or strong curvature regions) one has to prescribe the gauge condition in well-suited ways to achieve stable evolution schemes [54, 55]. In fact, the first

gauge choices in use gave rise to unstable numerical evolutions.

In the 3+1 framework of GR the freedom to choose any coordinate system is represented by the lapse  $\alpha$  and the shift vector  $\beta^i$  as explained in Sec. 2.2.1.

The simplest choice is to use Gaussian normal coordinates or "geodesic slicing" where one sets  $\alpha = 1$  and  $\beta^i = 0$ . The name "geodesic slicing" stems from the fact that coordinate time coincides with proper time measured by an Eulerian observer<sup>6</sup> between neighbouring hypersurfaces  $\Sigma_t$  and that lines of constant spatial coordinates are orthogonal to the hypersurface  $\Sigma_t$ . With this choice any metric becomes simply

$$g_{\mu\nu}dx^\mu dx^\nu = -dt^2 + \gamma_{ij}dx^i dx^j. \quad (2.17)$$

This gauge choice turns out to be an unfortunate one when evolving curved spacetimes. The evolution fails even for small perturbations around Minkowski space.

One way to avoid these problems is to let the gauge quantities dynamically adjust to the local properties of the spacetime in a way that whenever singularities are encountered the gauge can adjust for the sake of numerical stability. In order to give a more concrete example: It is e.g. possible to drive the lapse to zero when the slices approach a singularity. As a consequence the evolution freezes and does not reach the singularity leading to an effect called slice-stretching<sup>7</sup>. This property is called singularity avoidance. On a more analytical level one may write the gauge conditions in a form where they are driven towards an asymptotic end state dictated by the symmetries of the expected late stage spacetime<sup>8</sup>. Such properties are called symmetry seeking.

The standard evolutions in numerical relativity use gauge choices which are solutions to differential equations rather than prescribed values as it often is the case in analytical works.

It has been found in [54] see also discussions in [38, 39] that gauge conditions for the lapse of the form

$$\partial_0\alpha \equiv \dot{\alpha} - \beta^i\alpha_{,i} = -\alpha^2 f(\alpha)K \quad (2.18)$$

yield superior stability properties and unsurprisingly add considerably to the robustness of a numerical scheme to solve Einsteins eqn. This is called the Bona-Maso family of gauge conditions.

---

<sup>6</sup>An Eulerian observer in a 3+1 framework is defined by a worldline which is parallel to  $n_a$  for all times.

<sup>7</sup>While useful for a stable evolution near singularities it does lead to crashes, eventually.

<sup>8</sup>By late stage we obviously refer to a 3+1 concept of time which is observer dependent.

The approach commonly used together with the BSSN formulation, which we will discuss in 2.4.2, is the so-called *moving-puncture gauge* which itself is a combination of the *1+log* slicing condition<sup>9</sup> for the lapse and the  $\tilde{\Gamma}$ -*driver condition* for the shift:

$$\partial_0\alpha = -\alpha^2 f(\alpha)K \quad (2.19)$$

$$\partial_0\beta^i = \mu_s \tilde{\Gamma}^i - \eta\beta^i \quad (2.20)$$

In the BAM code [56] we use

$$\partial_0\alpha = -2\alpha K \quad (2.21)$$

$$\partial_0\beta^i = 3/4B^i \quad (2.22)$$

$$\partial_0B^i = \partial_0\tilde{\Gamma}^i - \eta B^i. \quad (2.23)$$

These gauge choices yield stable evolutions for many different types of spacetimes including Minkowski-, spinning-, boosted- or multiple black-hole spacetimes and are in this sense very robust.

The most important consequence of the  $\tilde{\Gamma}$ -driver is that it compensates the infall of coordinate points towards singularities and effectively counteract the slice-stretching effect discussed above in the context of Bona-Maso slicing conditions.

For unequal mass binaries the  $\eta$ -parameter introduced to damp oscillations in the shift requires extra care. Inspecting the gauge conditions one discovers that it has dimensions of an inverse mass. For comparable mass binaries  $\eta = \text{const}$  can be chosen adequately. For large mass ratios  $\eta$  can be made sensitive to the local mass to dynamically (or in an analytically prescribed way) adjust the effects of the  $\tilde{\Gamma}$ -driver, accordingly.

## 2.4.2 Singularity treatment

Naturally the most interesting aspects of GR involve spacetimes with strong dynamics and curvature. In the extreme case when studying black holes one faces the difficulty of having to deal with singularities present in the solution. One has to choose coordinates that do not evolve to the physical singularity at the center of the black hole. Singularities at the horizon can be avoided by choosing coordinates which are regular at the horizon.

The most intuitive and frequently used approach is to exclude this singularity

---

<sup>9</sup>A special case of the Bona-Maso family with  $f = 2/\alpha$

from the computational domain and to impose boundary conditions on the resulting excision surface that captures the physics of the removed interior. The excision surface has to be inside the event horizon. The *apparent horizon*<sup>10</sup> is used in practice.

In principle boundary conditions should not be needed because inside the horizon all characteristics by definition point inward. Thus, at least in the continuum, from the excision surface nothing can escape from its interior and hence influence the exterior dynamics. Numerically, however this is not guaranteed and needs care.

The second, less obvious approach able to handle spacetime singularities is the *puncture* method [52, 56].

The key is a specific gauge choice (the *moving-puncture gauge*) together with a conformal decomposition of the evolved variables. The singularities are weakened during moving-puncture evolutions in the sense that the conformal factor can be shown to settle down from the  $r^{-1}$  to a  $r^{-1/2}$  behaviour near the puncture. In [57] this observation was linked to an analytical solution of Schwarzschild in maximal slicing found in [58]. In [57] an analytical solution for the stationary state of a spherically symmetric bh has been constructed in agreement with numerical results. This solution is now called the trumpet solution because the slices evolve to a cylindrical topology. A spherical collapse of dust was shown to approach this solution closely [59]. The authors interpret the disappearance of matter from the grid by this topology change: The other asymptotically flat end is squeezed in a region that remains unresolved by the grid. Note, that in the puncture method the computational domain also covers the interior of a black hole and there is neither the need to excise the black hole interior nor to impose artificial boundary conditions on the horizon. These aspects make the moving-puncture technique an attractive method for numerical relativity evolutions.

## 2.5 Hyperbolicity and Well-posedness

Only now that we have introduced both evolution systems and the gauge sector we are in the position to consider hyperbolicity and well-posedness of the full set of Einstein's equations. In this section we will closely follow [60, 37, 55].

For the IVP the notions of well-posedness and hyperbolicity are closely related. The idea behind the definition of well-posedness is that in order to have a consistent

---

<sup>10</sup>The apparent horizon is an approximate notion of the *event horizon* defined by the outermost surface with vanishing expansion  $\Theta \equiv D_s - K + K_{ss}$  where  $s$  denotes indices contracted against the outward pointing unit normal.

(i.e. converging) approximation to the continuum problem the solution must *depend continuously on the initial data*. More precisely a system has a well-posed initial (boundary) value problem if the solution can be bound by the initial and boundary data  $b(\cdot, \tau)$

$$\|u(\cdot, t)\| \leq F(t) \left( \|u(\cdot, 0)\| + \int_0^t b(\cdot, \tau) d\tau \right) \quad (2.24)$$

where  $F(t)$  is independent from the initial (and boundary) data.

Well-posedness and hence stability properties of partial differential equations (PDEs) can solely be analyzed in terms of the principal part. The principal part of a system of partial differential equations consists of the terms involving the highest derivatives.

All formulations discussed in this thesis can be obtained from the ADM formulation and thus share the first-order-in-time second-order-in-space form as a natural consequence of a Hamiltonian formulation. They are of the form

$$\dot{v} \simeq \partial v + w + \partial z \quad (2.25)$$

$$\dot{w} \simeq \partial \partial v + \partial w + \partial \partial z \quad (2.26)$$

where  $\simeq$  stands for equality in the principal part.

For simplicity we will instead define different notions of hyperbolicity on first order systems (as in [60]) of the form

$$\dot{u} \simeq P^i(u) u_{,i} + S(u) \quad (2.27)$$

where  $P^i$  are square matrices. We will define the different notions of hyperbolicity (weak-, strong- or symmetric hyperbolicity) of the first-order-in-time second-order-in-space system according to the existence of a reduction to a fully first order system which is weakly, strongly or symmetric hyperbolic, respectively.

**Definition** *Weak Hyperbolicity*. The system (2.27) is called *weakly* hyperbolic if the matrix  $P^n = n_i P^i$  has real eigenvalues for any unit vector  $n_i$ .

The notion of weak hyperbolicity is insufficient for the wellposedness of the initial value problem. The ADM equations in the form of equations 2.6 are only weakly hyperbolic and thus yield an ill-posed Cauchy problem. More generally, if an initial value problem is ill-posed *no* numerical implementation converges to the correct answer.

**Definition** *Strong Hyperbolicity.* The system 2.27 is called *strongly* hyperbolic if  $P^n$  is diagonalizable with real eigenvalues for any  $n_i$  and the matrix  $T_n$  that diagonalizes it and its inverse  $T_n^{-1}$  depend smoothly on  $n_i$

Together with the definition of characteristic variables this implies equivalence of strong hyperbolicity and the existence of a complete set of characteristic variables (eigenvectors) with real speeds that depend smoothly on  $n_i$ . Strong hyperbolicity implies weak hyperbolicity and in contrast to the latter guarantees wellposedness of the initial value problem.

**Definition** *Symmetric Hyperbolicity.* The system 2.27 is called *symmetric* hyperbolic if there exists a Hermitian, positive definite matrix  $H$  such that  $HP^n$  is Hermitian for any direction  $n_i$  and where  $H$  does not depend on  $n_i$ .

An example is the Generalized Harmonic formulation or Z4c coupled to the harmonic gauge. Symmetric hyperbolicity may be used to prove wellposedness of the initial boundary value problem. Symmetric hyperbolicity (for the constant coefficient case) gives rise to a quantity called an energy which may as an estimate for equation 2.24

## 2.6 Formulations

In 2.2.2 we have introduced the ADM equations which can be viewed as the first known 3+1 formulation of the Einstein equation. The ADM equations are only weakly hyperbolic and thus do not admit a well-posed initial value problem. In fact, when using the ADM equations to evolve small perturbations around Minkowski initial data (using e.g. geodesic slicing) the numerical solution blows up quickly.

Given a set of PDEs there are many ways of rewriting them such that in the continuum limit they are equivalent. For instance one can always choose different independent variables and related to that write the system with different numbers of derivatives. If the PDE system has a constraint subsystem there is the additional option of adding multiples of the constraints to the evolution equations without affecting physical solutions (i.e. the continuum limit). Such modifications alter the principal part and thus the characteristic structure as well as hyperbolicity properties. Thus such modifications may bring the system to a form which leads to a well-posed IVP.

There are many hyperbolic reformulations of GR, for an introduction to which we refer the interested reader to [55, 38] and references therein. One important



example which we do not discuss here and instead refer to [61] is the Generalized Harmonic formulation which was successfully used in the first breakthrough to tackle the binary black hole problem [19]. In the Generalized Harmonic formulation one needs to dynamically track the apparent horizon and excise the black hole interior replacing the values just inside the excised region with suitable boundary conditions.

At the discrete level (for numerical purposes) the system does *not* inherit all but only *some* properties of the continuum system. In particular some reformulations of a given set of PDEs at a given resolution numerically outperform others even when they have the same hyperbolicity and stability properties. Hence, hyperbolicity is not the only criterium for how well a formulation performance in practical applications. For instance, it turns out that a conformal decomposition as described in Sec. 2.3 lead to improved properties<sup>11</sup>.

## 2.6.1 BSSN

One important and widely used reformulation of the ADM equations is the BSSN system [62, 63]. There are several slightly different incarnations in use<sup>12</sup>. Here I only give the version relevant for the results of my thesis.

One performs a conformal transverse-traceless decomposition, see equations 2.10, 2.12 and 2.11, with  $\psi^4 = \gamma^{1/3}$  such that  $\tilde{\gamma}_{ij}$  has a unit determinant<sup>13</sup>. Most importantly one further introduces  $\tilde{\Gamma}^i = \tilde{\gamma}^{jk}\tilde{\Gamma}_{jk}^i$  as a new independent variable. The crucial impact on the stability properties have been pointed out in [64]. The above introduction allows to absorb mixed, second derivatives inside the 3D Ricci tensor arising in the evolution equation of  $\tilde{A}_{ij}$  (or  $K_{ij}$  in the ADM form) into a single derivative of  $\tilde{\Gamma}^i$  rendering the evolution equations for  $\gamma_{ij}$  and  $K_{ij}$  essentially to a wave equation. Yet another step is required to obtain a stable scheme. One adds the momentum constraint to the evolution equation of  $\tilde{\Gamma}^i$ . These procedures yield

---

<sup>11</sup>The reason for this improvement is currently not fully understood.

<sup>12</sup>Different conformal factors are used,  $\chi = \Psi^{-4} = e^{-4\phi}$  called the  $\phi$ -, or  $\chi$ -method, respectively.

<sup>13</sup>The algebraic constraints arising from these definitions, namely unit determinant of  $\tilde{\gamma}_{ij}$  and  $\tilde{A}_{ij}$  being tracefree is strictly enforced during evolution.

the BSSN equations [62, 63]:

$$\frac{d\tilde{\gamma}_{ij}}{dt} = -2\alpha\tilde{A}_{ij} \quad \frac{d\phi}{dt} = -\frac{1}{6}\alpha K \quad (2.28)$$

$$\begin{aligned} \frac{d}{dt}\tilde{\Gamma}^i &= \tilde{\gamma}^{jk}\partial_j\partial_k\beta^i + \frac{1}{3}\tilde{\Gamma}^{ij}\partial_j\partial_k\beta^k - 2\tilde{A}^{ij}\partial_j\alpha + 2\alpha(\tilde{\Gamma}_{jk}^i\tilde{A}^{jk} + \\ &6\tilde{A}^{ij}\partial_j\phi - \frac{2}{3}\tilde{\gamma}^{ij}\partial_j K - 8\pi\tilde{j}^i) \end{aligned} \quad (2.29)$$

$$\frac{d\tilde{A}_{ij}}{dt} = e^{-4\phi}(-D_i D_j \alpha + \alpha R_{ij})^{TF} + \alpha(K\tilde{A}_{ij} - 2\tilde{A}_{ik}\tilde{A}_j^k) \quad (2.30)$$

$$\frac{dK}{dt} = -D_i D^i \alpha + \alpha(\tilde{A}_{ij}\tilde{A}^{ij} + \frac{1}{3}K^2) \quad (2.31)$$

where TF denotes the trace-free part. The numerical stability properties have been analyzed in [63, 65]. BSSN when coupled to the moving puncture gauge is strongly hyperbolic [66, 67, 55]. From the above definitions it follows that BSSN has a well-posed IVP.

## 2.6.2 Z4c

The Z4 formulation was introduced in [68, 69]. Among the intriguing attributes of this formulation compared to BSSN is the more advanced stage of boundary conditions, see e.g. [70, 71], and its manifest covariance. Another is that constraint violations propagate with the speed of light. The latter property is particularly desirable when solving hyperbolic problems with constraint equations using a free evolution approach. In contrast the BSSN formulation has a zero speed mode associated with the Hamiltonian constraint, see [72], which can result in a local accumulation of constraint violations due to numerical error. In fully propagated schemes these violations can propagate off the computational domain, potentially yielding more accurate evolutions. In [72] the Z4 formulation was conformally decomposed and written in a way very close to the BSSN system, but with one additional variable  $\Theta$ . The resulting formulation is called Z4c. The addition of  $\Theta$  allows for the Hamiltonian constraint violating modes to propagate at a non-vanishing speed in the continuum. In addition it allows the use of constraint damping [73] because its time derivative is proportional to the Hamiltonian constraint. The constraint damping scheme was actually the last key ingredient in [19] to successfully evolve binary black holes with the Generalized Harmonic Formulation. The BSSN system lacks such a constraint damping scheme. The equations of motion are the BSSN ones with  $K$  replaced by

$\hat{K} = K + 2\Theta$ . In the limit of vanishing  $\Theta \rightarrow 0$  BSSN is recovered. Z4c differs from Z4 only in non-principal terms and therefore has the same characteristic structure and hyperbolicity properties.

Z4c when coupled to the moving puncture gauge is strongly hyperbolic. For the proof see [55]. From the above definitions it follows that Z4c has a well-posed IVP.

In [72] it was found that in particular the Hamiltonian constraint violations in spacetimes containing compact matter sources out performed corresponding BSSN evolutions in the case of spherical symmetry.

## 2.7 Boundary conditions

The foliations considered in most numerical relativity studies including this thesis necessitate appropriate (outer) boundary conditions (BC) to capture the spacetime outside the computational domain. The spacetime at the outer boundary typically still differs significantly from any asymptotic analytic solution. Hence, it is not trivial to specify BCs.

The current choice of all moving-puncture codes used at the moment is to assume all variables satisfy an advection equation in the radial domain and thus obey an purely outgoing wave solution<sup>14</sup>. This results in the Sommerfeld boundary conditions:

$$\dot{f} + v \left( f' + \frac{f - f_0}{r} \right) \hat{=} 0. \quad (2.32)$$

$$f \hat{=} f_0 + \frac{u(r - vt)}{r} \quad (2.33)$$

Ideally one would like the BCs to fulfill some desirable properties, see e.g. [74], some of which I list here:

- stable: well-posed IBVP
- constraint preserving: obey the constraint equations
- absorbing: minimize reflections of unphysical modes
- converging: converge with resolution at the consistent order

---

<sup>14</sup>Boundary conditions that involve the assumption of neglecting incoming modes are also called maximally dissipative boundary conditions

Typical proofs of well-posedness of the IBVP necessitate assumptions on a background on which one linearizes the equations and are mostly carried out on the continuum system. Eventually, one wishes to demonstrate at least numerical stability. Thus, in the end a numerical evolution will reveal whether the mathematical evidence for stability will carry over to the numerical scheme.

## 2.8 Discretization, computational infrastructure and the BAM-code

After having described the continuum system we want to solve we will now describe the basics of the numerical methods adopted.

The BSSN equations 2.28 are discretized and solved numerically using the BAM-code [56].

The discretization of the BAM code is done according to a finite-difference approach. Centered stencils are used with the exception of advection derivatives which are lopsided (the sidedness of the stencil being determined by the shift) or at refinement or outer boundary points where due to the communication overhead no buffer zones are available.

The time integration is done with a method-of-lines approach using a third or fourth order Runge-Kutta method.

### 2.8.1 Adaptive mesh-refinement (AMR)

The equations are solved on a hierarchy of refinement levels. Communication between the levels is done via restrict (fine to coarse) or prolongation (coarse to fine) operators. A box-in-box refinement in space is used where the inner boxes follow the motion of the compact objects. For this the bulk motion of the compact objects have to be tracked<sup>15</sup>. This tracking is done by integrating the shift condition with the initial position as initial condition. The grid spacing from one level to the other is scaled typically by a factor of two.

AMR helps to resolve the different lengthscales in the problem<sup>16</sup>. Furthermore,

---

<sup>15</sup>Note, that tracking the compact objects is otherwise not needed as for example in calculations employing the point particle representation. The center of the compact objects or a point on a black hole event horizon is not distinct in any way when solving a *field* equation.

<sup>16</sup>The problem of different timesteps associated with the different lengthscales remains and is the main obstacle in terms of computational efficiency.

with AMR it is possible to push the location where boundary conditions are imposed further out, i.e. in a regime where the assumptions behind the boundary conditions (e.g. flat Minkowski space) becomes better. The problem for cartesian coordinates is that one loses resolution in the radial direction which is needed for an accurate wave propagation. This is compensated by doubling the number of points on the outer (fixed) levels compared to the inner (moving ones). This is rather expensive especially in terms of memory requirements<sup>17</sup>. A much better solution is to use spherical shells for the outer levels [75]. In general, numerical errors tend to be large near refinement boundaries. One reason is the sudden jump in resolution and another is the fact that the order of artificial dissipation is progressively reduced due to the lack of sufficient buffer points.

### 2.8.2 Parallelization

After casting the BSSN system in its discrete form it turns out that in order to solve the resulting algebraic equations even for more accurate high order finite difference operators typical numbers of floating point operations and memory requirements exceed limits of single core computers, but see [76]. One right hand side computation per timestep (i.e. on the coarsest level) is on the order of a few  $\approx 1000Gflops$ . To deal with this computational task BAM is a parallelized code. The grid structure is subdivided into processor local patches which overlap with each other just enough to pass the information required to evaluate the largest local stencils. The library used to handle the communication between processors is the widely used *message passing interface (MPI)*.

### 2.8.3 Berger-Oliger timestepping

The different refinement levels also have to be evolved at different timesteps. The method proposed in [77] is second order accurate and works as follows. To guide the description we give a pseudo-code taken from [56]:

---

<sup>17</sup>The Berger-Oliger timestepping (discussed below) leads to an only moderate increase in terms of overall FLOPs because the outer levels are only rarely updated compared to the inner ones.

```

evolve_hierarchy(1, Δt)
  evolve(1, Δt)
  if (1 + 1 < L)
    evolve_hierarchy(1 + 1, Δt/2)
    evolve_hierarchy(1 + 1, Δt/2)
  if (1 > 0)
    restrict_prolong(1 - 1, 1)
  regrid(1)

```

The routine *evolve\_hierarchy* is called on the coarsest level  $l = 0$ . A routine *evolve* advances level  $l$  by the time step passed to *evolve\_hierarchy*. Then there is a recursive function call to *evolve\_hierarchy* for level  $l + 1$  with half the time step which is aborted when the finest level is reached. After each *evolve\_hierarchy* call restrict and prolongation operations fill the AMR refinement boundaries. The regridding updates the grid structure.

An example of Berger-Oliger timestepping (columns: level,iteration,time)

0	3	0.750
1	5	0.625
2	9	0.562
3	17	0.531
3	18	0.562
2	10	0.625
3	19	0.594
3	20	0.625
1	6	0.750
2	11	0.688
3	21	0.656
3	22	0.688
2	12	0.750
3	23	0.719
3	24	0.750

# 3 Physical observables

Successful evolutions alone yield values for the independent variables of the formulation at different grid points and times. One is still left with the task of computing physical observables that can be compared to measurements. In this chapter we briefly describe the approaches to compute physical observables.

## 3.1 Gravitational waves

Gravitational waves are analytic solutions to GR in the weak field approximation. Consider a linear perturbation around Minkowski spacetime

$$g_{\mu\nu} = \eta_{\mu\nu} + h_{\mu\nu} \quad (3.1)$$

where  $h_{\mu\nu}$  is small compared to  $\eta_{\mu\nu}$ . Instead of  $h_{\mu\nu}$ , we will use  $\bar{h}_{\mu\nu} = h_{\mu\nu} - \eta_{\mu\nu} h^\lambda{}_\lambda / 2$  together with *Lorentz Gauge*  $\nabla_\mu h^\mu{}_\nu = 0$ . The Einstein equation reads then

$$\square \bar{h}_{\mu\nu} \equiv \nabla^\lambda \nabla_\lambda \bar{h}_{\mu\nu} = 0 \quad (3.2)$$

There is further gauge freedom which we fix by choosing the transverse-traceless (TT-) gauge

$$\bar{h}^{\mu 0} = 0 \quad \bar{h}^{\mu\nu}{}_{;\mu} = 0 \quad (3.3)$$

In the TT-gauge the time-space components of the Riemann-tensor are

$$R_{i0j0} = -\frac{1}{2} \ddot{h}_{ij}^{\text{TT}} \quad (3.4)$$

The effects of a gravitational wave on test particles, such as the test particles that form the interferometer arms with length  $L$  of our detector is given by

$$\ddot{L}_i = \frac{1}{2} \ddot{h}_{ij}^{\text{TT}} L^j \quad (3.5)$$

### 3 Physical observables

When expressed in terms of the two remaining polarization degrees of freedom a gravitational wave reads

$$h_{ij}^{TT} = h_+ e_{ij}^+ h_x e_{ij}^x \quad (3.6)$$

with  $e^{+/x}$  being polarization tensors.

The spacetime of sources which give rise to strong gravitational radiation is not described adequately by this approximation. In this regime Einstein's field equation is not a simple wave equation. Hence, the fluctuations of the gravitational field in the strong field regime are not gravitational waves. Instead, the dynamics is governed by a combination of longitudinal and transverse, i.e. radiative components which cannot be disentangled unambiguously. However, once these fluctuations have propagated away from the emitting source the transverse part can be modeled as described above.

## 3.2 Wave-extraction

The GW strain  $h$  is the most important physical observable of numerical relativity calculations. One technique for computing it is the Newman-Penrose formalism which I describe next along with other aspects of GW extraction.

### 3.2.1 Newman-Penrose formalism

The Newman-Penrose formalism is a method to extract GWs from a generic spacetime [78, 79]. It is gauge invariant to first order in the metric perturbation. The idea is to represent the 10 linearly independent components of the Weyl Tensor  $W_{bcd}^a$  as five complex scalars  $\psi_i$  ( $0 \leq i \leq 4$ ). The  $\psi_i$  are defined by contractions of the Weyl-tensor against specific combinations of null tetrad vectors  $l^a, n^a, m^a, \bar{m}^a$ .

A null tetrad is a set of tetrad vectors satisfying the following conditions:

$$l^a l_a = n^a n_a = m^a m_a = \bar{m}^a \bar{m}_a = 0 \quad (3.7)$$

$$l^a n_a = -1, \quad m^a \bar{m}_a = 1, \quad (\text{all other pairs vanish}) \quad (3.8)$$

In particular,  $\psi_4$  is defined as the following contraction

$$\psi_4 := -C_{abcd} n^a \bar{m}^b n^c \bar{m}^d \quad (3.9)$$

The key observation is that in the weak field regime and in the appropriate gauge



$\psi_4$  can be identified with the outgoing gravitational degrees of freedom:

$$\psi_4(t) = \ddot{h}_+^{TT}(t) + i\ddot{h}_x^{TT}(t) \quad (3.10)$$

with the plus- and cross-polarizations of the GW strain.

### 3.2.2 Implications for the accuracy of numerical waveforms

There are numerous sources potentially limiting the accuracy of a waveform computed from a typical numerical relativity evolution. A direct implication for wave extraction follows from the validity of the identification of  $\psi_4$  with outgoing gravitational radiation. The error from finite extraction radius is determined by how well one approximates the weak field regime, where the identification is valid. The desired accuracy of our diagnostic, namely  $\psi_4$  dictates how far away from the source one has to extract gravitational waves. See [80] for a detailed investigation.

A second ingredient which limits waveform accuracy in numerical relativity is truncation error. The finite difference computations, the Runge-Kutta time integration, interpolation and integration routines all have a finite accuracy at a fixed grid spacing  $h$ . This results in uncertainties in the tracking of the position of the compact objects which is a reliable diagnostic for how accurate the emission process was computed. Once generated, metric dynamics are propagated again with finite accuracy to the wavezone where they can be identified with GWs. In summary, these and other effects add up in a non-trivial way leading to a finite accuracy when computing the Weyl tensor and thus the numerical waveform.

The outer boundary conditions may also affect wave extraction when it is imposed not far enough away. The assumptions behind the boundary conditions induce unphysical features which in a hyperbolic system propagate inside the domain. If the outer boundary is close enough relative to the runtime of the simulation these artefacts affect the dynamics in the wave extraction zone. Also constraint violations and grid noise are typically reflected by these boundary conditions instead of absorbed.

We have already discussed the benefits and drawbacks from a box-in-box AMR mesh refinement. Here we stress that particularly for the wave propagation the AMR refinement boundaries give rise to a large uncertainty which converges only slowly away with resolution.

### 3.2.3 Sphere integration - Simpson vs. Gauss-Legendre

One may decompose the gravitational waves in a basis of spin-weighted spherical harmonics  ${}^{-2}Y_{lm}$  (which can be found e.g. in Appendix D of [39]). It turns out that the GWs as well as the radiated energy from an inspiralling binary are dominated by the  $l = 2, m = 2$  mode.

In order to perform this decomposition of  $\psi_4$  one needs to interpolate onto and integrate over a sphere. There are many different ingredients potentially influencing the quality (i.e. precision) of the numerical waveform. It is thus not trivial which of these steps is the main bottleneck. The integration over the sphere is done so far using the Simpson rule. For the integration along the periodic  $\phi$ -domain this is certainly a good choice, because any integration scheme that is based on polynomial interpolation, also the trapezoidal rule, converges exponentially on periodic domains. The reason is that the error terms of these schemes are given by the MacLaurin formula. What makes the trapezoidal rule second order and the Simpson method 4th order accurate in general are the boundary terms. When these terms vanish or cancel each other because of periodicity the convergence is as rapid as that of a spectral method [81].

For the  $\Theta$ -domain, however, the Simpson rule is only 4th order accurate and one might wonder whether this has a limiting impact on the overall accuracy of the wave extraction. For this reason we implement a spectral sphere integration scheme, a Gauss-Legendre quadrature, which is more accurate than the usual Simpson quadrature adopted in all numerical relativity codes.

**Definition** A Gauss-Legendre quadrature is an approximation to the integral  $\int_a^b Wf \approx \sum_i w_i f_i(x_i)$  where the  $x_i$  are given by the roots  $x_i$  of the Legendre-Polynomials  $P_l(x_i) = 0$  and the weights  $w_i = \frac{2}{(1-x_i^2)(P_l'(x_i))^2}$  [82].

A Gauss-Legendre quadrature is a special class of Gauss-Jacobi integration and as such is  $2N-1$  order accurate. It converges spectrally when the integrand is smooth [83, 84]. Elementary examples show that any departure from smoothness slows down the convergence rate significantly. This should not be an issue for wave extraction as GWs are smooth, but one might be worried about the two singular poles on the sphere.

Investigations have shown that the errors in the  $l = 2, m = 2$  waveforms of an equal mass, non-spinning black hole binary are not affected by a more accurate sphere integration. The conclusion is that the  $\psi_4$ -data on the cartesian grid already

and presumably the metric itself are not accurate enough for the improvements in the sphere integration to take effect.

This consideration demonstrates that the search for improvement in accuracy becomes an easier task with a potential source of uncertainty removed. Moreover, it is to be expected that differences between the two methods eventually manifest for more accurate simulations or whenever small wavelength structures are integrated as for instance higher modes of GWs.

### 3.3 Convergence and error estimates

The discretization (with grid spacing  $h$ ) of a PDE corresponds to a Taylor expansion of the exact (typically unknown) continuum ( $h \rightarrow 0$ ) solution  $s_0$  in powers of  $h$

$$f_h = f_0 + \sum_{i=1} c_i h^i \quad (3.11)$$

where  $c_i$  are coefficients independent from the grid spacing  $h$ . Just like in the analytic case one has to check whether the expansion converges to the continuum solution. When the grid spacing of the numerical grid are within the convergence radius of the (truncated) Taylor expansion the numerical solution converges to the continuum answer at the order which is consistent with the numerical scheme implemented.

To validate convergence one assumes that the error is dominated by a leading order term with a coefficient that does not depend on  $h$  in the above Taylor expansion

$$f_h = f_\infty + ch^p \quad (3.12)$$

where  $p$  is the order of accuracy. In the (rare) case that the analytic solution is known one can eliminate the coefficient with two simulations with the exact same setting but different  $h$ , in the more realistic case where the analytic solution is unknown one needs three resolutions. Let us assume we have carried out three simulations with solutions  $s_1, s_2, s_3$  and different resolutions  $h_1, h_2, h_3$ . Then the differences  $s_2 - s_3$  and  $s_1 - s_2$  should satisfy:

$$\frac{s_3 - s_2}{s_2 - s_1} = \frac{h_3 - h_2}{h_2 - h_1} \quad (3.13)$$

Thus convergence of  $n^{th}$  order is achieved if the differences due to resolution behave in exactly the way given by the analytical expression above. Convergence is a necessary condition for having error estimates, because otherwise one never knows

### 3 Physical observables

how drastically the results change when the resolution is increased further.

A further consistency check is to verify the  $1/r$  fall-off of  $\psi_4$ . This test is just as important as it tests whether  $\psi_4$  can be identified with a GW. We analyze the deviations from the expected fall-off by computing  $\psi_4$  at different radii. We compare the rescaled values  $r_{extr}\psi_4$  where  $r_{extr}$  is the radius of our extraction sphere at different  $r_{extr}$ . In Fig. 3.1 we show a convergence plot for one of our black hole binary case. Performing three simulations and changing the resolution while fixing everything else yields the differences shown in the Fig. which scale in agreement with a 4th order convergence. This is expected as the time integrators or wave extraction routines are 4th order accurate. We note that in principle there are lower order contributions which in general do not seem to cause issues, i.e. have a very small coefficient  $c_i$ . The puncture itself is only a  $C^2$  function. For computational efficiency the time interpolation for the Runge-Kutta substeps is only second order. Berger-Oliger timestepping is another second order ingredient.

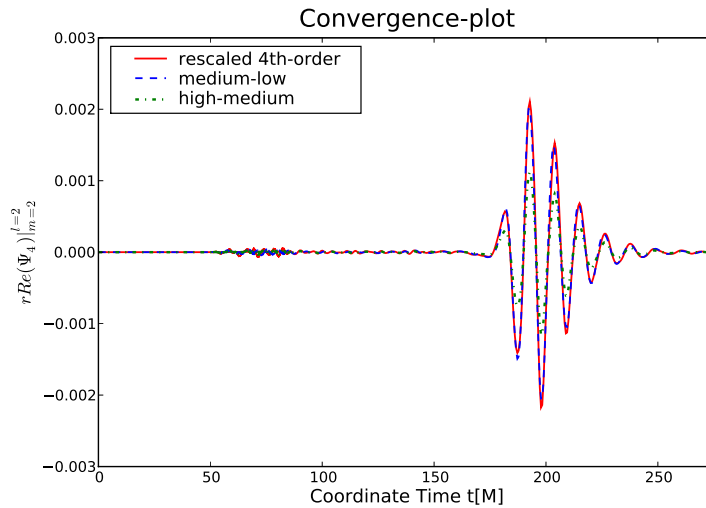


Figure 3.1: Convergence plot for a  $P = P_{qc}$ ,  $\Theta = 40^\circ$  of the 22-mode of  $r\psi_4$ . The blue dashed line shows the difference of  $r\mathcal{R}e(\psi_4)|_{m=2}^{l=2}$  as computed from the medium and low resolution data. Similarly, the green (dashed dotted) line for high and medium resolution. The solid line rescales the latter one assuming 4th order convergence. Both lines lie on top of each other demonstrating overall consistency of our results. The small noise at the beginning is due to the spurious junk radiation in our conformally flat initial data.

# 4 Black hole binaries on eccentric orbits

In this chapter we will introduce the two-body problem of GR and discuss the relevance, in particular that of eccentric binaries, to Gravitational Wave Astronomy. Then we will report our results on our numerical study of eccentric black hole binaries.

## 4.1 The two-body problem of GR

Two analytic solutions to the field equation of GR have particular astrophysical relevance, the Schwarzschild- [14] and the Kerr spacetime [85]. They are the only solutions of a well tested theory describing the stability of many known objects in the universe known as black holes. Both solutions are stationary and therefore do not contain gravitational radiation.

Since black holes are expected to reside at the center of almost every galaxy, which are known to collide with each other, suggests that single isolated black holes are not the only observationally relevant case. The gravitational field of two black holes is thus not only interesting as a theoretical problem in its own right, but is relevant from an observational point of view. The non-linearity of GR and the resulting lack of a superposition principle render this task a highly challenging one. In fact, it is an on-going active field of research that was starting several decades ago and is also called *the two-body problem of GR*. It consists of computing the metric of two massive objects orbiting around each other by solving Einsteins field equation.

There has been substantial progress in both analytical and numerical studies of the two-body problem in GR. A major breakthrough in analytic methods was the computation of two point masses in a weak-field approximation in 1963. Numerical evolutions were only recently accomplished in various regions of the underlying parameter space. Understanding the two-body problem of GR in more general sce-

narios remains an important challenge in order to test our understanding of gravity.

### 4.1.1 Relevance to GW astronomy

One fundamental difference between Newtonian theory and GR is gravitational radiation. Here we discuss insights that can be gained from a perturbative treatment that will lead to implications for the astrophysical relevance of binary systems.

Assuming slow motion and weak gravitational fields the power radiated is proportional to the third time derivative of the mass-quadrupole moment

$$L_{GW} = -\frac{dE}{dt} = \frac{1}{5} \left\langle \ddot{\mathcal{T}}_{ij} \ddot{\mathcal{T}}^{ij} \right\rangle \quad (4.1)$$

where  $\mathcal{T}$  is the trace-free part of the second moment of the mass distribution [39]. For this reason binary systems of compact objects are naturally strong sources for GWs because due to the compactness their mass distribution is most dynamical. In fact, the first (indirect) confirmation of the existence of gravitational radiation was discovered in a binary pulsar [86, 87]. The measured decrease in the orbital period matches perfectly the prediction of radiation losses due to gravitational waves.

Note, that astrophysically there is a complicated interplay of different effects that determine the evolution of a *realistic* binary. A simple estimate of the timescale of gravitational wave emission yields

$$\frac{t_{Merger}}{t_{Hubble}} \approx \frac{M}{M_{\odot}} \left( \frac{R_0}{10^6 R_s} \right)^4 \quad (4.2)$$

where  $R_0$  is the initial orbital radius. A binary of two  $10^9 M_{\odot}$  black holes on circular orbits must be as close as  $1pc$  in order to merge within the Hubble time. From this estimate one can also see that for smaller separations the time scale for gravitational wave emission becomes shorter. Hence it will eventually dominate the orbital evolution compared to other competing effects. In this last stage it is thus (at least in general) not unreasonable to assume vacuum spacetimes also to describe realistic binaries (e.g. those in gaseous environment).

The simplest way of taking radiation losses into account is to assume Newtonian dynamics but include energy losses according to equation 4.1. The prescription is valid as long as motion is slow compared to the speed of light and the gravitational field is weak. This approach was chosen by Peters and Mathews in 1963 [26, 27]. In this work the equations of two orbiting bodies under their mutual gravitational

interaction were derived and solved. Just as a single black hole is uniquely defined by their mass and spin a spacetime containing two black holes are correspondingly determined by the mass ratio, individual spins and the orbit. In the Newtonian theory the latter can be parameterized by the eccentricity  $e$  and the semi-major axis  $a$ . The equations derived by Peters and Mathews read

$$\begin{aligned}\left\langle \frac{d\epsilon}{dt} \right\rangle &= -\frac{304}{15} \frac{m_1 m_2 (m_1 + m_2) \epsilon}{a^4 (1 - \epsilon^2)^{5/2}} \left( 1 + \frac{121}{304} \epsilon^2 \right) \leq 0 \\ \left\langle \frac{da}{dt} \right\rangle &= -\frac{64}{5} \frac{m_1 m_2 (m_1 + m_2)}{a^3 (1 - \epsilon^2)^{7/2}} \left( 1 + \frac{73}{24} \epsilon^2 + \frac{37}{96} \epsilon^4 \right) < 0\end{aligned}$$

where the brackets are averages over an orbital period. This result has important implications for a binary system: In the linear, slow-motion regime eccentricity is a monotonically decreasing function of time and circularizes the orbit on timescales typically shorter than the inspiral time scale. Ever since circularized orbits have been considered astrophysically most relevant.

Note that due to the energy loss to GWs the orbits are never perfect circles but always have a finite radial velocity component. Sufficiently far away this component is very small defining the notion of *quasi-circular orbits*, which are the most studied ones in the literature, e.g. [88, 89, 90, 91, 92, 93, 21] and references therein.

After these first computations of GWs from bound eccentric binaries Turner computed GWs from parabolic encounters in 1977 [94]. Most radiation however originates from a region where these calculations must be regarded inaccurate. It is thus desirable to compute GWs from these systems with the tools of numerical relativity.

In the GR two-body problem eccentricity is always accompanied by precession of the orbital ellipse of the bodies. The leading order precession effect in the test-mass limit is well-known and tested most accurately with measurements from the precession of Mercury in the gravitational potential of the sun, see e.g. [95] to be:

$$\Delta\phi = -\frac{6\pi a}{p} \tag{4.3}$$

In the strong-field regime this simple relationship is lost. The radiation losses will be significant and not adequately captured by geodesic motion. Non-linear contributions to the dynamics may give rise to a completely different solution, hence higher-order perturbations or Numerical Relativity have to be considered for such investigations.

### 4.1.2 Higher-order perturbation theory

In order to obtain more quantitative estimates one may go beyond linear order in the perturbation theory and expand Einstein's equation consistently in higher powers of  $(v/c)$ . In this expansion the effect of energy loss due to gravitational radiation arises at the  $\mathcal{O}((v/c)^5)$ -order. Post-Newtonian expansions are computed in very different ways and are known up to  $\mathcal{O}((v/c)^6)$ -order and higher in some cases. For higher orders two conceptual problems appear. First, there is strong evidence that the Post-Newtonian [96, 97] expansion, in general, is not a convergent series, but an asymptotic one. That is it yields more accurate results when higher orders are included up to a finite order and then starts to diverge. Second, for higher orders at some point there is some ambiguity resulting in free parameters that must be fixed. In the Effective-One-Body [9, 10] method one uses resummation techniques to improve the convergence of the Post-Newtonian expansion. Furthermore there are parameters built in the model that can be calibrated to numerical results to incorporate non-perturbative information.

Within both formalisms neutron stars and black holes are usually represented as point particles which is another simplification that breaks down near the merger. Especially orbits with high eccentricities are more demanding than quasi-circular inspirals due to higher orbital velocities and enhanced tidal effects during pericenter.

Both perturbative approaches have reached a mature state and achieve impressive agreements sometimes beyond their expected range of validity [98]. The fundamental assumption of slow motion  $v \ll c$  is a fairly good one for the most part of the binary's orbital evolution. Thus, it should not be surprising that perturbative methods are very accurate for the most part of the inspiral.

### 4.1.3 Relevance of eccentric binaries

Despite the strong arguments favoring quasi-circular binaries there is growing literature on the astrophysical relevance of tight (i.e. relativistic) eccentric binaries. The challenge consists in finding mechanisms which allow binaries to become tighter against the strong circularizing effect of GW emission while at the same time retaining (over the evolution) or amplifying (in the late stages) the orbital eccentricity. If such systems do not circularize before reaching the strong-field regime an increase in eccentricity is a rather generic effect [99]. Overall one may classify scenarios which may give rise to tight eccentric binaries into three categories:



- N-body effects in dense stellar environments
  
- Galaxy mergers
  
- Interaction with gaseous environments

N-body processes may occur in dense stellar environments, for example in globular clusters or near the galactic center. The non-linear outcome of globular cluster dynamics [100, 101, 31, 102, 103] gives rise to many highly eccentric black hole binaries and ejections thereof. Stellar scattering events near supermassive black holes in the center of galaxies [29, 30, 104, 105, 106, 107, 28, 108, 109, 110] and tidal disruption of inspiralling binaries by means of the Hill mechanism can leave highly eccentric orbiting black holes while ejecting the other. In [32] it was shown that a body orbiting around an inner binary may excite oscillations and growth of the eccentricity of the inner binary due to orbital resonances. Three black hole systems have also been studied in numerical relativity and Post-Newtonian expansion, see for example [111, 112].

Highly eccentric, tight binary black hole configurations seem to be the rule rather than the exception in galaxy-merger scenarios [113, 106, 114]. There is also observational evidence that binaries of supermassive black holes do *not* always circularize before merger. The brightness of the well-known quasar source OJ287 exhibits variability including a 12 $yr$  period since more than a century. In [115, 33] the data was fitted using a Post-Newtonian model of a supermassive black-hole binary where the more massive black hole is surrounded by an accretion disk. The periodic outbursts occur everytime when the smaller black hole passes through the accretion disk of the larger one. The fit converged yielding a mass ratio of  $q \equiv m/M \approx 1/127$ , a large eccentricity and a small semi-major axis  $a \approx 0.06pc$ . The resulting pericenter precession is as large as  $40^\circ$  per orbit. These inferred orbital parameters reveal that, at least some small eccentricity will be present at the time of merger.

We may thus conclude, that, although a black hole binary considered in isolation will circularize, in realistic astrophysical settings many effects may occur to induce - possibly even strong - eccentricities. Thus a detailed investigation of eccentric binaries is mandatory to match theoretical predictions with observations in gravitational wave astronomy.

## 4.2 Results for quasi-circular orbits from Numerical Relativity

Early results from numerical relativity lead to discoveries of new effects and have guided purely analytical approaches. We will therefore review selected findings from Numerical Relativity [116, 21] on quasi-circular orbits before returning to the eccentric case.

Since several years the regime of *equal-mass, non-spinning* binaries on *quasi-circular* orbits is well understood. The main reason is the low resolution requirements due to the more comparable length scales. The black holes spiral in under radiation losses, enter a plunge phase at some point and merge to form a distorted merger remnant which exhibits the ring down of its quasi-normal modes to asymptote to a Kerr black hole with spin  $a/M^2 = 0.69 \pm 0.02$ . During the whole process  $\approx 4\%$  of the initial ADM mass of the spacetime is radiated away in gravitational waves. In the meantime more than 30 orbits can be computed by the Caltech/Cornell group [117] using pseudo-spectral methods, which enables a detailed comparison with perturbative methods and an accurate error analysis.

Treating unequal masses, larger momenta and/or spin necessitates a higher resolution due to sharper gradients that need to be resolved on the grid.

In the *unequal-mass* case it was found that there is a final kick or recoil of the remnant black hole. This effect is a consequence of conservation of linear momentum together with an isotropic radiation. To compensate the beamed, directed emission of linear momentum in the GWs the center of mass moves in the opposite direction. The magnitude of the kick in the non-spinning and quasi-circular case obeys the Fitchett formula [118]

$$v_{kick} = A\eta^2\sqrt{1 - 4\eta}(1 + B\eta) \quad (4.4)$$

with  $A \approx 1.210^4$  and  $B \approx -0.93$  and the symmetric mass ratio  $\eta = q/(1 + q)^2$ . The maximum of  $v_{kick} \approx 175\text{km/s}$  occurs for a mass ratio around 1 : 3. The largest mass ratio studied so far is  $q = 1/100$  [25] and yields good agreements with results from extreme mass ratio inspirals.

Recently simulations achieved much larger  $v_{kick}$  if the individual black holes have spin. The largest kick reported is from a configuration where the two spins of the black holes are anti-aligned but both lie inside the orbital plane giving a kick of  $v_{kick} \approx 2500\text{km/s}$ . In hyperbolic encounters  $v_{kick} = 10000\text{km/s}$  have been observed

[119]. This is a very interesting result because it allows supermassive black holes to leave their host galaxies, even if these are giant elliptical ones. In cases where the kick is not large enough the supermassive black hole may still be forced out of the equatorial plane of a spiral galaxy inducing perturbations on the disk [120].

The astrophysically interesting case where the black holes have spins has also been studied, with 0.97 the largest reported value [24]. Investigations involve orbital hang-up leading to characteristic waveform features. First successes in sampling the huge parameter space better have been achieved.

### 4.3 Beyond quasi-circular orbits

The first successful simulation [17] of two black holes including merger and ringdown by Frans Pretorius was in fact a configuration with significant eccentricity. In the following [19] analogies were found between evolutions of extreme eccentricity cases to unstable circular orbits.

### 4.4 Zoom-whirl regime

Zoom-whirl orbits arise as a purely relativistic phenomenon of the GR two-body problem. The term “zoom-whirl” stems from the peculiar fact that these orbits undergo an extended passage through pericenter, i.e., beyond the motion in a Newtonian potential with potentially arbitrarily many orbits followed by a phase where the orbits separate to apocenter in a repeating manner. This property makes these kind of orbits fascinating GW sources because of the correspondingly unique waveform signatures. Their astrophysical relevance is currently under debate. In view of the efficient circularizing effect of gravitational radiation on a binary orbit in the weak-field regime one must conclude that zoom-whirl orbits occupy a small size of the total parameter space. Estimating the actual size of this region is thus a crucial problem that needs to be solved with numerical relativity.

#### 4.4.1 Definition and origin

In the context of geodesic calculations zoom-whirls are defined as eccentric orbits close to the separatrix of stable bound orbits [121].

A proper definition of the term *zoom-whirl* in the non-linear regime is not as

straightforward. In [19] the authors have given a precise definition of the whirl phase as perturbations of unstable circular orbits and computed the corresponding Lyapunov exponents describing the critical behavior near the threshold of immediate merger.

For orbits with larger pericenter distance there will simply be a large pericenter precession. The precession effects are accompanied by a longer time spent at pericenter to justify the term fractional whirl. One should keep in mind though that the analogon to whirl orbits in the sense of [121] can be found inside the innermost stable circular orbit of Schwarzschild spacetime.

The close connection to unstable circular orbits leads to the expectation that zoom-whirl behavior is particularly relevant for high eccentricities (small pericenter distances). As we shall demonstrate it is not limited to that regime, but applies to a larger class of systems.

In this thesis, we explore the zoom-whirl regime of comparable mass non-spinning black hole binaries.

#### 4.4.2 Relevance of zoom-whirls

Whether zoom-whirl orbits are of relevance to gravitational wave (GW) astronomy depends on several factors. Even if the signals are stronger, if excessive fine-tuning is required, then the population of strong sources might amount to a very small corner of parameter space. Conversely, if little tuning is involved, then zoom-whirl orbits can be potential GW sources even for ground-based detectors, see [108, 109, 28, 31] and references therein.

As we will show, zoom-whirl orbits are not as rare as one may think, see also the discussion in [122]. In the cores of globular clusters measurements indicate isotropic velocity distributions at the cluster core and a King profile [123] at larger radii, see [124] for the globular cluster 47 Tucanae. Astrophysically, the linear momentum in these binaries is not arbitrarily large, which is why we limit our study to “low” momentum (between the momentum of circular orbits and six times that value). For a rough estimate let us assume that some of the relevant processes leading to large eccentricities effectively produce a uniform random distribution of eccentricities.

In this work we show that for such binaries up to one complete whirl can be observed during the last encounter just before merger within a fine-tuning interval of the angle on the order of one degree or  $\Delta e \approx 0.01$  at an initial separation of  $D = 20M$ . We emphasize that there exists a discrete fine structure such that for a

given  $D$  the regions where whirls happen are *disjunct* consisting of  $N$  intervals  $\Delta\Theta$  or  $\Delta e$ , equivalently. Hence a fraction of  $N\Delta e$  of such eccentric binaries can show a whirl effect. The number  $N$  depends on the sensitivity of the detector because whirl signals will become weaker for lower eccentricities and eventually are suppressed. So for example, if the detector is sensitive to the whirl signal of the lowest eccentricity ( $P = 1P_{qc}, \Theta = 60^\circ$ ) case of our data set, then  $N = 7$ , because the whirl occurred during the 7th encounter. The detector would then also see the stronger whirls of the evolutions that have less encounters  $48^\circ < \Theta < 60^\circ$  (see Figs. 4.9, 4.23). So in this simplified discussion we conclude that  $\approx 7\%$  of the eccentric black hole binaries in the cores of globular clusters merge through a whirl phase. For a real estimate one has to include a realistic distribution of eccentricities, unequal mass and spin effects. Furthermore, one has to study the dependence of our  $\Delta e$  estimate on the separation.

As GWs carry away orbital energy, an infinite number of whirl orbits cannot be obtained. Thus, a small part of the parameter space is not accessible.

In any case, as a matter of principle we should be prepared to detect and recognize GWs from all corners of parameter space including zoom-whirl orbits.

### 4.4.3 Illustration using geodesics

Zoom-whirl behavior can be seen in the geodesic limit. To illustrate the effect, we consider a test particle in Schwarzschild spacetime. With  $(t, r, \phi)$  being the spherical Schwarzschild coordinates and  $M$  the mass of the black hole the equations of motion for a time-like geodesic are a set of coupled second-order non-linear PDE and read

$$\dot{\phi}(t)r(t) = -2\dot{r}(t)\dot{\phi}(t) \quad (4.5)$$

$$M\dot{r}^2(t) + r^2(t)\left(1 - \frac{2M}{r(t)}\right)\ddot{r}(t) = M\left(1 - \frac{2M}{r(t)}\right). \quad (4.6)$$

For a special choice of initial conditions the test particle approaches the innermost stable circular orbit exhibiting several orbits before it finally escapes (see Figure 4.4.3) or merges. This outcome depends on the distance to the threshold. At threshold we can thus, in principle, construct a geodesic with an infinite number of whirls.

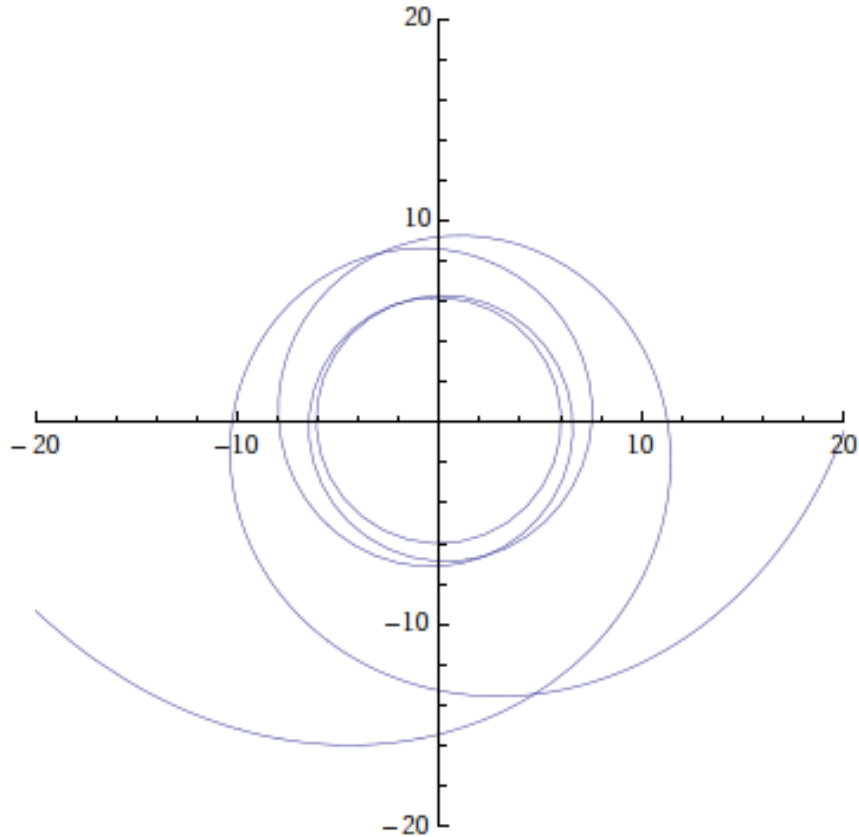


Figure 4.1: Time-like geodesic in Schwarzschild spacetime tuned to threshold. The axis are the  $(x, y)$  coordinate inside the equatorial plane.

#### 4.4.4 Eccentric binaries

Before we study eccentric binaries and zoom-whirl orbits in more detail, we summarize the literature in this area.

The basic features of zoom-whirl orbits were first discussed in the context of geodesics in a stationary black hole spacetime (e.g. [125, 126, 127]), in extreme mass ratio inspirals (e.g. [121, 128, 129]) and post-Newtonian (PN) evolutions [130, 131]. For geodesics, it is a matter of fine-tuning the initial parameters of the orbit to obtain a certain number of whirls. In fact, for geodesics the number of whirls can be made arbitrarily large since there is no gravitational radiation. Going beyond the test-mass limit, including radiation losses becomes a key task, e.g. [121, 132, 133].

Perhaps the main question about zoom-whirl orbits in GR is how the classic, well known picture of zoom-whirl geodesics changes for binaries with comparable masses in configurations where radiation damping becomes significant. Naively, we do not expect the binary to radiate away more than its total mass, i.e., the number

of orbits is finite since it is limited by the energy and angular momentum radiated away during each whirl. In fact, for comparable masses one might have questioned whether it is possible to obtain even a single (full) whirl. Since the whirls may happen at small separations, even inside the innermost stable circular orbit, such computations are problematic for (simple) PN approximations. However, recently fully general relativistic numerical evolutions of eccentric black hole binaries have indeed found whirl orbits, although the number of whirls in these experiments is less than three.

In [19], Pretorius and Khurana present the first example of a whirl orbit for an equal mass binary. In [134, 135, 136], several examples for the transition from inspiral to plunge are studied, investigating the radiated energy, angular momentum and the resulting final spin. In [136] longer evolutions with up to three (fractional) whirl plus zoom phases are studied. A first study of binaries with unequal masses and non-vanishing spin can be found in [137]. The notion of marginally stable circular orbits in background spacetimes was shown to be in close resemblance to whirl orbits in numerical evolutions of finite mass ratio [99, 19]. The consequences for kicks are addressed in [138]. Implications for data analysis are studied in e.g. [139]. The focus in [140, 141, 142, 143, 144, 145] is on high-energy collision. Among the key results so far is that the total energy radiated can easily exceed the 4% of the total mass radiated away during the last stage of a quasi-circular inspiral. For high-energy collision, up to  $35 \pm 5\%$  have been found [143]. In [146], we found multiple extrema in the radiated energy as a function of the initial data at low momentum, and that only a modest amount of fine-tuning is required to spot these extrema. These extrema should be compared to the variations in the mass and spin of the merger remnant noted in [147].

## 4.5 Black hole parameters

Here we describe the parameters that describe the initial data for black hole binaries. In this work we set the spins to zero. The input for the computation of the initial data is constituted by  $m_i$ , the (bare) puncture masses,  $\vec{P}_i$ , the momenta, and  $\vec{x}_i$ , the positions. Since the momenta are non-zero, we obtain smaller physical masses  $M_i$  at the inner asymptotically flat ends of the punctures. The difference between the masses  $m_i$  and  $M_i$  ranges from  $7 \cdot 10^{-3}M$  for  $1P_{qc}$  to  $3.5 \cdot 10^{-2}M$  for  $6P_{qc}$  and is essentially independent of  $\Theta$ . The total mass  $M$  is defined as  $M := \sum_i m_i$ . The

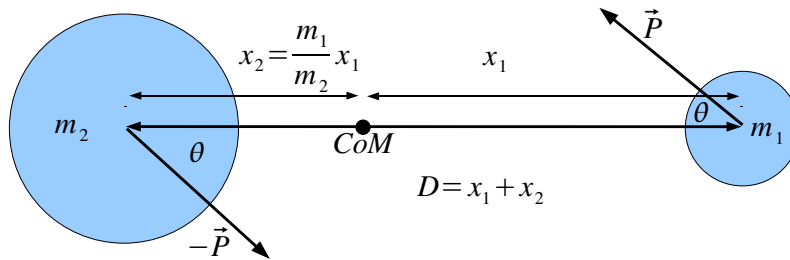


Figure 4.2: Here we illustrate our initial setup. CoM stands for the center of mass.

ADM mass at the  $i$ -th puncture and at infinity are

$$M_{ADM}^i = (1 + u(\vec{x}_i))m_i + \frac{m_1 m_2}{2D}, \quad (4.7)$$

$$\begin{aligned} M_{ADM}^\infty &= M_{ADM}^1 + M_{ADM}^2 + E_{bind} \\ &= m_1 + m_2 + \lim_{r \rightarrow \infty} (2ru), \end{aligned} \quad (4.8)$$

respectively, where  $u$  is the correction to the conformal factor in the puncture framework and  $E_{bind}$  the binding energy. Values for  $M_{ADM}^\infty$  range from 0.994 for  $1P_{qc}$  to 1.2 for  $6P_{qc}$ . Since the global mass scale in vacuum is arbitrary, the masses can be characterized by one number, for instance the symmetric mass ratio denoted by  $\nu = m_1 m_2 / (m_1 + m_2)^2$ .

We choose coordinates in which the punctures are initially located on the  $x$ -axis, see Fig. 4.2. For equal masses we set  $x_{1,2} = \pm D/2$  for a coordinate separation  $D$ . For unequal masses we leave  $x_1$  unchanged but set  $x_2 = x_1 m_1 / m_2$ . For the momenta we choose  $\vec{P}_{1,2} = \pm \vec{P}$ . This implies, together with the choice of  $x_{1,2}$ , that initially the center of mass is at rest and that mergers happen at the origin (except for a small merger kick due to unequal masses). Concretely, we consider momenta in the  $x$ - $y$ -plane given by their magnitude  $P$  and an angle  $\Theta$  such that  $\vec{P} = (-P \cos \Theta, P \sin \Theta, 0)$ . Specifying the “shooting angle”  $\Theta$  is equivalent to the choice of an impact parameter.

Given the above geometric configuration, numerical simulations are parameterized by specific choices for  $x_1$ ,  $\nu$ ,  $P$ , and  $\Theta$ . We set  $x_1 = 10M$  for all runs, which implies  $D = 20M$  for equal masses. For unequal masses, we position the larger mass at  $x_2$ , i.e.,  $M_2 > M_1$  and  $|x_2| < x_1$ . Most of the simulations we discuss are for equal masses ( $\nu = 1/4$ ), but we also consider a few examples for mass ratio 1:2 ( $\nu = 2/9$ ),



1:3 ( $\nu = 3/16$ ) and 1:4 ( $\nu = 4/25$ ). The magnitude  $P$  of the momenta is chosen as a multiple of  $P_{qc}$ , which denotes the magnitude of the momentum for a quasi-circular inspiral. Following [148], for equal masses at  $D = 20M$  we have  $P_{qc} = 0.061747M$ . We consider  $P/P_{qc} = 1, 2, \dots, 6$ , and as the most extreme case  $P/P_{qc} = 10$ . The direction of the momenta is given by  $\Theta \in [0, 90^\circ]$ . Here  $\Theta = 0$  corresponds to a head-on collision, while for quasi-circular inspiralling orbits  $\Theta$  is slightly smaller than  $90^\circ$  because the momentum has a small radial component. The case  $\Theta > 90^\circ$  with initially radially outgoing motion can be ignored <sup>1</sup>.

For the main part of this work, we first choose a specific mass ratio, in particular we choose between equal and unequal masses. Second, we choose one of several (low) momentum cases. Third, we vary the shooting angle systematically, in particular searching for maxima and minima in the total radiated energy, examining the number of whirls, etc. There are some obvious alternatives to set up such parameter scans, for example fixing  $\Theta$  [136], using some measure of eccentricity, the angular momentum [147], or the binding energy [134] as parameter. Apart from having a simple interpretation as a scattering experiment with fixed momentum size, our setup also describes simulations at roughly constant total energy, if in analogy to classical point masses the total energy is defined as the sum of the kinetic and potential energy (since  $P$  and  $D$  are constant while varying  $\Theta$ ). Each run amounts to 500 – 30000 CPUh (the latter one for  $1P_{qc}, \Theta = 60^\circ$ ), which is strongly dependent on how far and how many times the orbits zoom out. We implemented Brent’s method [149] to bracket local extrema in the efficiency of converting energy into outgoing gravitational radiation, for which a small number of runs sufficed. This reduced the total number of runs to about a 130 while still sampling the parameter space in an adaptive and accurate way. In retrospect, we found that a golden section search [149] is, for the finite accuracy we required, a better choice despite being only first order convergent. The parabolic interpolation inside Brent’s method chooses the new guesses systematically towards the flatter part of the asymmetric maxima.

## 4.6 Numerical results

To prime the discussion of the orbits, we first consider several examples of puncture tracks for equal mass binaries with  $P = P_{qc}$  and  $P = 5P_{qc}$ , see Figs. 4.3 – 4.7. Shown

---

<sup>1</sup>Generally speaking, if such an orbit is unbound then the black holes separate without close encounter. If bound, then after reaching the first apocenter the orbit becomes inward-bound, which in principle is already included for  $\Theta \in [0, 90^\circ]$ .

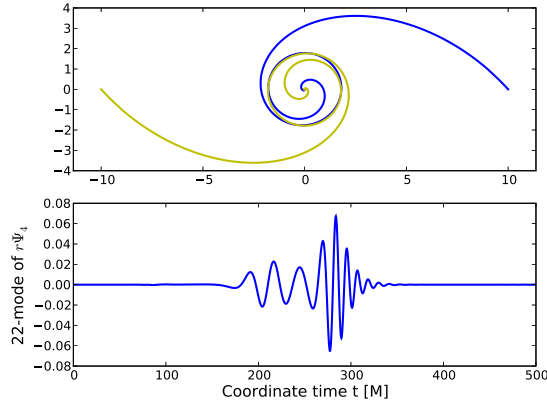


Figure 4.3:  $P = P_{qc}$ ,  $\Theta = 48^\circ$ . There is about one full whirl in a range of  $\pm 1^\circ$  around this shooting angle followed by the merger. The waveform clearly shows a wave associated with the whirl, and its amplitude is smaller than that of the ensuing merger signal. The diameter of the whirl is a little smaller than that of the innermost orbit of a quasi-circular inspiral.

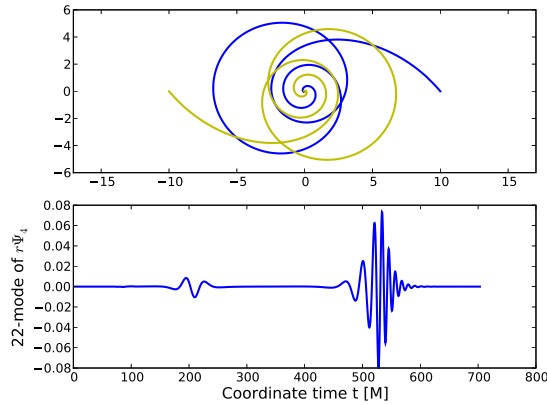


Figure 4.4:  $P = P_{qc}$ ,  $\Theta = 50^\circ$ . For a shooting angle slightly larger than that leading to the strongest whirl, there is about half a whirl, followed by a zoom out to about three times the whirl diameter, followed by a short inspiral and merger that starts with significantly reduced eccentricity. Note the comparatively small and short wave pulse associated with the whirl, again at about  $200M$  of evolution.

are the puncture tracks in the  $x$ - $y$ -coordinate plane in the upper panels, and the 22-mode of the waveforms in the lower panels. The waveforms are further discussed in Sec. 4.6.2. The figures show two sequences of runs for the two momenta that explore how the orbits change when the shooting angle is varied from small to large.

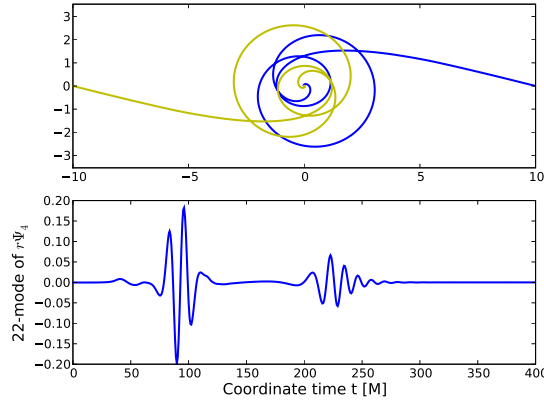


Figure 4.5:  $P = 5P_{qc}$ ,  $\Theta = 14.15^\circ$ . Example for initial momentum which is significantly larger than that of quasi-circular orbits, and which can easily produce unbound orbits. Zoom-whirl orbits are found for much smaller shooting angles than in Fig. 4.3 and 4.4. There is one whirl, and a short zoom followed by a merger. Due to the additional kinetic energy, the whirl signal increases in amplitude and exceeds the merger signal.

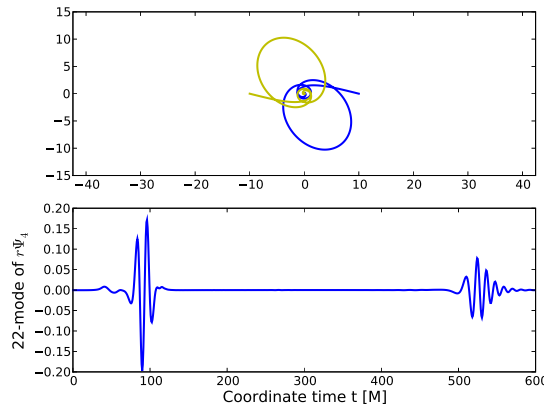


Figure 4.6:  $P = 5P_{qc}$ ,  $\Theta = 14.20^\circ$ . The larger the momentum, the more sensitive the orbit becomes to the choice of the shooting angle. A small change in angle compared to Fig. 4.5 leads to a much larger zoom phase even though the initial whirl is almost unchanged.

## 4.6.1 Orbital phenomenology

### Classification of orbits

For any choice of the mass ratio  $\nu$  and initial separation  $D$ , we can in principle fill in a “phase-diagram” as shown in Fig. 4.8, which labels orbits in a  $P$ – $\Theta$  plot.

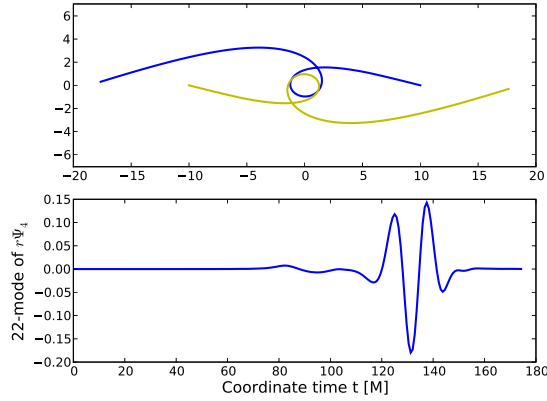


Figure 4.7:  $P = 5P_{qc}$ ,  $\Theta = 14.3^\circ$ . Enlarging the shooting angle further compared to Fig. 4.6 results in a whirl followed by a zoom to infinity (unbound orbit, no merger).

The main classification is whether initial parameters  $P$  and  $\Theta$  lead to orbits that are bound (implying capture and merger) or unbound (escape to infinity). In Newtonian gravity, we only have to check whether the kinetic energy exceeds the potential energy, or equivalently whether the binding energy is positive or negative. In general relativity, this distinction is only possible a posteriori since the gravitational waves and the associated loss of energy and angular momentum are only known after the Einstein equations have been solved. Solutions to the evolution problem define the dividing line  $P = P_{bu}(\nu, D, \Theta)$  in Fig. 4.8. Orbits with  $P > P_{bu}$  are unbound, orbits with  $P < P_{bu}$  are bound.

A simplified, a priori upper limit on the momentum  $P$  that ensures boundedness is  $\tilde{P}_b := P_{bu}(\nu, D, \Theta = 180^\circ)$ , which is independent of  $\Theta$ , see also Fig. 4.8. If the momentum  $P$  does not suffice to escape in the direction  $\Theta = 180^\circ$  (for which radiation losses are minimized), then the orbits are bound for all  $\Theta$ . Here we use the assumption that the black holes are not spinning. Approximating the minimal radiation loss in the “head-off” direction by zero, we compute a simple estimate of  $\tilde{P}_b$  based on the binding energy in equation 4.8. Fixing  $\Theta = 180^\circ$  and  $D = 20M$  we iteratively compute initial data with varying  $P$  to obtain the binding energy  $E_{bind}$ .  $\tilde{P}_b$  is then defined as  $\tilde{P}_b := P(E_{bind} = 0, \Theta = 180^\circ)$  resulting in  $\tilde{P}_b = 0.085(4 \pm 3)M$ . There is an error since we end the iteration after a few steps, and in addition radiation effects are ignored. For example, the momentum of the quasi-circular orbit leads to bound orbits for all angles since  $P_{qc} < \tilde{P}_b \approx 1.377P_{qc}$ .

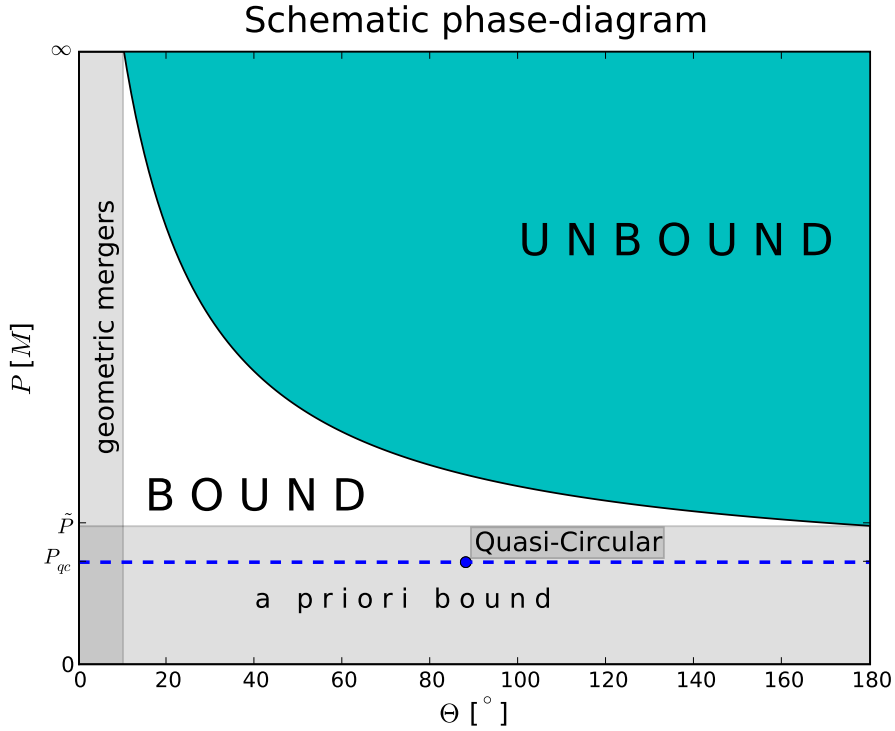


Figure 4.8: Here we show a sketch of the resulting phase diagram. The grey-shaded zones are formed by evolutions that can be shown to be bound without performing a numerical evolution.

Inverting  $P_{bu}(\nu, D, \Theta)$ , we define  $\Theta_{bu}(\nu, D, P)$ , the shooting angle between bound and unbound orbits, as a function of  $P$ . An a priori upper limit for bound orbits is given by  $\Theta_{geom} = \Theta_{bu}(\nu, D, P = \infty)$ , see Fig. 4.8. In practice it is tricky to study large  $P$  due to limitations in the construction of initial data. Conceptually, however, we can think of this limit as a geometric constraint based on the finite size of the black holes. The idea is that the two black holes must merge when their event horizons touch. Using Euclidean geometry,  $\Theta_{geom}$  is given by  $\sin \Theta_{geom} = d_{merger}/D$ , where  $d_{merger}$  is the separation of the punctures at the time of the merger. However, the size of the black holes depends on the gauge. The Schwarzschild radius for a mass  $m$  is  $2m$  in Schwarzschild coordinates,  $m/2$  for isotropic coordinates, and depending on the moving puncture gauge somewhere in between for the numerical evolutions. We therefore use the numerical result for  $d_{merger}$ . For equal masses we find that a common event horizon appears at a coordinate distance of about  $d_{merger} \approx 1.76$  to  $1.95M$  (with a slight drift towards smaller values with increasing momentum). This estimate leads for  $D = 20M$  to a geometrical limit of  $\Theta_{geom} =$

$10.5^\circ$  using the Euclidean formula. This limit does not appear to be very restrictive for low momenta, but it is not in contradiction to the runs of this study, either. All simulations with  $\Theta < \Theta_{geom}$  end in a merger.

Within the category of bound orbits there is a detailed classification scheme based on periodic orbits which is complete when neglecting radiation effects. In this classification [127, 130] one indexes all closed orbits with a triplet of integers  $(z, w, v)$ , where  $z$  is the number of zooms within an approximate  $2\pi$  period, i.e. the number of “leafs”,  $v$  is the stride over the leafs ( $1 \leq v \leq z - 1$ ), and  $w$  is the number of whirls. The total precession angle is  $2\pi(w + \frac{v}{z})$ . The question is whether this classification still works in an approximate sense for black-hole binaries with radiation effects. Especially near the merger of comparable mass black-hole binaries, the orbits shrink significantly and may not be well represented by a single periodic orbit, but rather by a sequence of them. Our findings imply that the longest whirls associated with the largest precession angles (largest  $w$ ) occur for momenta with  $P$  slightly larger than  $\tilde{P}$  and are very close to a precession of  $2\pi$ . We also find that the dependence on  $P$  is weak and beyond  $P \gtrsim 2P_{qc}$  compatible with the statement that it only depends on the mass ratio. Radiation damping seems to limit the length of the whirl phase for larger  $P$ , although there may be artifacts due to the initial data. In terms of periodic tables this means that we typically find preferred subsets of periodic orbits that approximate our evolutions best. The number of whirl-orbits  $w$  is clearly limited by the efficiency of gravitational radiation. For equal masses  $w = 1$  seems to be the largest  $w$  one can obtain. For larger mass ratios  $w = 2$  should also become possible somewhere beyond a mass ratio of 1 : 4. In the regime we are probing orbits with  $z = 2, z = 3$  and  $v = 1$  are favored. However, our data set contains too few data points on different mass ratios to make a strong statement.

### **Orbital dynamics**

We describe the main aspects of the orbital dynamics we find in our data set using the categorization introduced in the previous section.

All equal mass runs start at  $D = 20M$  ( $P = 10P_{qc}$  has  $D = 50M$ ) in such a way that  $D$  shrinks. Obviously, the following evolution depends on the values of  $P$  and  $\Theta$ . Starting with the **B** category we discuss the orbital dynamics from low to high  $\Theta$ . At low  $\Theta$  (or equivalently for high eccentricities)  $D$  monotonically shrinks leading to a rather prompt merger (as can be seen in the lower left insets of Fig. 4.11) without completing a single orbit. The runs with larger  $\Theta$  have correspondingly higher initial

orbital angular momentum and manage to resist the strong gravitational pull for longer so that the merger time steadily grows. For  $\Theta \approx 46^\circ$  the punctures complete one orbit before merger. At yet larger  $\Theta \gtrsim 48^\circ$  the orbits begin to exhibit a circular phase (the whirl) which is maintained for longer as  $\Theta$  is increased. However, at  $\Theta \approx 48.5^\circ$  the orbit leaves the circle again towards larger radii (the zoom) delaying the merger significantly. In this range of  $\Theta$  there is a high sensitivity on the initial data (concerning merger time as a function of  $\Theta$ ). A mild increase in  $\Theta$  leads to a much larger  $t_m$  because the black holes slow down as they move out before falling back. In the limit  $\Theta \rightarrow 90^\circ$  the (fractional) whirls become shorter while the apocenters and pericenters become increasingly degenerate. The pericenter grows with  $\Theta$ , hence the black holes do not cross their mutual gravitational potential as deeply and consequently not as much radiation occurs enabling more and more (fractional) zoom-whirl episodes. There is a completely smooth transition between full zoom-whirls and fractional ones (strong pericenter precession).

As a consequence of our setup, our evolutions start somewhere within the ellipse rather than in the apocenter, see right insets of Fig. 4.11. Despite that fact, one can see that the orbits exhibit a huge precession of roughly  $\pi$  or close to  $2\pi$  for  $\Theta = 48.5$  (followed by a tiny zoom). Even for the smallest eccentricity we studied, the  $\Theta = 60^\circ$  case, one can see that the shortest (fractional) whirls still have precessions as large as  $2\pi/3$ . Thus, over the course of the whole evolution the accumulated precession amounts to more than two entire orbits. Those values by far exceed the amounts of precession known from mildly relativistic systems like the famous Hulse-Taylor pulsar investigated in [86] with a precession of  $q = 0.0037^\circ$  per orbit or the binary pulsar [150] with  $q = 0.0044^\circ$  per orbit. These multiple, fractional whirl systems have correspondingly milder gravitational radiation. In these cases, we are able to find precession not only from one apocenter to the next but also precession of the multi-leaf clover as a whole. This is very similar to the findings in studies on periodic orbits [127, 130] (or nearby aperiodic orbits rather). This additional, peculiar precession effect is indeed small also for our evolutions, though not negligible.

Switching to the **U/B** category the additional possibility arises that the black holes just fly-by deflecting their trajectories and escape to infinity giving rise to the merger/ fly-by threshold (see insets in Fig. 4.12) which we will discuss later.

We again describe the orbital phenomenology from low to high values of  $\Theta$ . The qualitative features of low  $\Theta$  evolutions are the same as in the **B**-category. The actual values of  $\Theta$  that lead to analogous characteristics (one complete orbit, a

whirl, maximum in  $E_{rad}$ , etc. ) are inversely proportional to the momentum  $P$ . This is in agreement with the expectation that for larger  $P$  one has to shoot the black holes closer to each other compared to corresponding lower  $P$  evolutions in order to obtain qualitatively similar behavior.

Again, as in the **B**-category, the whirl phase is followed by a zoom for larger values of  $\Theta$ . Now there is a finite range in  $\Theta$ , depending on  $P$ , where the black holes do not escape to infinity, but reach an outer turning point (like in the **B**-type orbits) and fall back ending in a so-called 'delayed merger'. Beyond a certain (momentum dependent) value of  $\Theta_{U/B}$  the black holes are simply deflected or "fly-by" each other.

Inside the **U/B** category we only find orbits exhibiting whirls during the first encounter and never thereafter. This behavior agrees with the interpretation that too much angular momentum is radiated during the first whirl to have another whirl episode. One might believe that if the whirls were short enough, the angular momentum losses should be comparatively modest, hence multiple fractional whirls just like in the **B**-category should in principle also be possible. However, it turns out that (at least for our initial data sets) the black holes in those evolutions do not pass each other close enough to shed sufficient energy. In other words, the evolutions corresponding to the multiple zoom-whirls in the **B**-category are all unbound systems inside **U/B** and never come closer again.

We proceed by analyzing precession effects and discuss resemblances to periodic orbits. For a given  $P$  the precession angle shrinks with increasing  $\Theta$  when approaching the threshold as expected. The maximal amount of precession we find is slightly larger than in the **B** category.

We clearly recognize patterns known from periodic orbits. For the  $P = 2P_{qc}$  sequence we find  $z = 2, z = 3, z = 4$  orbits. The main difference to periodic orbits is that the orbits end in a merger after the first leaf has been traversed because of the severe radiation losses. For instance  $P = 2P_{qc}, \Theta = 25.1^\circ$  resembles the  $z = 3, v = 1, w = 0$  orbit with  $q = 2\pi/3$ . When decreasing  $\Theta$  only by small amounts, the arising orbits typically show the same amount of precession (only  $D_{per}$  shrinks with  $\Theta$ ). At some point there is a transition to another multi-leaf clover and the precession amounts to a value of  $q = \pi$  and is now similar to the periodic orbit labeled  $z = 2, w = 0, v = 1$ .

We were not able to find a full whirl with the black holes escaping to infinity, which is most probably due to excessive loss of energy during the long whirl. It is an open question whether this statement holds for general momentum  $P$ , but if it



occurs, then for momenta  $P > 6P_{qc}$ .

Among the open questions regarding orbital phenomenology of zoom-whirl orbits in full GR is how long the whirl phase can be, or how large the maximum precession is. Investigations regarding this question can be found in e.g. [19, 142, 143, 137]. Due to different initial data and also different tuning strategies these investigations have been performed in different regions in parameter space. Here we seek to give a rather comprehensive view on the complete picture.

Sharpening the above question we ask: Given a fixed  $P$ , what is the longest possible whirl phase and how does this maximal precession scale as a function of  $P$ ? Both the results of previous studies as well as our results strongly indicate that the answer to this question is given by the interplay between two competing effects, namely, the available angular momentum and the efficiency of gravitational radiation. For low  $P$  radiation turns out to be less efficient, see Figs. 4.10 and 4.11, so the more angular momentum is present, the longer the whirl phase can be. As a larger  $P$  also implies a larger angular momentum, we see that the whirl phases for intermediate values of  $P$  become longer as  $P$  increases. Beyond a critical value of  $P$  the effect of increasing efficiency of gravitational radiation becomes significant. During the whirl, angular momentum is radiated away very quickly. Thus, the duration of the whirl phase is limited due to radiation damping.

For a survey of this parameter space it is necessary to distinguish between bound and unbound orbits at a finite simulation time (i.e., without simulating impracticably long). We employ the binding energy  $E_{bind}$  for this purpose. Without gravitational radiation  $E_{bind}$  is a constant of motion and the orbits are unbound for  $E_{bind} > 0$  and bound if  $E_{bind} < 0$ . In full GR we distinguish bound from unbound orbits by comparing the initial binding energy  $E_{bind}(t = 0)$  with the total radiated energy after the first close encounter  $E_{rad}(t > t_{encounter}^{1st})$ . We consider the orbit to be bound if  $E_{bind}(t = 0) < E_{rad}(t > t_{encounter}^{1st})$  and unbound else. Note that this criterion should only be applied close to the threshold between bound and unbound runs, as it does not apply beyond this regime. The prime example to show a contradiction is a head-on collision as it merges although it will violate the criterium above. Every single piece of evidence indicates that this criterion holds, where we applied it. It shortens the runtime of the unbound runs significantly.

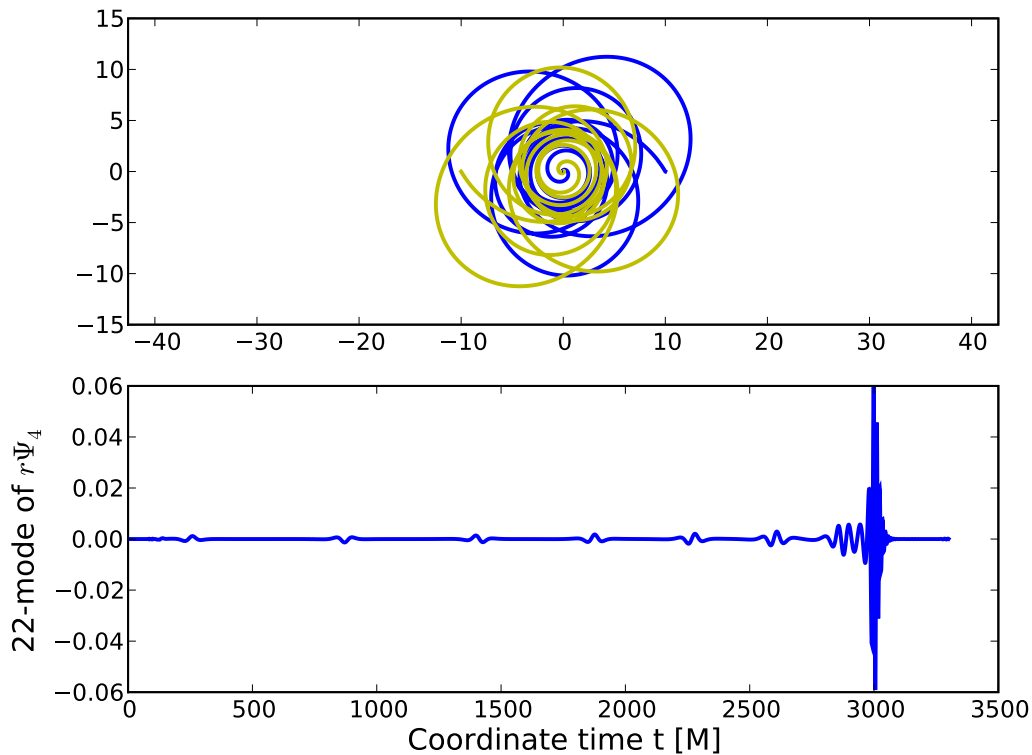
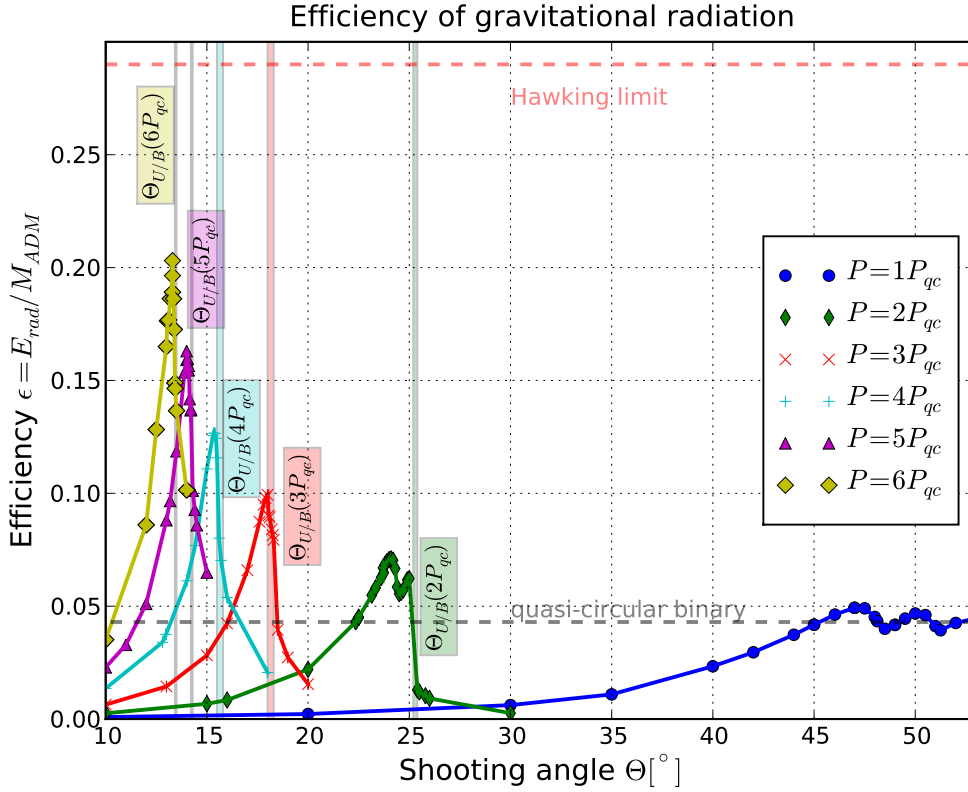


Figure 4.9:  $P = 1P_{qc}$ ,  $\Theta = 60^\circ$  case. This is the evolution with the lowest eccentricity in our data set (initially  $e \approx 0.55$ ). One can see that the orbital trajectories approximately trace out a 3-leaf clover. The orbital energy losses from one leaf to the next are apparent as the sizes of the leaves are shrinking significantly. At every close encounter the waveform exhibits a small burst-type signal which looks similar in shape to the calculation by [94], but is off in magnitude. Note that as the evolution proceeds the encounter bursts occur more frequently. The binary circularizes only partially and maintains an eccentricity  $e \approx (a-b)/(a+b) = 0.24$  shortly before the whirl phase. This demonstrates that whirl effects with strong waveform imprints can occur also for low eccentricities.

## 4.6.2 Radiation properties

### Waveforms

Here we demonstrate how the orbital dynamics as described in Sec. 4.6.1 are reflected in the GW signals. We discuss typical waveforms of a representative subset of our evolutions (see figs. discussed in Sec. 4.6.1). Our main focus is on the richness in information stored in eccentric black-hole binary waveforms in contrast to quasi-

Figure 4.10: Radiated energy for different  $P, \Theta$ .

circular ones. It is this aspect which allows to learn considerably more about the source compared to a quasi-circular black-hole binary. Already the 22-mode shows obvious differences which become larger in higher modes. For example, the  $l = 2$   $m = 0$ -mode of a quasi-circular orbits looks just like a smaller amplitude version of the  $l = 2$   $m = 2$ -mode. In the eccentric case we observe differences. For equal mass, non-spinning black-hole binary only even  $l$ -modes contribute. We have computed the  $l \leq 8$  modes and find that the  $l = 2$  is still the largest contribution, but  $l = 4$  has a significant contribution throughout the merger and  $l = 6$  and  $l = 8$  close to the maximum. Consequently parameter estimation works much better as more features in the signal tend to break degeneracies in parameter space [151].

One main difference between quasi-circular and eccentric waveforms is the presence of small bursts corresponding to close encounters at pericenter. Those small signals will be observable by instruments like LISA [152, 153, 154, 155] or the ET-telescope [156, 157] for commonly expected signal strengths.

Evolution that exhibit a whirl phase shortly before they merge behave slightly

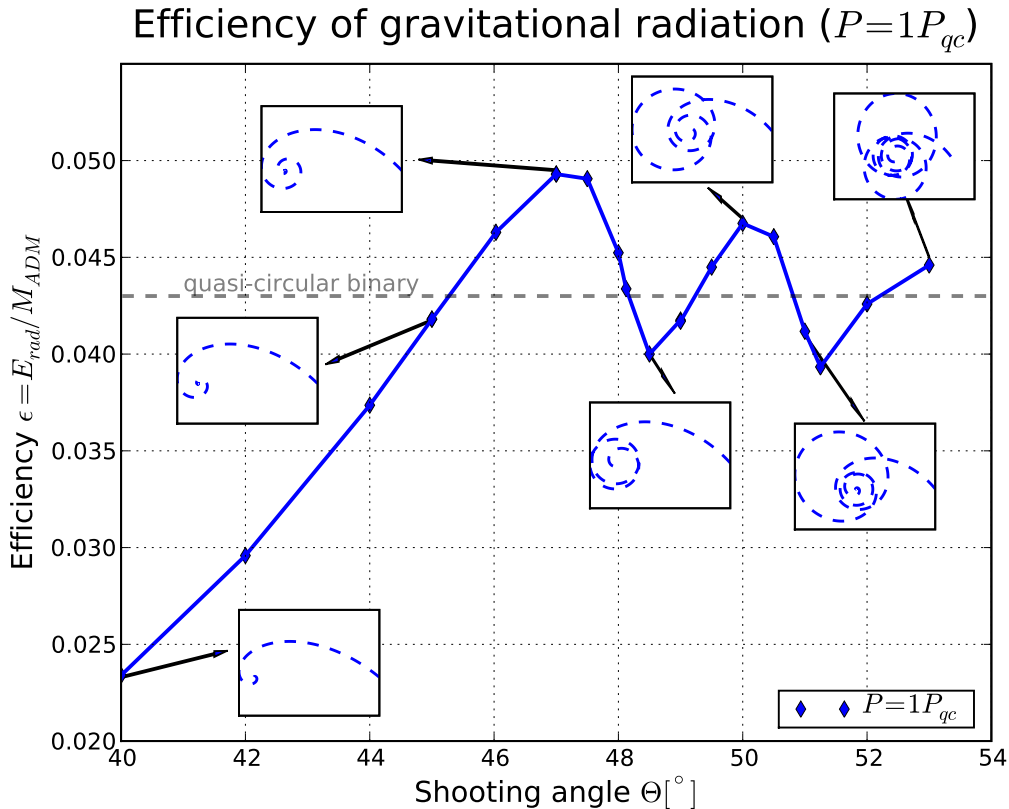
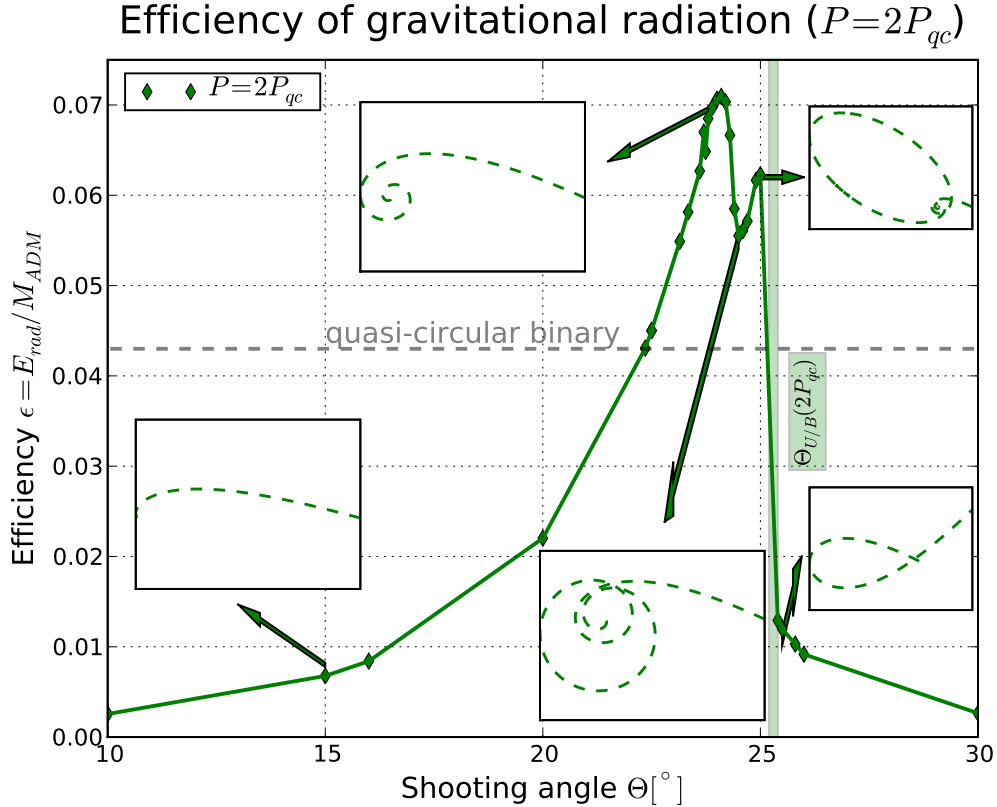


Figure 4.11: Radiated energy for different  $P, \Theta$ . The  $\Theta = 60^\circ$  case is excluded because of visual considerations. The energy radiated of for  $\Theta = 60^\circ$  agrees within the plotting accuracy with the grey line for a quasi-circular binary.

exceptional (see e.g. Fig. 4.3), i.e., instead of small encounter bursts they exhibit a longer signal because of a complicated interplay of the whirl and onset of merger. This waveform feature is most probably not easy to fit inside a hybrid waveform template bank, as also discussed in [122]. To each close encounter burst one can fit the waveforms computed by Turner [94] with an amplifying factor or compare to a PN calculation [158, 159].

Further information on eccentricity can be obtained from the shape of the amplitude (as a function of time). Our finding is, that high eccentricity (though not as high as in the head-on case) is correlated with a strong ring-down signal. The part of the waveform that corresponds to the onset of merger is very sensitive to the velocity of the black holes.

The merger part of the 22-mode is rather similar to the quasi-circular case, but

Figure 4.12: Radiated energy for different  $P, \Theta$ .

a closer look [146] reveals significant differences especially in the amplitudes. At the end of the inspiral phase, the quasi-circular waveform exhibits or more constant contribution early on as opposed to an eccentric signal, with either very quiet or very loud phases before the onset of merger. The latter occurs when the transition to plunge happens through a whirl.

So far the qualitative features described here are rather independent of the mass ratio (up to 1:4). In more quantitative terms, the above analysis is not as straightforward in the unequal-mass regime, but generally it is possible to observe correlations and draw conclusions on the parameters. Especially features like the amount of precession allow to deduce knowledge on the mass ratio from the waveform. We have investigated the waveform and the orbital trajectories for the mass ratio 1 : 3. We find that the whirl effect at the onset of merger can have a more complex structure than equal mass evolutions. This suggests that features induced by eccentric unequal-mass black-hole binary give rise to waveform features which effectively break degeneracies in parameter space [151].

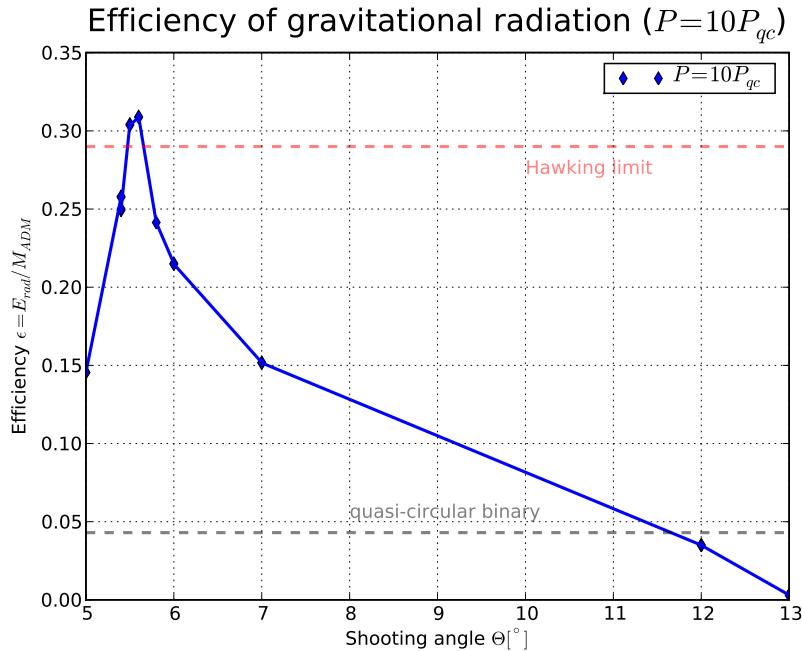


Figure 4.13: Radiated energy for  $10P_{qc}$  and different  $\Theta$ . In these runs we were forced to choose a larger initial separation  $D = 100M$  due to the larger junk radiation in the initial data.

In this work we do not aim for waveform templates. We rather show that with current codes this can be done at a comparatively low computational cost. In order to optimize the matching one also needs to address the question of how initial data should best be parameterized. The latter aim is of course also tightly connected to the canonical parameterization used in PN and EOB approaches [160, 161, 162].

Moreover a comprehensive understanding of the parameter space is essential. A larger parameter study including more mass ratios is needed to derive stronger, more robust correlations. For this and other reasons we demonstrate a larger class of evolutions covering every essential region in the parameter space of non-spinning black-hole binary with comparable masses.

It would be highly desirable to construct accurate template waveforms from such data sets by matching them to waveforms as computed from a PN expansion (see the first comparison [159]). For highly eccentric orbits this matching is more expensive because longer evolutions are needed.

Additional work is necessary to check how efficiently one could model the eccentricity dependence of the waveform empirically also in the highly eccentric regime in order to improve the efficiency in matched-filtering searches. We emphasize that the

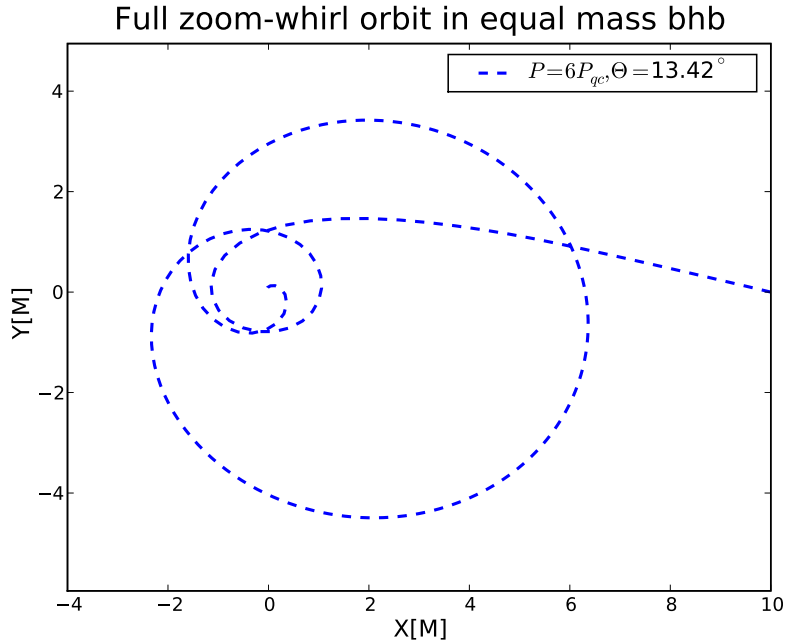
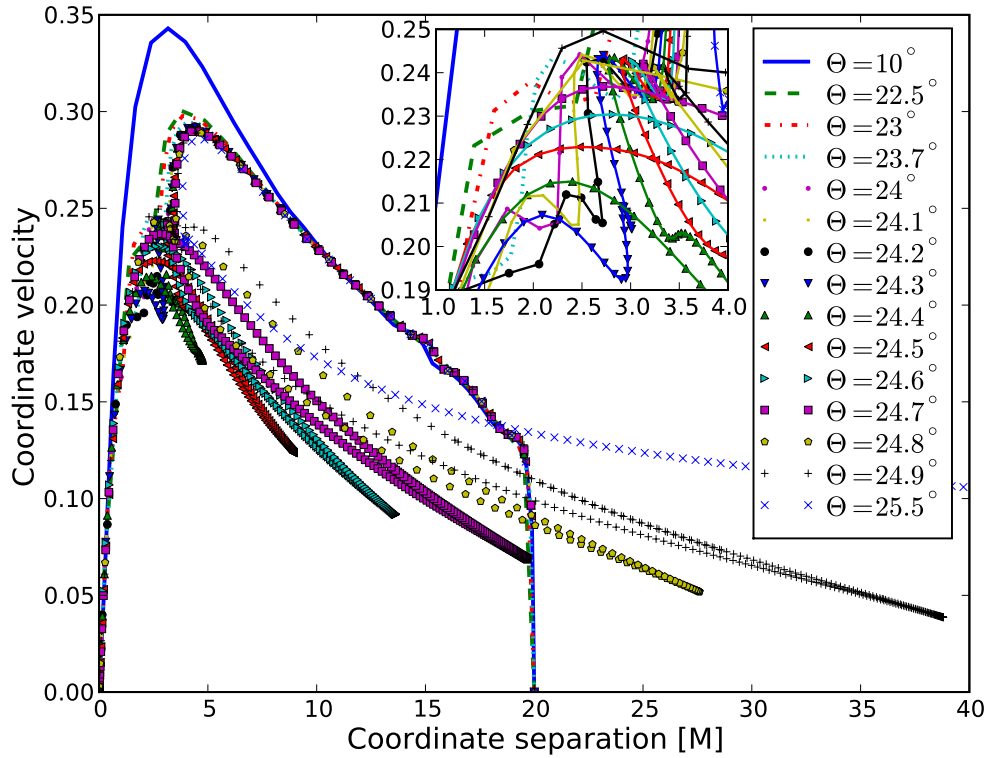


Figure 4.14:  $P = 6P_{qc}$ ,  $\Theta = 13.33^\circ$ . A full zoom-whirl orbit with a more pronounced zoom than in the one in Fig. 4.5.

effects of non-negligible eccentricity on the quality of currently used empirical fits in the data analysis can be undesirable even for ground-based detectors [163, 28]. Since eccentric, equal-mass black-hole binaries can have very strong GW emission and might occur more frequently than expected (e.g. in globular cluster or near galactic centers) there is hope that even ground-based detectors may detect them. Note that especially the bursts associated with capturing phenomena at larger momentum, which may occur in a milder form in globular clusters, are much stronger signals than the ones during merger, see Figs. 4.5 and 4.6. For this reason they might be detectable even by ground-based detectors. Consequently templates for such signals are mandatory to optimize signal processing.

For LISA-like missions the above considerations together with our results (especially from unequal mass ratios) demonstrate that there is much information in the waveforms of eccentric black-hole binaries. Numerical relativity was shown to be capable of improving the accuracy in parameter estimation significantly by providing accurate waveform templates [155]. A similar if not larger improvement will be achieved when including eccentricity [151].


 Figure 4.15: Phasespace for  $P = 2P_{qc}$ .

### Radiated energy

Computing the energy  $E_{rad}$  radiated away in GW

$$E_{rad}(t) = \int_{-\infty}^t \left[ \lim_{r \rightarrow \infty} \frac{r^2}{16\pi} \int_{\Omega} \left| \int_{-\infty}^{\tilde{t}} \Psi_4(\tilde{t}) d\tilde{t} \right|^2 d\Omega \right] d\tilde{t} \quad (4.9)$$

from bound binary system, i.e., **B**-type orbits, not only requires to extract GW in a gauge-invariant way, but also to estimate the cumulated energy radiated during the entire past evolution. In the quasi-circular case there is comparatively little radiation before a typical numerical evolution is started. Hence, the numerically computed energy is rather close to the total amount including the entire past evolution. In the eccentric setups in this study, the evolution in the past of the orbit did cause more significant radiation. We estimate the radiated energy of the past evolution to be  $E_{rad}^{past} \approx -E_{bind}(t = 0)$ . Using this estimate we implicitly assume that the binary was isolated in its entire past. In this case the total energy is zero when



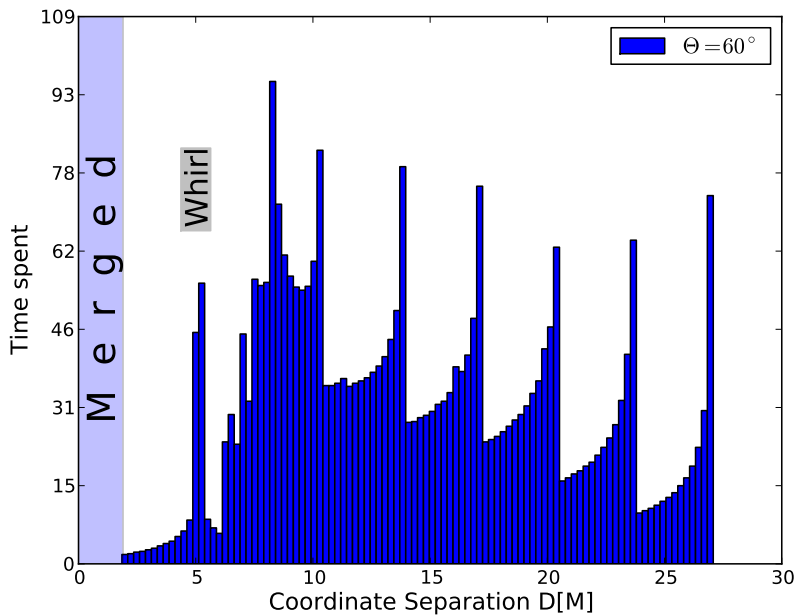


Figure 4.16: Histogram of coordinate separation for the  $P = 1P_{qc}$ ,  $60^\circ$  case. Note the whirl phase at  $D = 5M$  and compare to [122], Fig. 4.18 and Fig. 4.17

the binary is infinitely far separated. In order to approach up to a distance  $D$  the binary has released exactly  $E_{rad}^{past} = E_{bind}$ . Therefore adding the initial negative binding energy to the computed radiated energy one has an estimate for the total amount. The actual value  $E_{bind}(t = 0)$  for the  $P = P_{qc}$  sequence turns out to be  $E_{rad}^{past} \approx -E_{bind}(t = 0) \approx 0.0057 \pm 0.0001$ .

Having performed this estimate for the past evolution we furthermore normalize  $E_{rad}$  by the ADM-mass of the initial time slice  $M_{ADM}(t = 0)$ . The resulting quantity is what we call the “efficiency” of gravitational radiation. It measures the fraction of the total initial ADM-mass of a binary spacetime that is converted in outgoing gravitational radiation. Here we give the maximum efficiency for 7 initial momenta  $P$ . So far the largest value  $35 \pm 5\%$  was reported in [141, 164, 143, 134] (in which the punctures have coordinate velocities of  $v = 0.94$ ). In our data set we approach this limit rather closely (see Fig. 4.13). it was not our aim not to push this limit further, as the junk radiation (which is part of the solution) accounts for  $E_{junk} \approx 0.05$ , but rather extend our data set over roughly the region probed by all groups.

On the other hand if the binary was not isolated through its entire past one obviously has to study how the binary is actually formed. In this case one should

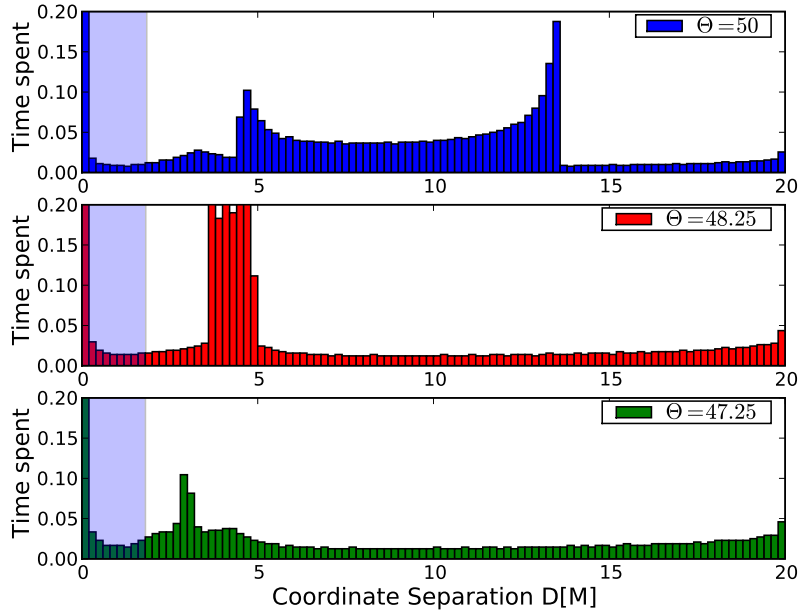


Figure 4.17: Normalized histogram of coordinate separation for three cases in the  $P = 1P_{qc}$  set. The scale on the y-axis should not be directly compared to Fig. 4.16 and Fig. 4.18, because here we normalize and we have not excluded the data after the merger has occurred. Compare the separations where whirls occur with Fig. 4.16 and Fig. 4.18. One can see a tightening of the whirl as initial angular momentum is increased.

analyze the first close encounter phase which eventually leads to a capture. These scenarios are one of our motivations for all runs with  $P > \tilde{P}$ . We emphasize that especially the fly-by orbits can be very violent GW sources when the black holes move very fast and at the same time come very close to each other. These high-velocity fly-by scenarios are - if at all - only relevant from an astrophysical point of view in dense environments like for example globular clusters and galactic cores.

The results of all our evolutions are presented in figs. 4.12 4.13 4.10 4.11. The different lines (colors, symbols) in these plots correspond to different initial momenta and each line shows the efficiency of gravitational radiation as a function of  $\Theta$  (equivalently: Impact parameter, angular momentum or inverse eccentricity).

The first global feature to notice is that gravitational radiation becomes much more efficient for higher momenta.

For low momenta and mass ratios under consideration the shooting angles for

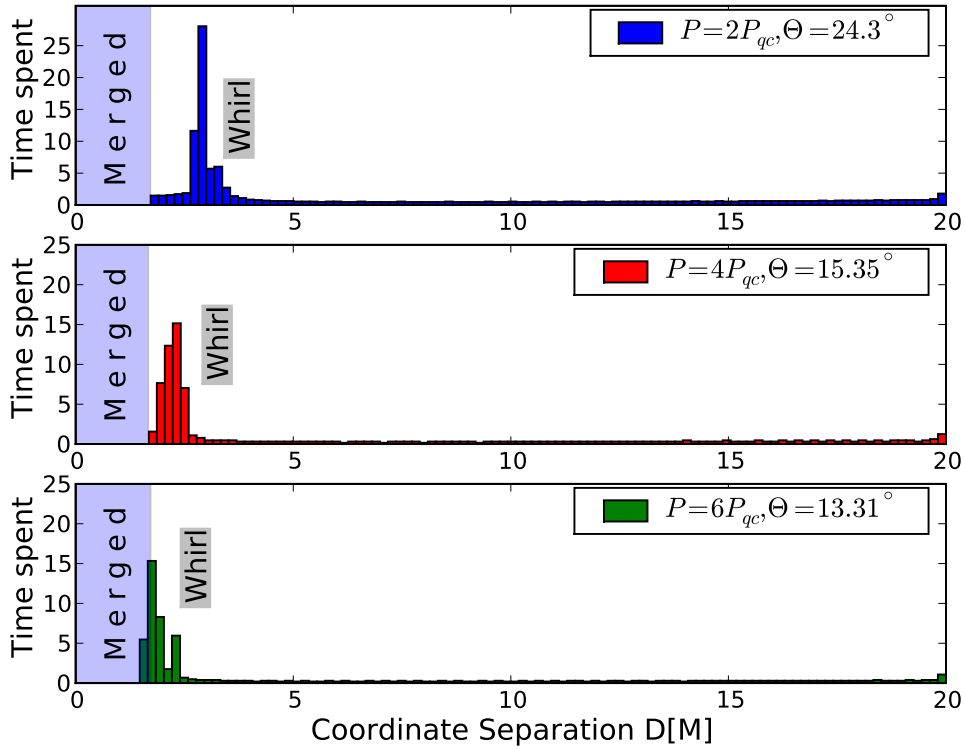


Figure 4.18: Histogram of coordinate separation for higher  $P$  cases. Note, that the binary with  $6P_{qc}$  spend a finite time at a separation smaller than the separation at the later merger. It is to be expected that this a gauge effect.

most number of orbits in general neither coincide with the maxima in  $E_{rad}$  nor do they coincide with the unstable, circular (whirl-like) orbits merging right thereafter. Generally, the maximum in  $E_{rad}$  inside the **U/B**-category lies close to the merger/fly-by threshold. There appears to be a growing amount of degeneracy in the limit  $P \rightarrow \infty$ : Here the unstable circular orbits actually seem to coincide with the most efficient radiators. Concerning the degeneracy, this is indeed expected, from a geodesic analog. Soon after the merger the spacetime will settle down to a Kerr solution with spin parameter depending on the initial data. For low momenta [147, 136] showed that the final spin parameter lies within  $0.6 < a < 0.0832$  with the tendency that the spin parameter grows with the initial momentum. Thus the resulting background spacetime will have tighter characteristic radii ( $r_{isco}, r_{mb}, r_{whirl}$ ). As the binary spends considerably more time at the whirl radius than elsewhere

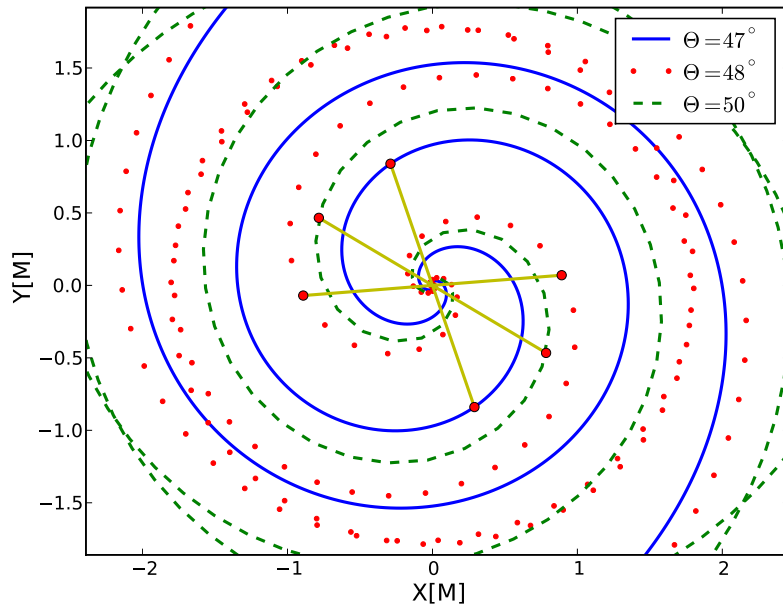


Figure 4.19: We make the following observation for the most efficient radiators at a fixed momentum scale  $P$ : At the moment of merger the tangent to the puncture track is closest to being orthogonal to  $\vec{D}$ .

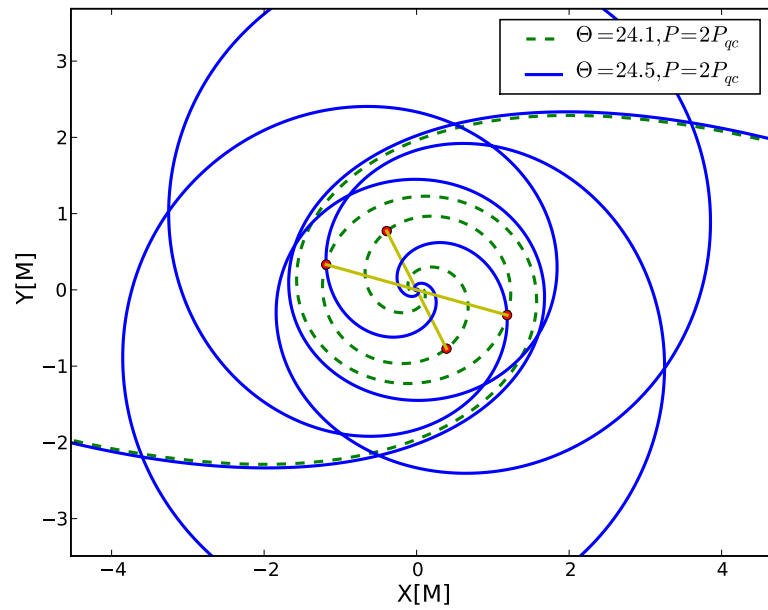


Figure 4.20: The same illustration as in the previous figure but for  $P = 2P_{qc}$ .

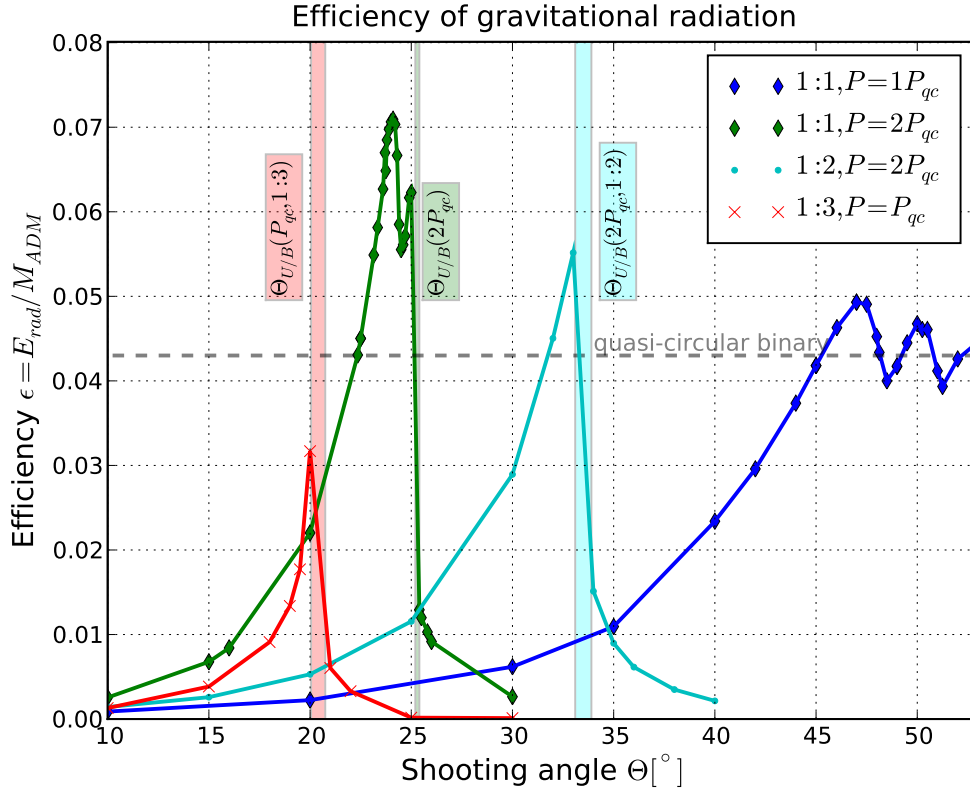


Figure 4.21: Comparison of radiated energy at different mass ratios (1 : 1, 1 : 2, 1 : 3).

(except at a potential apocenter) (see Fig. 4.18) the binary radiates much more efficiently if this whirl occurs at a smaller radius. Thus the tightening of the characteristic radii of the underlying spacetime as the momentum (hence the final spin parameter) is increased can be seen as one reason why in the high momentum case zoom-whirl orbits do coincide with the most efficient radiators, while this is not the case in the low momentum regime, where the whirl radii are significantly larger.

We can confirm previous studies [165] according to which there is a critical maximal eccentricity (minimal  $\Theta$ ) beyond which the radiated energy quickly drops by orders of magnitude to the tiny amounts known from head-on collisions [166]. The drop in  $E_{rad}$  as  $\Theta$  is lowered can clearly be seen for every considered initial momentum in Fig. 4.10. Note, that for the first time one can see that the shape of this transition is by no means trivial (notice the extrema in  $P = 1P_{qc}$  and  $P = 2P_{qc}$ ). Especially in the  $P = 1P_{qc}$  sequence several additional local extrema appear which show a remarkably clean periodicity as a function of  $\Theta$  and should be compared with

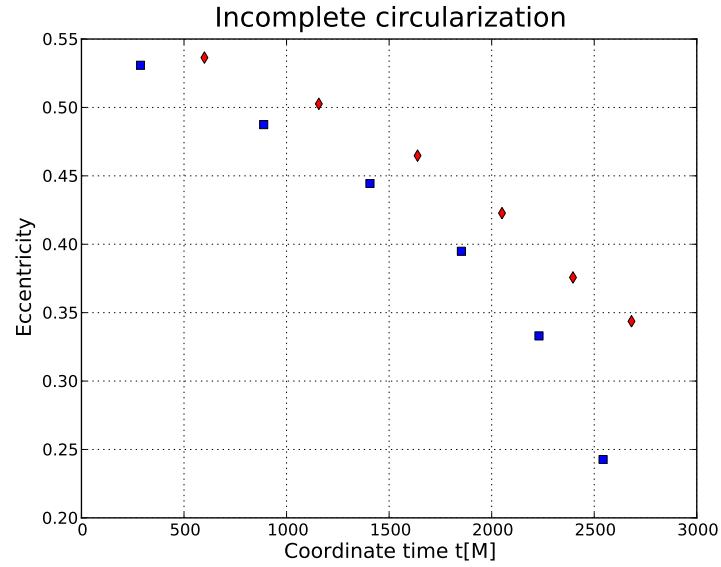


Figure 4.22: Eccentricity evolution in the  $P = 1P_{qc}$ ,  $\Theta = 60^\circ$  case. The eccentricity is estimated as  $e = (a - b)/(a + b)$ , where the upper and lower curve corresponds to two different combinations of  $a$  and  $b$  (1st pericenter, 1st apocenter or 1st apocenter 2nd pericenter, respectively). The values on the time axis are the arithmetic mean between the apocenter and pericenter times.

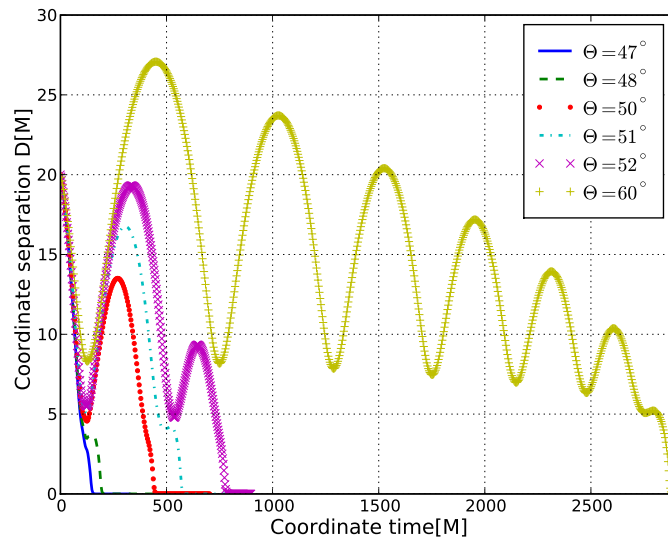


Figure 4.23: Coordinate separation as a function of time. At a given  $P$  none of these curves seems to overlap with another one.

corresponding features in the final spin and mass, seen in [147]. The corresponding features in  $P = 2P_{qc}$  originate from orbits that zoom out again after the first close encounter during which a short, first burst in GW occurs.

There are two qualitative questions to answer:

- (1) Why are there no additional extrema for  $P \geq 3P_{qc}$ ?
- (2) Why is there only one additional maximum in  $P = 2P_{qc}$ ?

The answer to the first question is that the additional fluctuations arise due to GW from after the first close encounter. For large  $P$  the contribution to the  $E_{rad}$  at late times is however completely overwhelmed by the strong first encounter burst leading to a capture. That is to say, the additional second bump is still there, but simply suppressed by the radiated energy during capture.

The second question is less obvious to answer. It is very important to recall that the whirl radii in  $P = 2P_{qc}$  are much tighter than in  $P = 1P_{qc}$  [146] and that the tighter the whirl the more energy and angular momentum is radiated. We interpret the absence of more than one additional maximum for  $P = 2P_{qc}$  as being due to the fact that those orbits which shed sufficient energy to be captured also must radiate too much angular momentum in order to enable an additional whirl episode (in contrast to  $P = 1P_{qc}$ ). One might argue instead, that we did not vary the parameters with sufficient sensitivity in the higher momentum runs (for high momenta small difference in  $\Theta$  lead to larger differences). The large number of evolutions (smooth sampling), exhaustive analysis we have performed and the fact that other investigations have not found such evolutions either render a selection bias rather implausible.

Based on these considerations we conjecture that for equal masses above a certain momentum **only one** phase of close encounter (eventually plus a later merger) is possible simply because of the angular momentum loss during the first close encounter (which is strongly velocity-dependent) as argued above. For lower momenta enough angular momentum can survive and consequently multiple whirl phases can occur, but they are necessarily shorter.

According to our findings from unequal-mass runs the scaling of radiated energy with mass ratio is eccentricity-dependent. By that we mean that the empirically found  $1/\nu^2$  scaling in quasi-circular binaries clearly does not hold and is not generic for all values of  $\Theta$  (see Fig. 4.21). Comparing the maxima in  $E_{rad}$  between equal mass and unequal-mass runs we find that a mass ratio 1:2 still gives a maximal efficiency which is not too far away from the corresponding equal mass run with

the same  $P/M_{ADM}$ . This result is in contradiction to our expectation from quasi-circular binaries where  $E_{rad}$  decreases steeply with mass ratio. Also our results for mass ratios 1:3 and 1:4 show a similar trend suggesting that a mass ratio of 1:4 still is in that sense far away from the geodesic limit. Our results suggest further parameter studies to analyze the scaling in the eccentric regime along the mass ratio axis. Clearly,  $E_{rad}$  is much more sensitive to  $P$  rather than  $\nu$ .

We finish this section with a comparison of the lowest momentum results considered ( $P = 1P_{qc}$ ) with the Hawking limit [167] for the maximal radiated energy derived from the area theorem. The spacetimes in this sequence are the closest realization of two Schwarzschild black holes with vanishing orbital angular momentum at infinity within our data set. Note that our value is also the maximum of **all** non-spinning black-hole binaries with momenta  $P \lesssim 1P_{qc}$ , as yet slower  $P$  according to our results further reduce efficiency and unequal-mass black-hole binary have systemically less dynamic quadrupole moment than equal-mass black-hole binary. We deduce a maximum efficiency of a merger of two non-spinning black holes (with arbitrary mass ratio) to be  $5 \pm 0.05\%$  which is far away from the limit  $29\%$  that follows from Hawking's area theorem. Only for some runs in the  $P = 10P_{qc}$  sequence we reach higher efficiencies (see Fig. 4.13) when the local spacetime around each black hole should be significantly different from a Schwarzschild spacetime because of the additional momentum. However, computing the Lorentz-factor  $W$  from the coordinate velocity we note that the motion of the punctures is still rather mildly relativistic at the onset of merger. This finding turns out to be surprisingly insensitive to the initial momentum. Increasing the initial momentum of the punctures leads to a motion which is rather relativistic when entering the whirl phase ( $W \approx 1.155$ ), but during the whirl they decelerate by large amounts (for  $P = 6P_{qc}$  the decrease in velocity is as large as during the merger). At merger however **all** equal mass evolutions approach  $W \approx 1.05 \pm 0.02$  independent of their initial data.

### 4.6.3 Phase space

Many interesting questions about black-hole binaries are difficult to answer by only investigating gauge-invariant quantities. New diagnostics are useful to interpret these spacetimes. A very useful construction which we are going to use is the histogram of  $D(t)$  (see also Figs. 4.16 4.17 and 4.18). Since the histogram simply counts the number of timesteps per interval  $D \pm \Delta D$  one can multiply by the timestep to measure the coordinate time the binary spends within the coordinate separation



interval. We would like to focus on two important conclusions drawn from this plot. First, as already reported in [146] the whirls as viewed as the analogon to unstable circular orbits in background spacetimes show up as a sharp and well-defined peak allowing us to measure the radii of unstable circular orbits in these highly non-linear spacetimes remarkably well. Second, the whirl radii are becoming systematically tighter as  $P$  increases (see Fig. 4.18) which is related to a higher Kerr-parameter of the merger remnant once it has concluded the ring-down phase [165, 147].

A second diagnostic we use is the trajectory through phase space, see fig 4.15. It is built from  $D(t)$  and the coordinate velocity  $v(t)$  of the punctures (serving as generalized coordinates). The introduction of these two diagnostics serves the purpose of probing two key aspects of the dynamics of a binary for emission of gravitational radiation:

- The faster the black holes move the more the binary radiates (maximizing the third time-derivative of the mass-quadrupole).
- The longer a binary spends in a configuration allowing fast motion, the more it radiates (maximizing the integral over time).

Both of those principles arise from an intuition relying on the quadrupole formula. The first principle is based on the fact that fast and tightly moving binaries maximize the third time-derivative of the mass quadrupole moment, see equation 4.1. The second principle takes into account the fact that  $E_{rad}$  is an integral of  $\Psi_4$  over time (see equation 4.9). In this section we demonstrate that indeed these two diagnostics allow one to understand why some evolutions radiate more than others and that in combination they constitute a very instructive way of analyzing black-hole binary spacetimes. The complete set of phase space trajectories can be viewed as a vector field on the phase space, see Fig. 4.15, characterizing the dynamics of a binary with general initial conditions within a single plot. Obviously, this construction is strongly gauge-dependent, since it is built from three coordinates. Switching to another gauge should lead to some sort of deformation of the trajectory. In fact, we see non-trivial gauge effects in some high momentum evolutions where outmoving punctures near the merger-/flyby threshold accelerate.

However, several former investigations have led to the conclusion that the coordinates of punctures correspond rather well to what an observer at infinity sees [168, 169]. Apart from that there are other reasons suggesting that these coordinate quantities contain relevant, physical information. The time interval between two

apocenters  $D_{ap}$  or pericenters  $D_{per}$  is gauge-invariant despite the fact that  $t$  and the numerical **values** of  $D_{ap}$  or  $D_{per}$  are, of course, gauge-dependent. Summarizing, being aware of the gauge issue, we use this construction to analyze our evolutions. We probe the gauge-dependence by varying  $P$  by factors as large as 10 to justify our conclusions.

To familiarize us with the trajectories in phase space consider a circular motion. This motion corresponds to a single point, and a closed ellipse to a straight line.

We now describe trajectories found in the  $P = 2P_{qc}$  set as shown in Fig. 4.15. The evolution starts at the lower right corner ( $D = 20M, v = 0$ ). The trajectory quickly rises (due to gauge adjustment) so that the momentum of each black hole approaches the value given in the initial data. Then very intuitively the trajectory moves towards the upper left (orbits shrink, punctures become faster). Note that for large separations and low velocities the trajectory is approximates Kepler’s law. But as soon as gravity pulls non-perturbatively the trajectories depart from the Newtonian behavior. The monotonic lines from the Newtonian theory are replaced (wound up) and are finally dragged towards the origin ( $D = 0, \mathbf{v} = 0$ ) which is an inevitable attractor for all bound systems.

The other orbits that form the opposite extreme class are the fly-by evolutions (see  $\Theta \geq 25.5^\circ$  data in Fig. 4.15). While they all start out near the same point in phase space, they have a turning point before merger would set in and escape to the right (towards spatial infinity), instead of plunging. A head-on collision in phase space looks very much like an eccentric binary starting on the  $\mathbf{v} = 0$  line at the value of  $D$  that corresponds to the same total energy. We note that a head-on collision always constitutes an upper envelope in the phase space (see Fig. 4.15). That is to say, fixing  $P$  and comparing  $\Theta = 0$  runs with  $\Theta \neq 0$  evolutions we always find  $\mathbf{v}(t, \Theta = 0) > \mathbf{v}(t, \Theta \neq 0)$  (at least for  $D(t) \leq D(t = 0)$ ). A remaining question is whether the lower envelope also corresponds to a physical solution. The most straightforward expectation one has is a quasi-circular inspiral starting from a coordinate separation, which leads to the same total energy. However we were not able to do a direct comparison simply because a quasi-circular binary with initially  $D = 20M$  is just computationally not affordable at the moment as it initially moves extremely slowly through phase space.

One might ask whether the minima and maxima in efficiency as a function of  $\Theta$  appear due to a certain “type of merger” or in other words “near-merger-dynamics”. Indeed there are systematic features: Efficiency is maximized when at the time at

which a common horizon is formed, the tangent vector to the puncture trajectory exhibits the largest angle with the separation vector  $\vec{D}$  (see [146], Figs. 4.19 and 4.20). We interpret this empirical finding in the following way: Maximizing the above mentioned angle translates into maximizing the quantity  $\vec{L} = \vec{D} \times \vec{P}$ , i.e., the flat-space expression for the angular momentum of two point masses with momentum  $P$  separated by a distance  $D$ . We therefore conjecture based on our data set that the strongest ring-down signals are caused by those evolutions which maximize the angular momentum at the moment of merger. Independent of this interpretation it is evident that this orbital feature coincides with the fluctuations in  $E_{rad}$ . Our data set in  $P = P_{qc}$  is consistent with the interpretation that the maxima and minima in  $E_{rad}$  occur because of distinct ringdown signals (as interpreted above). This is evident just by comparing the GWs. We are, however, unable to give an explanation for the differences between the individual maxima solely based on gauge-invariant quantities. Using the phase space trajectories one can see that the differences coincide with differences in the durations the black-hole binary spends in the radiatively most efficient phases as can be seen in the phase space (not shown) and in histograms of  $D$  Fig. 4.17.

Comparing the different zoom episodes at progressively shrinking  $D_{per}$  the phase-space trajectory reveals the non-perturbative nature of a black-hole binary spacetime close to merger: The further the trajectory approaches the lower left the more these lines are bent in sharp contrast to the rather straight lines at large  $D$  expected for orbits closer to Kepler's ellipses.

Comparing these findings to a similar analysis of the **U/B**-category allows to study the  $P$ -dependence of radiation properties, hence to probe the robustness of our gauge-dependent conclusions in [146]. Furthermore using the phase space trajectories one can have a more comprehensive and compact view on the structure of the merger/ fly-by transition region.

The transition zone between bound and unbound evolutions is illustrated using the phase-space trajectories (see in Fig. 4.15) for the  $P = 2P_{qc}$  sequence varying  $\Theta$ . First, we recognize the two extreme cases we have already discussed above. Inbetween, we find a very complex transition which is governed by several additional (non closed) loops corresponding to orbits that zoom out after a first whirl phase thereby slowing down, i.e., moving to the lower right, before returning towards the upper left. Note that during the next zoom-in the binary must follow a path further to the lower left, because the system is dissipative.

The turning points correspond to the apocenter which become sharper as the binary tightens. The set of these turning points form a lower envelope (in analogy to the upper envelope mentioned before) that is never crossed by any of our evolutions at the same initial  $D$ . Interestingly, the set of all  $\Theta$  evolutions (at fixed  $P \geq \tilde{P}$ ) look very similar to a  $P \leq \tilde{P}$  low  $\Theta$  (e.g.  $P = 1P_{qc}, \Theta = 60^\circ$ ) evolution.

Note how far the zooms may extend when the binary approaches the merger/fly-by threshold resulting in an ever larger runtime. We face difficulties in the bound orbits near  $\Theta \rightarrow \Theta_{fly-by}^{merger}$  because those orbits both need very long evolutions (decrease of accuracy) and most importantly the black holes may be separated so far that they move near or even through the wave extraction sphere thereby producing artificial features in  $E_{rad}$ . This contaminates the waves and a clean separation of physical radiation and gauge dynamics is not trivial. It is not simple to subtract this contamination even when it was safely separated from the real signal in time because the computation of  $E_{rad}$  is unphysically influenced ever since the punctures have moved through the extraction sphere (as if spacetime locally remembered a puncture moving by before). These issues typically do not arise for low eccentric evolutions even when the wave-extraction sphere is very close (say  $40M$ ).

**Unequal masses:** An investigation of the phase-space trajectories of unequal-mass black-hole binaries reveals that the general shape of the trajectories is quite robust with respect to the mass ratio. There are two main differences: (1) Unequal-mass orbits move systematically slower compared to a corresponding equal mass binary with comparable initial momentum. (2) Unequal-mass mergers start their final plunge from an increasingly larger coordinate separation than equal mass mergers. These are the most important reasons why radiation in the unequal-mass evolutions is weaker. Yet another possible reason could be that also the deceleration is milder for higher mass ratios. In other words, unequal-mass binaries do not tap as deeply into the gravitational potential as equal mass binaries, thus cannot extract as much energy from the spacetime. As mentioned already in 4.6.2, we find evidence that there is a strong eccentricity-dependence in how  $E_{rad}$  scales with mass ratio.

We have analyzed the phase-space trajectories for mass ratios  $1 : 1, 1 : 2$  and  $1 : 4$ . The systemically lower velocities for larger mass ratios in comparison to equal-mass black-hole binary is evident. We emphasize that further study is required to sample the behavior of eccentric unequal-mass binaries. In particular, studies of larger mass ratios would give more insights into the geodesic analogon.

# 5 Binary neutron stars on eccentric orbits

The results shown previously were vacuum solutions to Einstein's field equation  $R_{\mu\nu} = 0$ . In this chapter we will extend previous results to a case with non-vanishing stress-energy tensor, namely binary neutron stars on eccentric orbits. One way to read the field equation with non-zero  $T_{\mu\nu}$  is to imagine that matter produces spacetime curvature which itself is the source of gravity. Conversely, the spacetime dictates the matter how to move. This coupling between the metric and the matter corresponds to a non-linearity of the field equation which gives rise to new subtleties. In the next section we outline how the additional terms on the right hand side, i.e.,  $T_{\mu\nu} \neq 0$  are computed.

## 5.1 The matter scheme

In [170] a scheme for hydrodynamics has been added to the BAM code. Here we summarize the fundamental equations. For details on the numerical implementation we refer to [170].

Assume a stress-energy tensor of a perfect fluid:

$$T_{\mu\nu} = \rho h u_\mu u_\nu + p g_{\mu\nu} , \quad (5.1)$$

with  $\rho$  the rest-mass density,  $\epsilon$  the specific internal energy,  $h \equiv 1 + \epsilon + p/\rho$  the specific enthalpy,  $p$  the pressure and  $u^\mu$  the four-velocity ( $u^\mu u_\mu = -1$ ). The total energy density is given by

$$e = \rho(1 + \epsilon) . \quad (5.2)$$

The equations for matter are given by the local conservation laws for the energy-

momentum tensor and baryon number,

$$\nabla_a T^{ab} = 0 \quad (5.3)$$

$$\nabla_a (\rho u^a) = 0 \quad (5.4)$$

respectively, and an equation of state, which we discuss later. The *conservative* variables are defined as:

$$\vec{q} \equiv \sqrt{\gamma} [D, S_i, \tau] , \quad (5.5)$$

and can be obtained from the 6 *primitive* variables  $\vec{w} = \{p, \rho, v^i, \epsilon\}$  via the relations:

$$D \equiv W \rho \quad (5.6a)$$

$$S_i \equiv W^2 \rho h v_i \quad (5.6b)$$

$$\tau \equiv (W^2 \rho h - p) - D . \quad (5.6c)$$

Above  $v^i$  is the fluid velocity measured by the Eulerian observer:

$$v^i = \frac{u^i}{W} + \frac{\beta^i}{\alpha} = \frac{1}{\alpha} \left( \frac{u^i}{u^0} + \beta^i \right) , \quad (5.7)$$

and  $W$  is the Lorentz factor between the fluid frame and the Eulerian observer,  $W = 1/\sqrt{1-v^2}$ , with  $v^2 = \gamma_{ij} v^i v^j$ .

The hyperbolic, first-order and flux-conservative form is [171, 172, 173]:

$$\partial_t \vec{q} + \partial_i \vec{f}^{(i)}(\vec{q}) = \vec{s}(\vec{q}) , \quad (5.8)$$

where  $\vec{f}^{(i)}(\vec{q})$  are the fluxes:

$$\vec{f}^{(i)} \equiv \sqrt{-g} \left[ D \left( v^i - \frac{\beta^i}{\alpha} \right), S_j \left( v^i - \frac{\beta^i}{\alpha} \right) + p \delta_j^i, \tau \left( v^i - \frac{\beta^i}{\alpha} \right) + p v^i \right] \quad (5.9)$$

and  $\vec{s}(\vec{q})$  are the source terms:

$$\vec{s} \equiv \sqrt{-g} \left[ 0, T^{\mu\nu} (\partial_\mu g_{\nu j} - \Gamma_{\nu\mu}^\delta g_{\delta j}), \alpha (T^{\mu 0} \partial_\mu \ln \alpha - T^{\mu\nu} \Gamma_{\nu\mu}^0) \right] . \quad (5.10)$$

Above  $g \equiv \det g_{\mu\nu} = -\alpha^2 \gamma$  and  $\gamma \equiv \det \gamma_{ij}$ .

The system in Eq. (5.8) is strongly hyperbolic in flat spacetime [172].

### 5.1.1 Equation of state

The system is closed by an equation of state of the form:

$$p = P(\rho, \epsilon) . \quad (5.11)$$

The sound speed  $c_s^2$  is defined as:

$$hc_s^2 = \chi + \frac{p}{\rho^2} \kappa \quad (5.12)$$

$$\chi \equiv \frac{\partial P}{\partial \rho} \quad (5.13)$$

$$\kappa \equiv \frac{\partial P}{\partial \epsilon} . \quad (5.14)$$

For this thesis we choose a polytropic equation of state

$$P(\rho) = K\rho^\Gamma \quad ; \quad \epsilon(\rho) = K\frac{\rho^{\Gamma-1}}{\Gamma-1} \quad (5.15)$$

where  $K$  and  $\Gamma$  are parameters which we here set to  $K = 100$  and  $\Gamma = 2$ , respectively.

### 5.1.2 High Resolution Shock Capturing methods

One of the additional challenges of matter spacetimes not present in vacuum spacetimes is the possibility of shock formation. Starting from smooth initial data discontinuities may form in a finite time. These features are part of the physical weak solution and hence have to be approximated by the numerical scheme employed. There is a huge literature behind numerical schemes capable of coping with such discontinuities and they are commonly referred to as *High-Resolution-Shock-Capturing* methods (HRSC), see [174] for a comprehensive introduction and references therein. The strategy to deal with discontinuous data is founded on the Riemann Problem. The Riemann Problem is an initial-value problem of a conservation law of the form 5.8 together with piecewise constant initial data, i.e., one discontinuity in the initial data. For non-linear problems one can approximate the solution locally by a Riemann Problem at each cell interface. For a detailed and comprehensive description see [174].

We solve the equations described above introducing a uniform staggered spatial grid of spacing  $\Delta x$  and  $N_x$  points and considering the semi-discrete form of the

equations:

$$\frac{d\vec{q}_i}{dt} = \frac{1}{\Delta x} \left( \hat{f}_{i-\frac{1}{2}} - \hat{f}_{i+\frac{1}{2}} \right) + \frac{1}{\Delta y} \left( \hat{f}_{j-\frac{1}{2}} - \hat{f}_{j+\frac{1}{2}} \right) + \frac{1}{\Delta z} \left( \hat{f}_{k-\frac{1}{2}} - \hat{f}_{k+\frac{1}{2}} \right) + \vec{s}_i \quad (5.16)$$

where the  $\hat{f}_{i\pm\frac{1}{2}}$  (five component vectors) are the numerical fluxes computed from the physical ones (Eq. (5.9)) by interpolating on the cell interfaces in a non-oscillatory way and solving an approximate Riemann problem. We adopt the method of lines (MoL) to solve Eq. (5.16), based on BAM Runge-Kutta integrators.

The HRSC method adopted for the computation of the RHS of Eq. (5.16) is described in [175, 176] and it is based on point values discretization (instead of cell averages), high-order non-oscillatory reconstructions [177, 178, 179] and central schemes [180, 181]. The method adopts high-order non-oscillatory interpolation of the primitive variable to cell interfaces. See [182] for a discussion on the link with Finite Volume Methods.

The basics steps of the algorithm are:

- Recovery of the primitive variables  $\vec{w}$  from the conservative ones  $\vec{q}$
- Reconstruction of the primitive variables at interfaces  $i + \frac{1}{2}$ : In this thesis I use the (CENO3) scheme because it preserves the Hamiltonian constraint better [170] than other schemes implemented.
- Computation of the numerical fluxes  $\hat{f}_{i+\frac{1}{2}}$ : applying local Lax-Friedrich (LLF) [180, 181] as an approximate Riemann solver which takes into account the eigenvalues of the Jacobian in equation Eq. (5.8) to determine the local characteristic speeds.
- Computation of source terms  $\vec{s}$  from Eq. (5.10):
- Time-(sub)-step .

### 5.1.3 Vacuum treatment

In regions where the density/pressure drops below some critical value the fundamental equations become ill-defined, namely the assumption of a fluid description breaks down. This issue also arises in Newtonian Hydrodynamics for many astrophysical applications. In order to simulate systems that give rise to such evacuated regions one thus has to deal with this problem in some way. A rigorous consistent



treatment is unknown, but several strategies have proven to be better than others. The standard approach is to use an artificial atmosphere specified by a floor value. If the density is lower than the floor value it is simply replaced by the floor value. The floor value is chosen just as large as necessary to achieve stable evolution also in vacuum regions in order to affect the dynamics as little as possible.

## 5.2 Binary neutron stars on eccentric orbits

The possible relevance of tight eccentric encounters has been studied in [183, 184]. Recent population synthesis studies [185] suggest that a significant fraction of eccentric neutron star - neutron star binaries will give rise to GW signals detectable by future detectors such as DECIGO [186] or the Einstein telescope [156]<sup>1</sup>. According to the results for DECIGO, 2 – 27% of binary neutron stars will have  $e > 0.01$  at the time they enter the sensitivity-band. This still suggests that tight, eccentric binary neutron stars are rare, yet they are potential sources for DECIGO<sup>2</sup>.

These systems are natural laboratories to study the effects of the equation of state on tidal disruption and may lead to conclusions also for mixed binary scenarios [187]. So far eccentric neutron-star binaries have not been studied in numerical relativity. One expects enhanced tidal interaction over Newtonian dynamics or quasi-circular evolutions in GR (see [35] and references therein) especially during the close encounters or potential whirl phases. These considerations suggest a rich, yet unexplored phenomenology around the threshold of immediate merger.

### 5.2.1 Initial data

We superpose two individually boosted TOV solutions with each other according to  $g_{\mu\nu} = g_{\mu\nu}^{tov1} + g_{\mu\nu}^{tov2} - \eta_{\mu\nu}$  which preserves the asymptotics ( $r \rightarrow \infty$ ) of the individual solutions. Given the non-linearity of the constraint equations of GR the resulting initial data obviously does *not* satisfy the constraint equations of GR, but we have checked that the constraint violations fall off with  $1/D$  for sufficiently large separations  $D$  as expected. Thus one may view this type of initial data as an ap-

---

<sup>1</sup>However, near future detectors, such as advanced LIGO, are most likely blind to these event. Only 2% of binary neutron stars will have  $e > 0.01$  when entering the advLIGO sensitivity band.

<sup>2</sup>DECIGO is the proposed Japanese space-based GW detector most sensitive at frequencies  $0.1Hz < \nu < 10Hz$ .

proximate solution to the constraint equations expanded in inverse powers of the binary separation.

We now describe the procedure for one boosted TOV. The starting point is the 4D-ADM metric  $g_{\mu\nu}^{SW}$  of isotropic Schwarzschild (SW) which is the unique solution to a static, isotropic spacetime and thus also describes the exterior TOV solution

$$g_{\mu\nu}^{tov,ex} = g_{\mu\nu}^{SW} = \begin{pmatrix} -\alpha^2 & 0 \\ 0 & \psi^4 \delta_{ij} \end{pmatrix} \quad (5.17)$$

$$\alpha_{,i}^{ext} = M/(0.5M + r)^2 x_i/r \quad (5.18)$$

$$(\psi^4)_{,i}^{ext} = -2M\psi^3 x_i/r^3 \quad (5.19)$$

with the conformal factor  $\psi = 1 + M/2r$ . For the inner metric  $g_{\mu\nu}^{tov,in}$  and its derivatives  $d\alpha, d(\psi_4)$  we use the spectral code which solves for a spherically symmetric star configuration, using a Chebyshev expansion (see details in [72]).

We will also need the Christoffel symbols

$$\Gamma_{\mu\nu}^{\kappa} = \frac{g^{s\kappa}}{2} (g_{\mu s, \nu}^{tov} + g_{\nu s, \mu}^{tov} - g_{\mu\nu, s}^{tov}) \quad (5.20)$$

in which the derivatives of the metric are given by

$$g_{\mu\nu, \kappa} = \begin{pmatrix} -2\alpha\alpha_{, \kappa} & 0 \\ 0 & (\psi_4)_{, \kappa} \delta_{ij} \end{pmatrix} \quad (5.21)$$

We proceed by applying a Lorentz-boost to  $g_{\mu\nu}^{tov}, g_{\mu\nu, \sigma}^{tov}$  and  $\Gamma_{\mu\nu}^{\sigma}$  as

$$g_{\mu\nu}^{tov} = \Lambda_{\mu}^{\sigma} \Lambda_{\nu}^{\lambda} g_{\sigma\lambda}^{tov} \quad (5.22)$$

$$g_{\mu\nu, \kappa}^{tov} = \Lambda_{\kappa}^{\tau} \Lambda_{\mu}^{\sigma} \Lambda_{\nu}^{\lambda} \Gamma_{\mu\nu}^{\tau\kappa} = \Lambda_{\tau}^{\kappa} \Lambda_{\mu}^{\sigma} \Lambda_{\nu}^{\lambda} \Gamma_{\sigma\lambda}^{\tau} \quad (5.23)$$

Finally the initial data follows from:

$$\alpha = -\sqrt{\frac{1}{g_{00}^{tov-1}}} \quad (5.24)$$

$$\beta^i = -\frac{g_{tov-1}^{0i}}{g_{tov-1}^{00}} \quad (5.25)$$

$$\gamma_{ij} = g_{ij}^{tov} \quad (5.26)$$

$$K_{ij} = -\alpha \Gamma_{ij}^t \quad (5.27)$$

## 5.2.2 Test cases

As first tests spacetimes of single boosted TOV as well as two TOV stars head-on from rest have been evolved successfully. Here we briefly describe our findings. The boosted TOV test will give an impression of how accurately we can follow the motion of a TOV star on the grid. The head-on case validates our approach of setting up approximate initial data according to the superposition we described. All TOV stars in this work have a mass of  $M = 1.4 M_{\odot}$  and a radius of  $R = 8.126 \text{ km}$ .

### Single boosted TOV

Due to the non-trivial gauge conditions the resulting coordinate velocity may deviate from the prescribed boost-parameter. Extensive testing of the boosted TOV routine leads to the results shown in Fig. 5.1. We track the star by tracking the minimum of  $\alpha$ . The coordinate velocity agrees with the boost parameter to within  $\Delta v/v \approx 1\%$  for a grid with finest resolution  $h = M/8$ .

There is large dynamics initially which is probably due to the behavior of the moving puncture gauge. In Fig. 5.1 we show the coordinate velocity and the Hamiltonian constraint violations as a function time. One can see that initializing the shift according to the analytic solution reduces that gauge dynamics considerably compared to the case where the  $\beta^i = 0$  initially. Therefore we will from now on always use the analytic shift as initial condition.

### Head-on case

The simplest test involving the superposition is the head-on collision of two neutron stars starting from rest. The neutron stars fall towards each other and merge. The merger remnant is at rest with respect to the grid and quickly forms a horizon. We

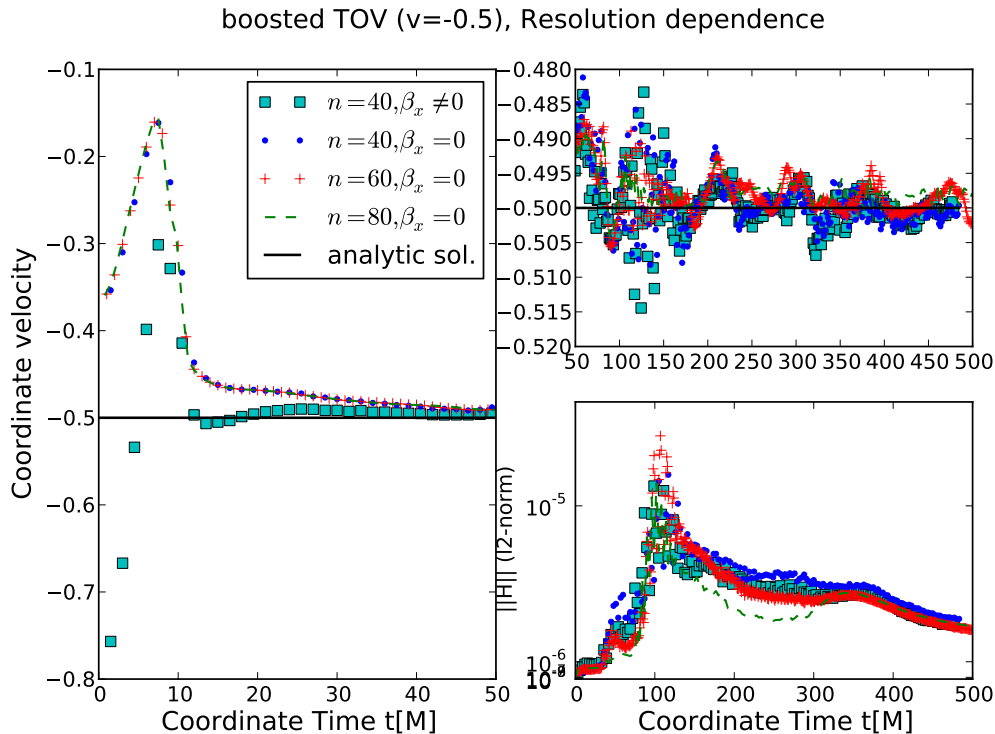


Figure 5.1: Coordinate velocity and L2-norm of the Hamiltonian constraint violations as a function of coordinate time for a boosted TOV solution with boost parameter  $v = -0.5$ . The left plot shows the global picture with an initial gauge adjustment before the velocity settles down to the analytic value. The fluctuations due to the gauge are considerably reduced by specifying the initial shift according to the analytic solution instead of setting it to zero. The upper right subplot is a zoom on the coordinate velocity for  $t > 50$  and shows agreement with the expected velocity of  $\Delta v/v \approx 1\%$ . On the initial slice the Hamiltonian constraint has the lowest value over the entire evolution demonstrating the dominant contribution of the truncation error of the evolution scheme.

have also performed the more general case that involves an initial modest boost and obtain very similar results.

Performing this test at different resolutions and separations  $D = 20, 40M, 50M$  we clearly find the constraint violations due to the finite separation dominate over the discretization error. In the evolution the truncation error soon becomes the dominant contribution.

## 5.3 Binary case: Results

We now turn to the study of binary neutron stars on eccentric orbits. We start by describing our setup and explain the orbital properties that our models seen in Figs. 5.2 and 5.3

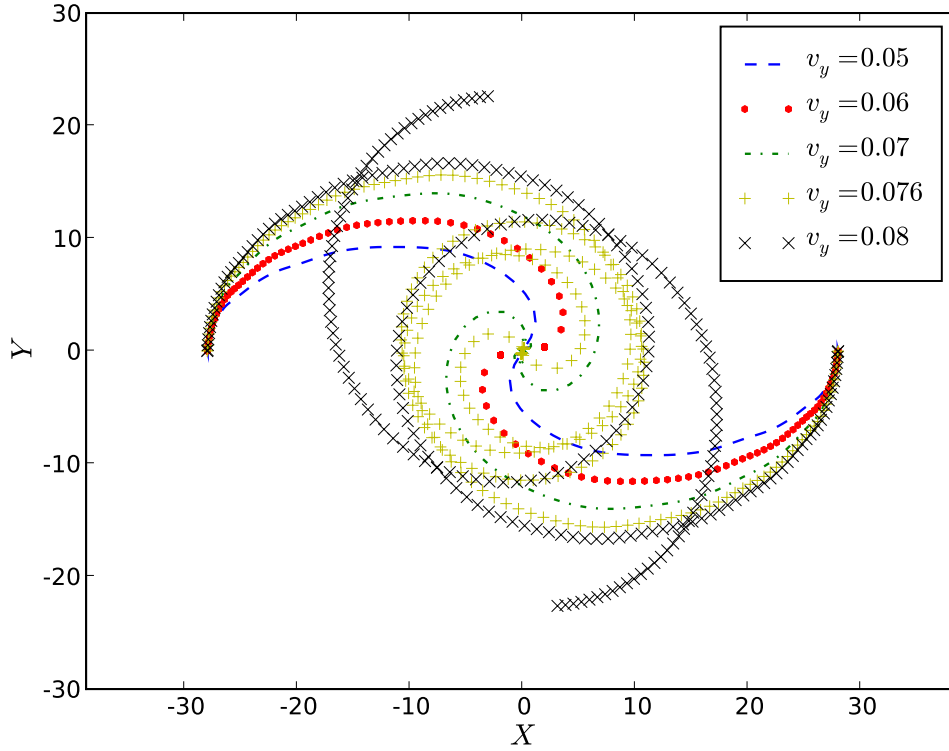


Figure 5.2: Here we show the orbital trajectories of a subset of the  $D = 20M$  data. In the main text the overall dynamics is discussed from low to high  $v_y$ . The  $v_y = 0.08$  case survives the first encounter. We have followed the evolution for longer, but we expect it to merge later on.

### 5.3.1 Setup

We set up neutron-star neutron-star binaries using the superposition strategy, outlined before, placing the stars at  $x_{tov1} = -x_{tov2}$ . By specifying a boost along the y-axis we obtain initial data close to a binary at apocenter such that  $2a(t = 0) \approx D(t = 0) = 2|x_{tov1/2}| = 20M$  (where  $M = m_{tov1} + m_{tov2}$ ).



Figure 5.3: Here we show the orbital trajectories of a subset of the  $D = 50M$  data. In the main text we discussed the  $v_y = 0.02$  case in detail. The initial parts of the orbit have been suppressed for better visual impression.

We thus parameterize our initial data set by a single parameter, namely the initial tangential boost velocity  $v_y$  setting  $v_x = v_z = 0$ . This parameter is of course directly related to the initial shooting angle (as discussed in the black-hole binary case), eccentricity, impact parameter or orbital angular momentum. The models considered here are labeled by the value of the initial tangential velocity  $v_y$  and separation  $D$ . The latter corresponds to the apocenter of the orbit.

### 5.3.2 Global outcome and orbital dynamics

We discuss the orbital dynamics found in the  $D = 20M$  data set from low to high values  $v_y$  guided by the trajectories shown in Fig. 5.2. The phenomenology in the  $D = 50M$  set is the same.

For  $v_y < 0.07$  the neutron stars do not complete a full orbit. Instead they plunge, merge and rapidly form a black hole. Increasing  $v_y$  further the orbits survive for

longer, just as in the black hole binary case. Also the collapse to a black hole occurs later. For the  $v_y = 0.076$  case we see a whirl followed directly by a plunge. The  $v_y = 0.077$  barely survives the first encounter, because the pericenter distance is larger. The orbital ellipse precesses by an angle of  $q \approx 100^\circ$ . For  $v_y = 0.78$  the precession is smaller and reads  $q \approx 90^\circ$  with a larger pericenter distance. We did not follow the runs  $v_y \geq 0.77$  until merger. However the emerging picture is clear: The orbits will have larger pericenter distances during the first encounter. The precession decreases, the merger time and number of close encounters will grow as a result of the smaller radiation losses. We have also find cases in the neutron star binary set that whirl on their second encounter.

### 5.3.3 Effects of truncation error during evolution

Before we extend the discussion of our results, we analyze the effects of the truncation error on our findings, by varying the resolution of our simulations.

#### Conservation of ADM mass

We have analyzed the conservation of the ADM mass as a function of time. If no matter or radiation leaves the grid this quantity should be conserved up to numerical error. We find generically that the ADM mass is preserved to within 3% over the entire evolution time. This gives evidence that the truncation error is not too large.

#### Constraint violations

We analyze Hamiltonian and momentum constraint violations and compare them to standard evolutions of constraint satisfying initial data representing binary neutron stars on quasi-circular orbits as obtained in [170]. The Hamiltonian constraint violations in the eccentric data are larger than the constraint satisfying data during inspiral but comparable during and after merger. This suggests that our approximate initial data does not pose a major limitation for the accuracy of the wave extraction. The violations in the L2-norm are in both cases dominated by the Hamiltonian constraint during the inspiral and by the momentum constraint after the merger. We point out, that the finest box covers the entire star. Mesh refinement levels inside the star have previously been found to introduce large truncation errors. As a consequence of this constraint on the computational grid, the merger

remnants are poorly resolved compared to standard black-hole binary runs. It would be desirable to add a refinement level during merger to resolve this issue.

### Convergence of gravitational waveform

For the case  $D = 50M$ ,  $v_y = 0.01$  we have performed a convergence test for the real part of  $r\Psi_4$  as shown in Fig. 5.4 yielding third order convergence. This finding is different from results in the quasi-circular case [170] where second-order convergence was achieved. This suggests that the data sequence is over-convergent and not yet in the convergent regime. However, the truncation error is small enough for a qualitative study. Short runs with high eccentricity, leading to a direct plunge,

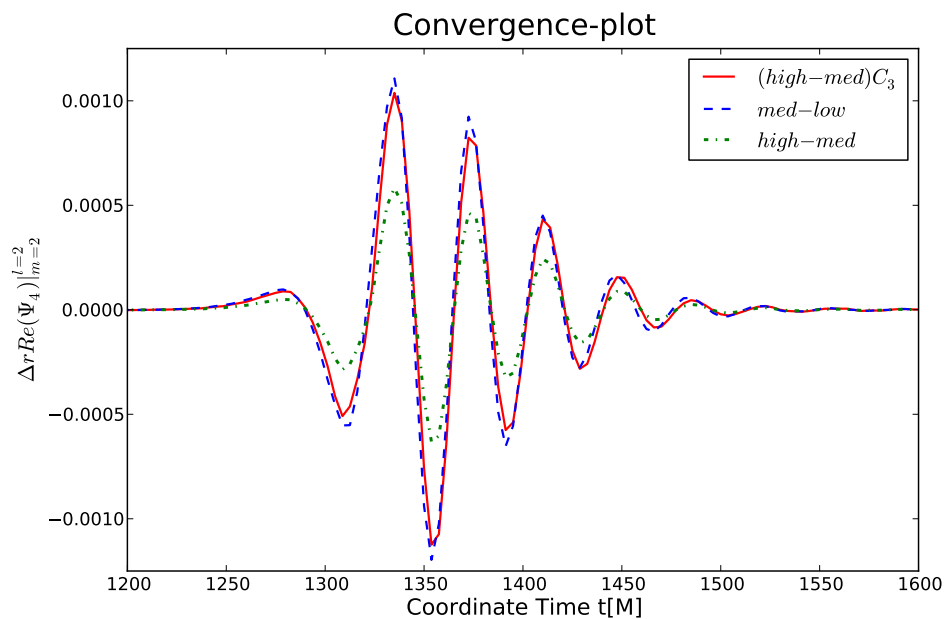


Figure 5.4:  $v_y = 0.01$ ,  $D = 50M$  case: 3rd-order convergence is achieved throughout the merger. Notice the phase shift that becomes quite apparent during ring-down. We emphasize that the waveforms have *not* been aligned for this convergence test.

can be expected to be more accurate than longer runs due to the accumulation of numerical error over time. The truncation error in longer runs, i.e., runs with at least one encounter, can only be shown to be small in the sense that conservation of global quantities, for instance the ADM mass, is maintained within a certain accuracy. The predictions of this study, for example the resulting disk mass, have been checked at different resolutions and yield weak dependence on the numerical resolution. All



major effects reported are generically present and of similar amplitude for different resolution, but there may be a significant drift in parameter space when varying the resolution. Here further investigations with higher resolution are planned. We conclude after this analysis justifies to study the phenomenology and qualitative behavior of eccentric binary neutron stars in the strong-field regime.

### 5.3.4 A representative case

For the remainder of this thesis we pick  $v_y = 0.2$ ,  $D = 50M$  as a representative case and investigate it in detail. We stress that the effects we will discuss are qualitatively also found for other parameters. We mention quantitative differences where appropriate.

#### Bulk motion at early times

Initially, the overall bulk motion is very similar to the black-hole binary case which is expected for large separations, see the orbital trajectories in Figs. 5.2 and 5.3. The stars do not show significant internal dynamics, simply following their orbits, without being deformed. In this early regime the gravitational waveform is very small, see Fig. 5.8. For the binary black hole case and also for quasi-circular neutron star binaries there is a small burst associated with the non-stationarity of the initial data. In our data sets this effect is much smaller. This is most likely because here we do not impose conformal flatness in the initial data. Instead of a Bowen-York momentum we perform a Lorentz-boost on each star.

#### Internal motion and tidal interaction

Tidal interactions have been studied in [188, 189, 190, 191, 192] some of which are applied to binary neutron stars. Initially the neutron stars are irrotational, i.e., the only rotation in the external reference frame is the rotation of the binary. Irrotational binaries are generally believed to be a better assumption, in an astrophysical context, than corotational neutron star binaries, mainly because the viscosity needed inside the stars to keep them in corotation exceeds the values commonly assigned to realistic neutron stars [193, 194]. As the evolution proceeds, tidal interactions due to the finite size of the two stars induce strong internal dynamics, in particular, during the close encounters. These are not seen in the initial data. We will elaborate on this point in the next subsection. The internal dynamics induced will lead

to a response in the neutron star that will be determined by its equation of state and compactness  $C = M/R$ . Thus, tidal interactions in general provide the most promising chance to learn about the equation of state of neutron stars.

### Threshold of immediate merger

Just as in the black-hole binary case, we find whirl phases near the threshold of immediate merger. The neutron stars in this run are just above the threshold, experiencing a strong radial perturbation together with a mild increase in internal rotation induced by the tidal interaction. This is one of the most extreme cases of tidal interaction one can think of. A plot of the density in the  $z = 0$  symmetry plane, see Fig. 5.6 gives an impression of the severe perturbation exerted on the internal dynamics of the neutron stars. In this case the stars separate after the first close encounter though they *touch* (!) each other, as can be seen in Fig. 5.5. Inspecting the waveform in more detail, one can see that these internal dynamics inside the stars show up in the 22 – *mode* of the GWs.

In view of the high sensitivity of the evolution outcome on the initial conditions every single piece of evidence indicates that applying *any* other equation of state or choosing a different compactness will yield vastly different results. The differences will be for example in the merger time, the disk and merger remnant mass, total number of encounters, accretion rates and other disk properties.

### Linking dynamics and observables

It will be of primary importance to verify the significance of imprints related to the matter in the physical observables. The findings from the previous chapter will prove highly useful in this context.

### Gravitational waveform

Most of the features, we have been discussing so far, lead to distinct features in the GW signal. In Fig. 5.8 we show the real part of the 22-mode (multiplied by the radius of the extraction sphere) over time for our representative  $v_y = 0.02, D = 50M$  case. To demonstrate how generic these features are we also show  $v_y = 0.018, D = 50M$  for comparison in Fig. ?? where we have marked the burst associated with the close encounter and the tidally induced waveform signal afterwards. This effect parallels the findings of [187] for the mixed binary case. Just at the onset of merger appears

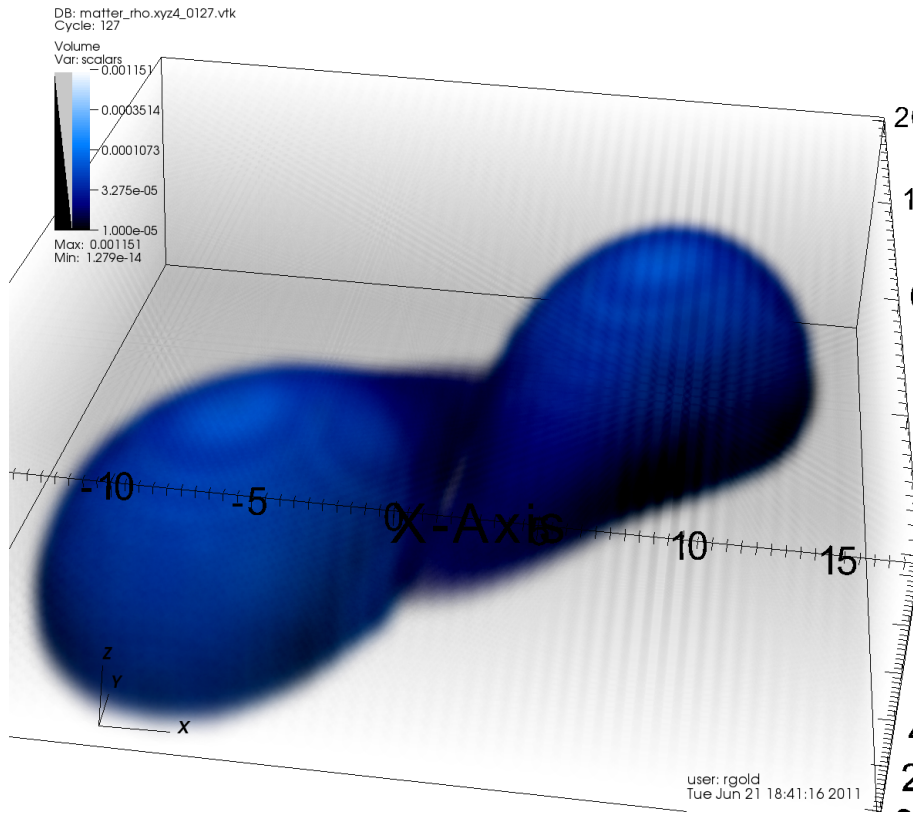


Figure 5.5:  $v_y = 0.02$ ,  $D = 50M$ : On the first encounter the neutron stars touch, but separate again due to the remaining orbital angular momentum.

a feature associated with the almost circular orbit during the whirl phase. During merger the frequency and amplitude increase (the "chirp") before the ring-down signal follows, which is characteristic for the collapse to a black hole which settles down to the Kerr solution. After the merger we cannot measure any sizable signal due to the post-merger dynamics suggesting that the post-merger dynamics are only relevant to the electromagnetic signal of such events.

### Post-Merger

When the neutron stars merge, they may either directly collapse to form a black hole or survive for a short amount of time supported by angular momentum, differential rotation or in general also shock heating for more realistic equations of state. Generically we find negligible disk masses for prompt mergers and massive disks for delayed mergers. We plot the total mass as a function of time in Fig. 5.13

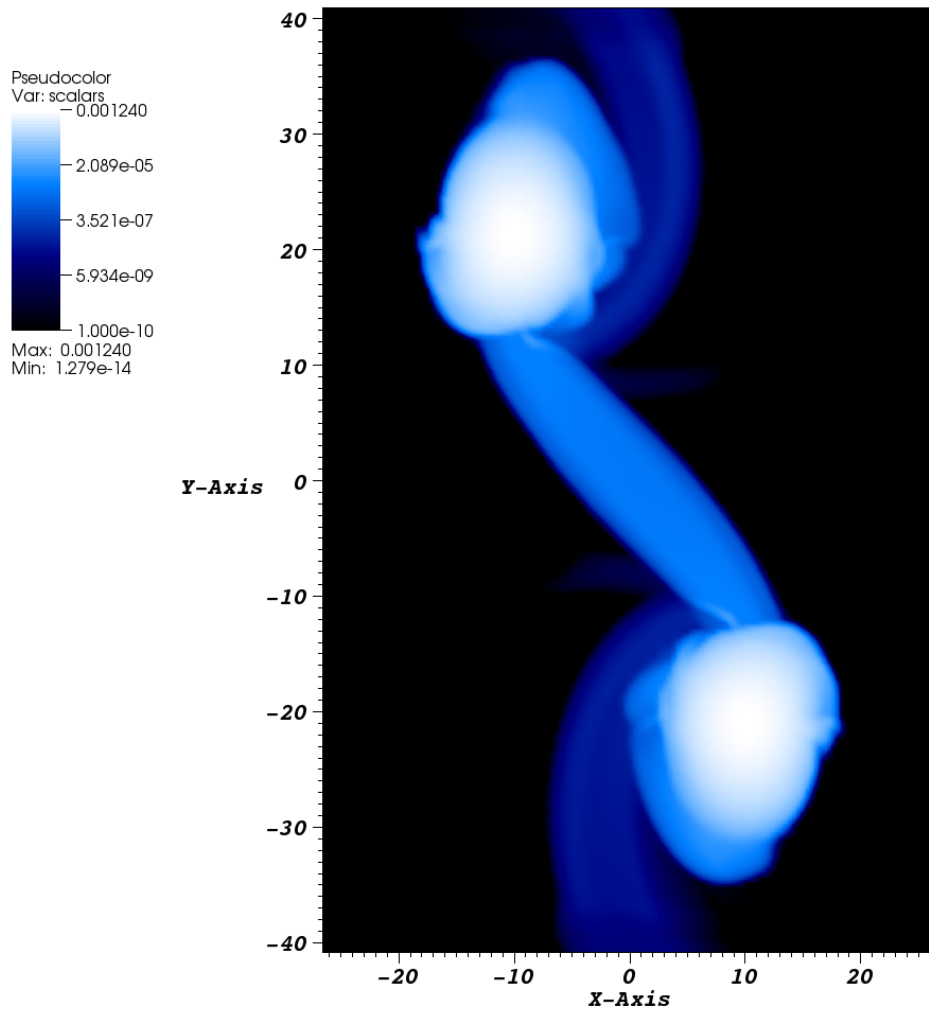


Figure 5.6:  $v_y = 0.02$ ,  $D = 50M$ : After the first encounter the orbit of the neutron stars are strongly perturbed and their shape distorted. The imprints of the tidal perturbation during the encounters on the stars produces signatures in the GWs.

### Disk properties

Beyond a threshold value of the initial orbital angular momentum  $L$ , a disk may form that settles down around the merger remnant. Important predictions for many astrophysical scenarios involve the properties of the resulting disk. In this part we report our results regarding the matter outside the event horizon. We point out,

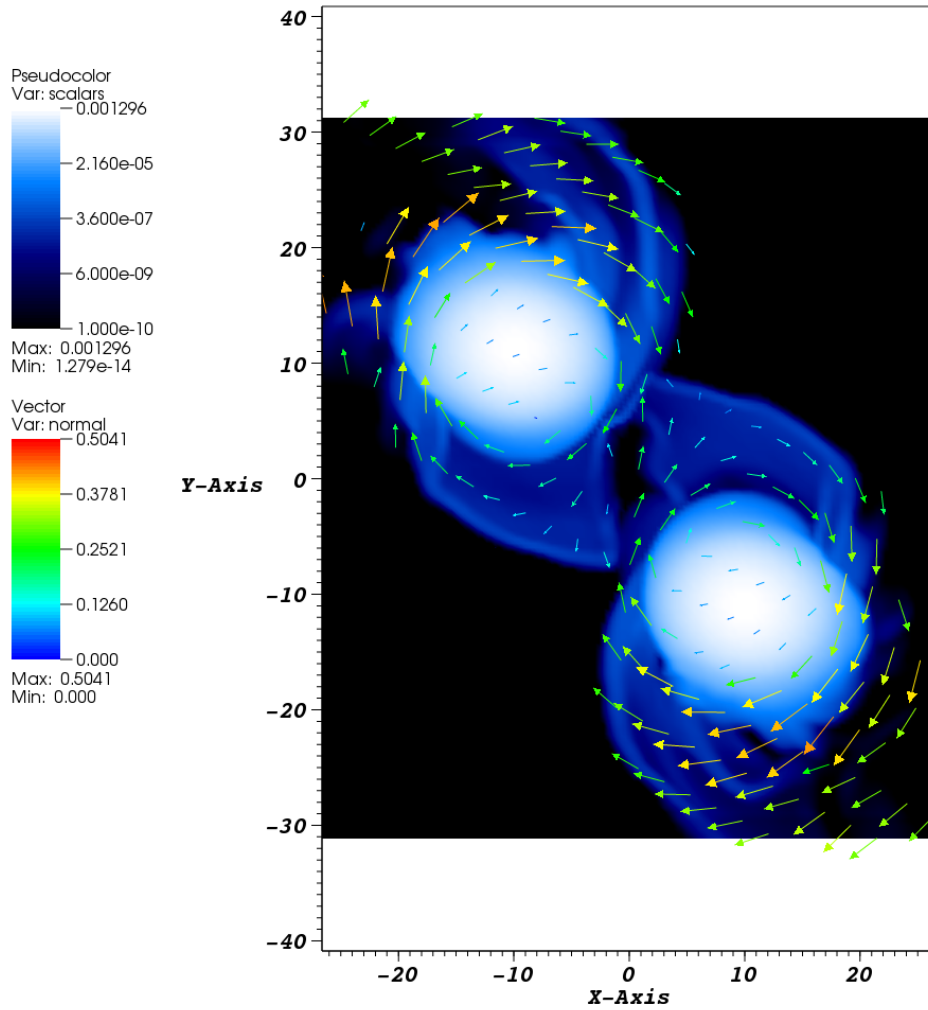


Figure 5.7:  $v_y = 0.02$ ,  $D = 50M$ : In the last encounter the internal structure of the neutron stars is already heavily perturbed from the first encounter. Their overall shape is not spherical and the filaments around each star have a sizable density. This suggests a strong dependence of the emitted gravitational waveform on the equation of state.

though, that for the late times, where the accretion disk forms, our evolutions can only be considered qualitatively, due to the lack of resolution.

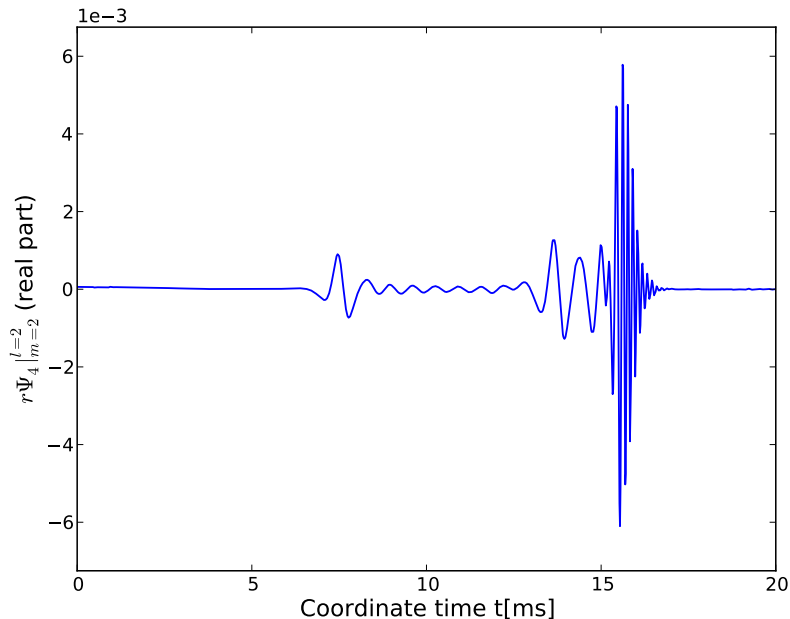


Figure 5.8:  $v_y = 0.02$ ,  $D = 50M$ : Real part of the  $l = 2$ ,  $m = 2$  mode of  $r\Psi_4$ . Note that the junk radiation is too small to appear on the scale of the plot. One can see the first encounter burst, the feature due to the tidally-induced perturbation of the stars (as in Fig. ??), a whirl feature at the onset of merger and the merger signal itself.

### Disk mass

The mass of the disk is expected to grow as a function  $L$ . Our diagnostic computes the rest mass inside the domain which includes matter residuals inside the black hole and also some unbound material. For these reasons our diagnostic yields *upper limits* on the disk mass. We point out, that we observe only negligible ( $\rho < 10^{-10}$  in code units) amounts of matter inside the horizon which quickly disappear.

For  $v_y \leq 0.06$ ,  $D = 20M$  *all* of the matter ends up inside the black hole and no disk or filaments remain outside the horizon. However, just above this plunge regime, as one approaches the threshold of immediate merger, there is a strong dependence of the disk mass on the  $v_y$  or the initial angular momentum, equivalently.

We highlight that a massive disk is the *generic* outcome for tight, eccentric neutron star binaries that survive the first encounter. The disk masses we find for  $e \approx 0.76$ ,  $a = 25M$  are as large as  $M_{disk} \approx 0.1M_\odot$  which is more than enough to produce a gamma ray burst [35, 195]. In this study we have considered only equal-mass binaries. In the quasi-circular regime it was shown that equal-mass

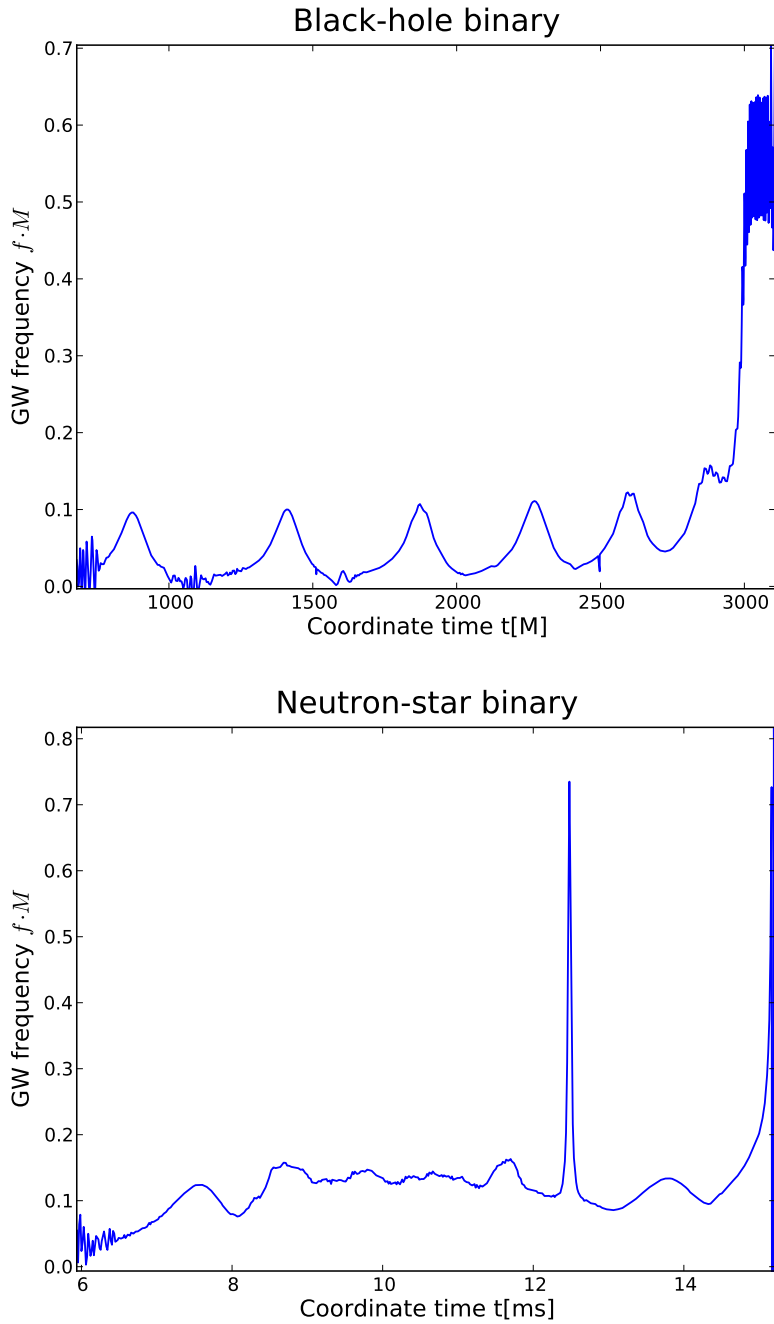


Figure 5.9: The frequency of the gravitational waveform as a function of time for the neutron star binary (bottom plot)  $v_y = 0.2, D = 50M$  case and the black hole binary (top plot)  $\Theta = 60^\circ, P = 1P_{qc}$  case. The gravitational wave frequency in between encounter bursts stays roughly constant for neutron stars while it drops for black hole binaries.

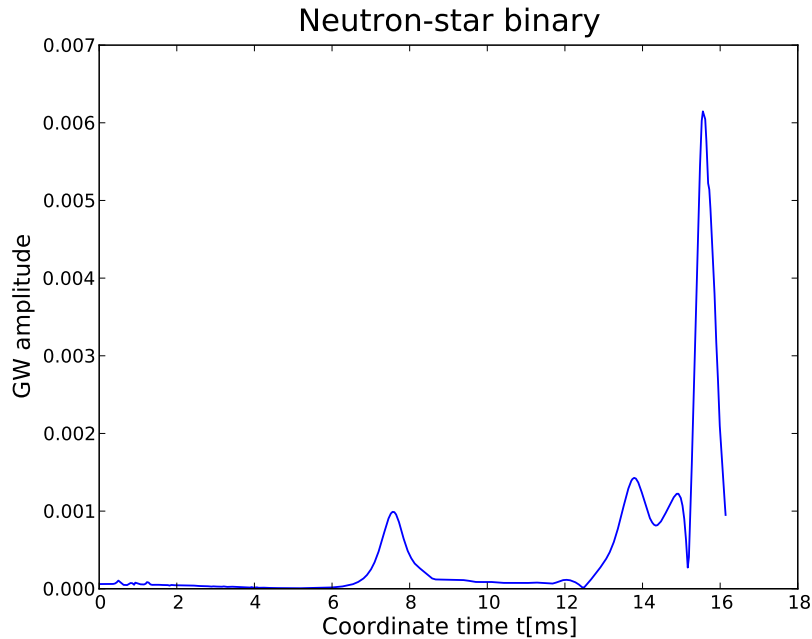


Figure 5.10: The amplitude of the gravitational waveform as a function of time for the neutron star binary  $v_y = 0.2$ ,  $D = 50M$  case.

neutron-star binaries only yield disks with negligible mass and therefore cannot produce to gamma-ray bursts. The same studies indicate that unequal masses produce generically more massive disks.

### Disk rotation profile

A quasi-stationary disk around a black hole closely follows a Keplerian rotation law. However, the disk formed in our runs is far away from this quasi-equilibrium. Hence, the disk will rearrange itself, settling down to a rotation law which should be close to Keplerian, eventually. We observe the relaxation of the disk from the inside out where the orbital timescales are shortest, but we do not follow the disk for long enough to see a stationary rotation on the outer parts. Higher computational power is needed to resolve the disk dynamics well enough in order to study its late-time behavior.

The main driver of disk dynamics shortly after merger is the excessive angular momentum of the fluid elements forcing them on a larger radius and therefore exciting a strong radially outward motion. One can see spiral arms typical for small radial drift velocities in a disk.



In the following the inner parts of the disk, i.e., inward from the inner-most stable circular orbits (ISCO) the disk is increasingly evacuated as expected. This truncation of the inner disk is not easy to reproduce in Newtonian simulations with a pseudo-relativistic potential description for gravity. In fully consistent GR simulations we find this feature generically.

Interestingly there is a phase, where the inner and the outer part of the disk become denser compared to the inner regions. At this stage a shear layer in the outer layers of the disk together with spiral arms cause dynamics, see Fig. 5.12. Whether the shear layer could be unstable to a Kelvin-Helmholtz instability necessitates further study.

#### **Fall-back of matter**

Before the onset of and during merger matter is ejected outwards. However, in our cases only a small amount of matter moves to very large radii or even out of the computational domain. Some of that material falls back on a longer time scale. We observe some of the fall-back at the end of our simulations.

## 5 Binary neutron stars on eccentric orbits

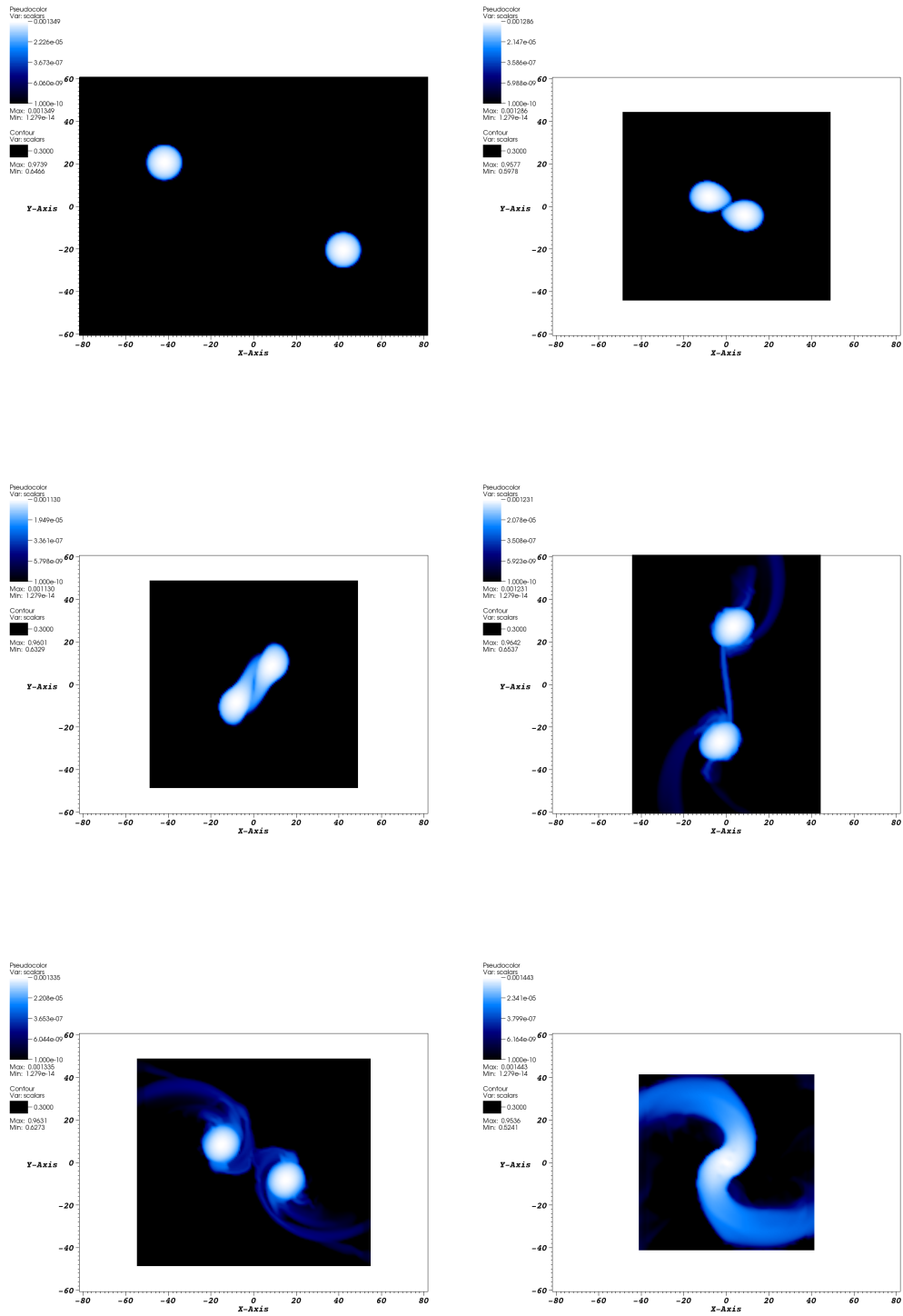


Figure 5.11: Time sequence (left to right - top to bottom) for the  $v_y = 0.02, D = 50M$  case. The encounter occurs between  $7 - 8ms$  after the evolution is started. The onset of merger takes place at  $t \approx 13 - 15ms$ .

### 5.3 Binary case: Results

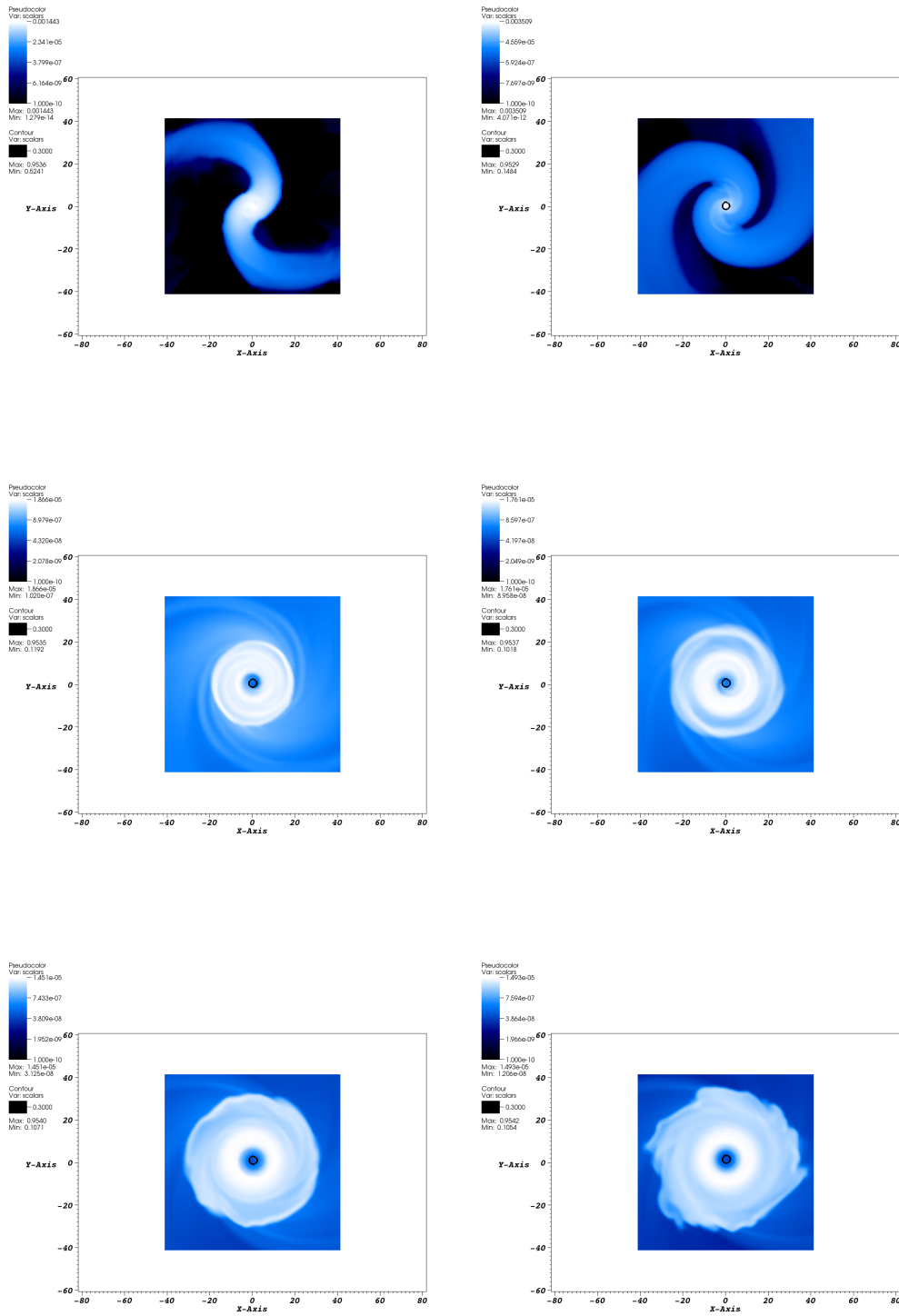


Figure 5.12: The collapse to a black hole takes place at  $t \approx 16ms$ . We follow the disk for roughly  $10ms$ . The black contour is the surface where  $\alpha = 0.3$ , which is rather close to the apparent horizon. Note that the disk quickly develops an evacuated region near the black hole.

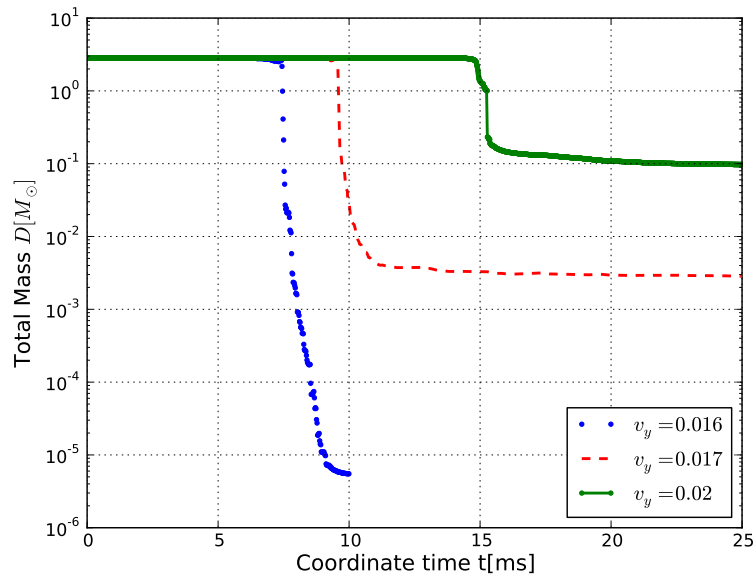


Figure 5.13: Total mass in units of solar mass as a function of time for the representative cases  $v_y = 0.016$ ,  $v_y = 0.017$ ,  $v_y = 0.02$ .

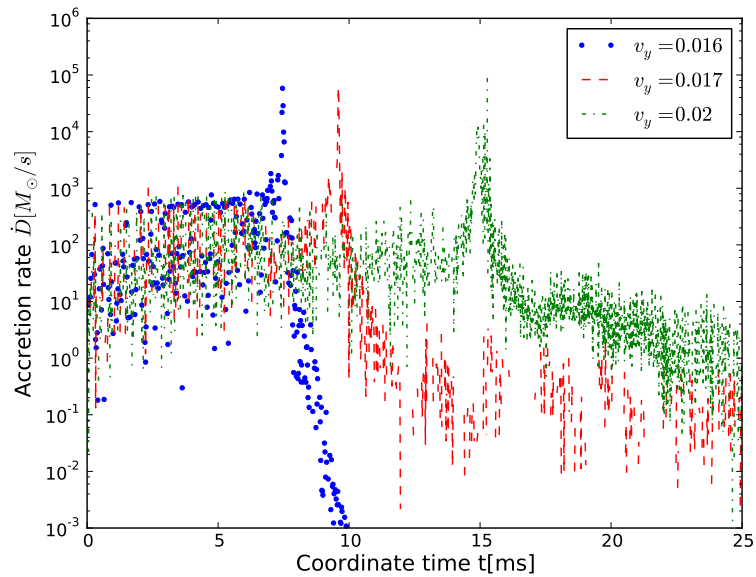


Figure 5.14: Accretion rate in units of solar mass per seconds as a function of time for the representative cases  $v_y = 0.016$ ,  $v_y = 0.017$ ,  $v_y = 0.02$ . The cases with a massive continue to accrete, while the accretion rate for prompt mergers quickly drops.

## 6 Conclusions and outlook

In this thesis we have studied binaries of compact objects, namely black-hole as well as neutron-star binaries, on eccentric orbits. A particular focus has been on zoom-whirl orbits, which can only be found in the strong-field, non-linear regime of General Relativity. For this purpose, numerical methods have been adopted to compute the dynamics and physical observables of the binary using the BSSN formulation and the moving-puncture technique. We have performed a comprehensive parameter study covering a vast range of eccentricities from hyperbolic encounters to the astrophysically more relevant cases of elliptic orbits. We have found zoom-whirl behavior in both regimes. The emitted gravitational waveform as well as the energy loss to gravitational radiation has been characterized and linked to the orbital dynamics. The orbital motion for large separation and the phenomenology for large pericenter passages is similar in the black hole and neutron star cases, but for smaller separation there are differences which in both cases leave distinguishable imprints in the gravitational waveform.

For black hole binaries we have given conclusive evidence that the relevance of zoom-whirl orbits has been underestimated in the past. The conventional understanding, that zoom-whirl orbits are a rare phenomenon arises because of misleading analogies to similar behavior of geodesics in Schwarzschild- or Kerr spacetime. Geodesics, in general, have to be fine-tuned in order to see zoom-whirl orbits, but there is no limit in the number of whirl orbits. We have investigated how this picture changes in the presence of finite-sized objects and close separation where radiation losses and tidal interactions become the dominating effects. We have found that for momenta, which are astrophysically most relevant, not much more than one entire orbit can be achieved during the whirl phase in the equal-mass case.

In view of the relevance of such orbits we find that in the non-linear case of binaries with comparable mass constituents the amount of fine-tuning required in order to see whirl effects is fairly low, corresponding to about one degree in the shooting angle. We show that for a fixed orbital separation and momentum, the regions

where whirl orbits occur, occupy disjunct intervals in the shooting angle. This fine structure of the underlying parameter space implies that whirl effects during the last encounter before coalescence can be found for a discrete set of eccentricity intervals rather than only for sufficiently high eccentricities. However, for lower eccentricities whirl effects in the gravitational waveform decrease and eventually will get lost in the inspiral signal towards the limit of quasi-circular orbits. These discrete features in the parameter space lead to quasi-periodic fluctuations in the radiated energy as a function of the shooting angle. Related fluctuations in the mass of the merger remnant have been reported in [147]. We link this effect to the orbital dynamics, thereby giving a physical interpretation.

Investigating the analogy of zoom-whirl behavior and unstable circular orbits we have shown that binary configurations are more efficient in losing energy via gravitational radiation when they spend more time at small separations. In particular, we find that, for the astrophysically most relevant orbits, whirls at the onset of merger occur at comparatively large separations and thus *decrease* the energy radiated into gravitational waves compared to a quasi-circular orbit in sharp contrast to common expectations from the weak-field approximation.

This work furthermore demonstrates that zoom-whirl orbits give rise to distinct gravitational waveforms due to their unique orbital dynamics. This feature makes them very interesting gravitational wave sources. Our results imply a improved accuracy in parameter estimation for waveforms which exhibit zoom-whirl behavior due to the non-negligible contributions of higher modes and their unique features.

We have extended our analysis beyond the equal-mass regime, covering mass ratios 1:2, 1:3 and 1:4. We find qualitative agreement to the equal-mass cases. The expectation that radiation losses strongly reduce with mass ratio, as known from quasi-circular studies, turns out not to hold. As a consequence the whirl phases are not much longer. In addition studies of the energy radiated and the orbital dynamics strongly suggest that these mass ratios are still far away from the geodesic limit.

It will be promising to extend this analysis to yet higher mass ratios especially in view of new advances in the gauge conditions to handle such spacetimes. Most importantly the inclusion of black hole spin must be expected to greatly enhance features related to zoom-whirl orbits. There is strong astrophysical evidence for spinning black holes, making the extension of this project to the regime where the punctures have spins astrophysically interesting. Furthermore, the high computational efficiency of black hole binary evolutions enables the possibility to perform

large parameter surveys. It will be interesting to perform fully consistent relativistic simulation for the binaries with sufficiently high eccentricity and small semi-major axis found in the data from N-body simulations of globular clusters. Such a study would shed light on the relevance of zoom-whirl orbits in globular clusters.

In the second part of this thesis we have studied eccentric neutron star binaries. These systems have not been studied in full General Relativity before. Realizing that the accuracy of binary neutron star evolutions is limited by the truncation error of the evolution scheme we use a linear superposition of two boosted single spherical star configurations as *approximate* initial data for fully relativistic evolutions. We discover, for the first time, zoom-whirl orbits in binary neutron stars.

All our evolutions merge within the simulation time and collapse to form a black hole. Exceptions are test cases in the low eccentricity regime, which we did not follow for more than two orbits. Depending on the initial eccentricity there may be delayed collapse due to the formation of a hypermassive neutron star. We have studied cases with one and two encounters. The evolutions that survive the first encounter including those merging through a whirl phase during their first encounter produce an accretion disk. The mass of the disk increases monotonically with lower eccentricities within the range of our study.

Our most important finding concerns the large values of disk mass that can be obtained. For eccentricities large enough to cause a direct plunge, essentially no disk material is left behind. However, in the more modest eccentricity case  $e \lesssim 0.7$ , we find disk masses as large as  $\lesssim 0.1$  solar masses, which easily provides enough material for a short gamma-ray burst scenario. In quasi-circular studies of neutron star binaries it was found that the disk mass for the equal-mass case is completely negligible, thus completely outruling them as potential candidates for short gamma-ray bursts. Considering unequal-mass cases of 1:3 or more give rises to sufficient disk masses, but the distribution of observed neutron star masses is rather narrowly concentrated around  $\sim 1.4$  solar masses suggesting that (near-) equal-mass cases should be much more common than mass ratios of 1:3 or even larger.

The accretion disks are highly dynamical, driven initially by radial motion of fluid elements, which cause spiral arms throughout the disk. Soon the region close to the black hole where no stable circular orbits exist becomes evacuated. The disk dynamics settle down fastest at small radii where the orbital time scale is shortest. In the outer parts of the disk ( $r_{out}^{disk} \gtrsim 10M$ ) dynamics of spiral arms, dynamics due to material falling back and effects related to a shear layer remain visible.

## 6 Conclusions and outlook

We find that tidal interactions are extremely high during tight close encounters or during whirl phases. In limiting cases we observe that the neutron stars even touch each other exchanging material during their first encounter and yet separate again before they merge on their next close encounter. Also in more general cases tidal interactions during the first encounter perturb the neutron stars heavily causing an internal rotation and a strong wobbling. These effects generically alter the waveform compared to the quasi-circular case leading to a signal with a rather constant amplitude and frequency. The latter corresponds to the instantaneous gravitational wave frequency during pericenter during which the perturbation was mainly caused. An interesting observation is that in an analogous case with black hole binaries the gravitational wave frequency and amplitude both decrease after the close encounter, hence making the distinction to neutron star binaries obvious. The strong imprints of the tidally-induced internal rotation stresses the importance of including such effects in future initial data prescriptions for eccentric neutron star binaries.

We give evidence that the tidal interaction during close encounters and in particular whirl orbits, as they may occur in eccentric neutron star binaries, dramatically increases the sensitivity of the emitted gravitational waveform on the equation of state of the nuclear matter. In our models we have only used a polytropic equation of state, but the large solution dependence on initial parameters and the induced, severe, internal dynamics imply that the evolution as well as the waveform will crucially depend on the equation of state. Gravitational waves from eccentric neutron star binaries may thus tell us much about the QCD phase diagram [196].

There are numerous ways to extend this work. A massive disk is not the only prerequisite to obtain short gamma-ray bursts. In order to actually launch one, magnetic fields are clearly needed. Furthermore a detailed study of the electromagnetic signatures due to accretion and synchrotron or neutrino emission could yield interesting insights for short gamma-ray-bursts.

Another aspect which opens up many possible projects is to study the corresponding settings in a mixed binary composed of a neutron star and a black hole. The latter may be chosen to have spin. So far studies of such systems have only begun and there is much more to learn about them.

In conclusion, eccentric binaries of compact objects are fascinating systems to study General Relativity. With the exciting prospect of detections of gravitational waves in the next few years one expects new discoveries unveiling the nature of compact objects in strong field gravity.



# Bibliography

- [1] Albert Einstein. Zur Allgemeinen Relativitätstheorie. *Preuss. Akad. Wiss. Berlin, Sitzungsber.*, pages 778–786, 1915.
- [2] Albert Einstein. Die Feldgleichungen der Gravitation. *Preuss. Akad. Wiss. Berlin, Sitzungsber.*, pages 844–847, 1915.
- [3] Dimitrios Psaltis. Probes and tests of strong-field gravity with observations in the electromagnetic spectrum. *Living Reviews in Relativity*, 11(9), 2008.
- [4] LISA (laser interferometer space antenna), proposal for a gravitational wave detector in space. Preprint, Max-Planck-Institut für Quantenoptik, MPQ 177, May 1993.
- [5] S Kawamura et al. The japanese space gravitational wave antenna; decigo. *Journal of Physics: Conference Series*, 120, 2008.
- [6] Erik Schnetter. Finding apparent horizons and other two-surfaces of constant expansion. *Class. Quantum Grav.*, 20(22):4719–4737, 2003.
- [7] L. Blanchet. Post-Newtonian theory and the two-body problem. *ArXiv e-prints*, July 2009.
- [8] Yousuke Itoh Toshifumi Futamase. The post-newtonian approximation for relativistic compact binaries. *Living Reviews in Relativity*, 10(2), 2007.
- [9] A. Buonanno and T. Damour. Effective one-body approach to general relativistic two-body dynamics. *Phys. Rev. D*, 59:084006, 1999.
- [10] Thibault Damour and Alessandro Nagar. Improved analytical description of inspiralling and coalescing black-hole binaries. *Phys. Rev. D*, 79(8):081503, Apr 2009.
- [11] Benjamin Aylott et al. Testing gravitational-wave searches with numerical relativity waveforms: Results from the first Numerical INjection Analysis (NINJA) project. *Class. Quant. Grav.*, 26:165008, 2009.
- [12] Y. Pan, A. Buonanno, M. Boyle, L. T. Buchman, L. E. Kidder, H. P. Pfeiffer, and M. A. Scheel. Inspiral-merger-ringdown multipolar waveforms of non-spinning black-hole binaries using the effective-one-body formalism. *ArXiv e-prints*, June 2011.

## Bibliography

- [13] Mark Hannam and Ian Hawke. Numerical relativity simulations in the era of the Einstein Telescope. *Gen. Rel. Grav.*, 43:465–483, 2011.
- [14] Karl Schwarzschild. Über das Gravitationsfeld eines Massenpunktes nach der Einsteinschen Theorie. *Sitzungsber. Dtsch. Akad. Wiss. Berlin, Kl. Math. Phys. Tech.*, pages 189–196, 1916.
- [15] G.D. Birkhoff. *Relativity and Modern Physics*. Harvard University Press, Cambridge Mass., 1923.
- [16] J. R Oppenheimer and H. Snyder. On Continued Gravitational Contraction. *Phys. Rev.*, 56:455–459, 1939.
- [17] Frans Pretorius. Evolution of binary black hole spacetimes. *Phys. Rev. Lett.*, 95:121101, 2005.
- [18] Manuela Campanelli, Carlos O. Lousto, Pedro Marronetti, and Yosef Zlochower. Accurate evolutions of orbiting black-hole binaries without excision. *Phys. Rev. Lett.*, 96:111101, 2006.
- [19] Frans Pretorius and Deepak Khurana. Black hole mergers and unstable circular orbits. *Class. Quant. Grav.*, 24:S83–S108, 2007.
- [20] Bernd Brügmann, Wolfgang Tichy, and Nina Jansen. Numerical simulation of orbiting black holes. *Phys. Rev. Lett.*, 92:211101, 2004.
- [21] S. T. McWilliams. The Status of Black-Hole Binary Merger Simulations with Numerical Relativity. *ArXiv e-prints*, December 2010.
- [22] Doreen Müller and Bernd Brügmann. Toward a dynamical shift condition for unequal mass black hole binary simulations. *Class. Quant. Grav.*, 27:114008, 2010.
- [23] Doreen Müller, Jason Grigsby, and Bernd Brügmann. Dynamical shift condition for unequal mass black hole binaries. *Phys. Rev.*, D82:064004, 2010.
- [24] Geoffrey Lovelace, Mark. A. Scheel, and Bela Szilagy. Simulating merging binary black holes with nearly extremal spins. *Phys. Rev.*, D83:024010, 2011.
- [25] Carlos O. Lousto and Yosef Zlochower. Orbital evolution of extreme-mass-ratio black-hole binaries with numerical relativity. *Phys. Rev. Lett.*, 106:041101, 2011.
- [26] P. C. Peters and J. Mathews. Gravitational radiation from point masses in a Keplerian orbit. *Phys. Rev.*, 131:435–440, 1963.
- [27] P. C. Peters. Gravitational radiation and the motion of two point masses. *Phys. Rev.*, 136:B1224–B1232, 1964.

- [28] Duncan A. Brown and Peter J. Zimmerman. The effect of eccentricity on searches for gravitational-waves from coalescing compact binaries in ground-based detectors, 2009.
- [29] Ryan M. O’Leary and Abraham Loeb. Star clusters around recoiled black holes in the milky way halo, 2008.
- [30] Ryan M. O’Leary, Bence Kocsis, and Abraham Loeb. Gravitational waves from scattering of stellar-mass black holes in galactic nuclei, 2008.
- [31] Linqing Wen. On the eccentricity distribution of coalescing black hole binaries driven by the kozai mechanism in globular clusters. *The Astrophysical Journal*, 598:419, 2003.
- [32] Y. Kozai. Secular perturbations of asteroids with high inclination and eccentricity. *Astron. J.*, 67:591–598, 1962.
- [33] M. J. Valtonen, S. Mikkola, D. Merritt, A. Gopakumar, H. J. Lehto, T. Hyvonen, H. Rampadarath, R. Saunders, M. Basta, and R. Hudec. Measuring the spin of the primary black hole in oj287, 2009.
- [34] B. S. Sathyaprakash and B. F. Schutz. Physics, Astrophysics and Cosmology with Gravitational Waves. *Living Rev. Rel.*, 12:2, 2009.
- [35] M. D. Duez. Numerical relativity confronts compact neutron star binaries: a review and status report. *Classical and Quantum Gravity*, 27(11):114002–+, June 2010.
- [36] Gregory B. Cook. Initial data for numerical relativity. *Living Rev. Relativity*, 3:5, 2000.
- [37] Carsten Gundlach and Jose M. Martin-Garcia. Well-posedness of formulations of the Einstein equations with dynamical lapse and shift conditions. *Phys. Rev.*, D74:024016, 2006.
- [38] Miguel Alcubierre. *Introduction to 3+1 numerical relativity*. 2008.
- [39] Thomas Baumgarte and Stuart Shapiro. *Numerical Relativity: Solving Einstein’s Equations on the Computer*. Cambridge University Press, Cambridge, 2010.
- [40] Ericourgoulhon. 3+1 formalism and bases of numerical relativity. 2007.
- [41] Y. Bruhat. Theoreme d’existence pour certains systemes d’equations aux derivees partielles non lineaires. *Acta Mathematica*, 88:141–225, 1952.
- [42] Y. Bruhat. The cauchy problem. In L. Witten, editor, *Gravitation: An Introduction to Current Research*. Wiley, New York, 1962.

## Bibliography

- [43] A. Lichnerowicz. L'intégration des équations de la gravitation relativiste et le problème des  $n$  corps. *J. Math. Pures et Appl.*, 23:37–63, 1944.
- [44] R. Arnowitt, S. Deser, and Charles W. Misner. The dynamics of general relativity. In L. Witten, editor, *Gravitation: An Introduction to Current Research*, pages 227–265. Wiley, New York, 1962.
- [45] Matthew William Anderson. *Constrained Evolution in Numerical Relativity*. PhD thesis, The University of Texas at Austin, Austin, Texas, U.S.A., 2004.
- [46] Vasileios Paschalidis, Alexei Khokhlov, and Igor D. Novikov. Well-posed constrained evolution of 3+1 formulations of general relativity. 2005.
- [47] G Darmois. Memorial de sciences mathematiques, fascicule xxv, "les equations de la gravitation einsteinienne", chapitre v. In 2919[10] Barrab'es C and Israel W 1991 *Phys. Rev. D* 43 1129 [11] Lake K 1979 *Phys. Rev. D* 19 2847[12] Sato H 1986 *Prog. Theor. Phys.* 76 1250 [13] Sakai N and Maeda K 1994 *Phys. Rev. D* 50 5425[14] Lichnerowicz A 1955 *Th'eories Relativistes de la Gravitatio*, 1927.
- [48] P. A. M. Dirac. *Proc. R. Soc. London*, A246:326, 1958.
- [49] J. W. York, Jr. Kinematics and dynamics of general relativity. In L. Smarr, editor, *Sources of Gravitational Radiation*, pages 83–126, Cambridge, 1979. Cambridge University Press.
- [50] J. M. Bowen and J. W. York, Jr. Time-asymmetric initial data for black holes and black-hole collisions. *Phys. Rev. D*, 21:2047–2056, 1980.
- [51] N. Ó Murchadha and J. York. Existence and uniqueness of solutions of the Hamiltonian constraint of general relativity on compact manifolds. *J. Math. Phys.*, 14:1551–1557, 1973.
- [52] S. Brandt and B. Brügmann. A simple construction of initial data for multiple black holes. *Phys. Rev. Lett.*, 78(19):3606–3609, 1997.
- [53] A. Garat and R. H. Price. Nonexistence of conformally flat slices of the kerr spacetime. *Phys. Rev. D*, 61:124011, 2000. gr-qc/0002013.
- [54] C. Bona, Joan Massó, and J. Stela. Numerical black holes: A moving grid approach. *Phys. Rev. D*, 51:1639–1645, 1995.
- [55] David Hilditch and Ronny Richter. Hyperbolic formulations of General Relativity with Hamiltonian structure. 2010.
- [56] Bernd Brügmann, José A. González, Mark Hannam, Sascha Husa, Ulrich Sperhake, and Wolfgang Tichy. Calibration of Moving Puncture Simulations. *Phys. Rev.*, D77:024027, 2008.

- [57] Mark Hannam, Sascha Husa, Bernd Brügmann, and Achamveedu Gopakumar. Comparison between numerical-relativity and post-Newtonian waveforms from spinning binaries: the orbital hang-up case. *Phys. Rev.*, D78:104007, 2008.
- [58] Frank Estabrook, Hugo Wahlquist, Steve Christensen, Bryce DeWitt, Larry Smarr, and Elaine Tsiang. Maximally slicing a black hole. *Phys. Rev. D*, 7(10):2814–2817, 1973.
- [59] Marcus Thierfelder, Sebastiano Bernuzzi, David Hilditch, Bernd Brügmann, and Luciano Rezzolla. The trumpet solution from spherical gravitational collapse with puncture gauges. *Phys.Rev.*, D83:064022, 2011.
- [60] Carsten Gundlach and Jose M. Martin-Garcia. Hyperbolicity of second-order in space systems of evolution equations. *Class. Quant. Grav.*, 23:S387–S404, 2006.
- [61] Frans Pretorius. Numerical relativity using a generalized harmonic decomposition. *Class. Quant. Grav.*, 22:425–452, 2005.
- [62] M. Shibata and T. Nakamura. Evolution of three-dimensional gravitational waves: Harmonic slicing case. *Phys. Rev. D*, 52:5428–5444, 1995.
- [63] T. W. Baumgarte and S. L. Shapiro. On the Numerical integration of Einstein’s field equations. *Phys. Rev. D*, 59:024007, 1998.
- [64] A. M. Knapp, E. J. Walker, and Thomas W. Baumgarte. Illustrating stability properties of numerical relativity in electrodynamics. *Phys. Rev. D*, 65:064031, 2002. gr-qc/0201051.
- [65] M. Alcubierre, G. Allen, B. Brügmann, E. Seidel, and W.-M. Suen. Towards an understanding of the stability properties of the 3+1 evolution equations in general relativity. *Phys. Rev. D*, 62:124011, 2000. gr-qc/9908079.
- [66] O. Sarbach, G. Calabrese, J. Pullin, and M. Tiglio. Hyperbolicity of the BSSN system of Einstein evolution equations. *Phys. Rev. D*, 66:064002, 2002.
- [67] Horst Beyer and Olivier Sarbach. On the well posedness of the Baumgarte-Shapiro- Shibata-Nakamura formulation of Einstein’s field equations. *Phys. Rev. D*, 70:104004, 2004.
- [68] C. Palenzuela C. Bona, T. Ledvinka and M. Zacek. General-covariant evolution formalism for Numerical Relativity.
- [69] C. Bona and C. Palenzuela. Dynamical shift conditions for the Z4 and BSSN hyperbolic formalisms. *Phys. Rev. D*, 69:104003, 2004.
- [70] C. Bona, T. Ledvinka, C. Palenzuela-Luque, and M. Zacek. Constraint-preserving boundary conditions in the Z4 Numerical Relativity formalism. *Class. Quant. Grav.*, 22:2615–2634, 2005.

## Bibliography

- [71] Milton Ruiz, David Hilditch, and Sebastiano Bernuzzi. Constraint preserving boundary conditions for the Z4c formulation of general relativity. *Phys. Rev.*, D83:024025, 2011.
- [72] Sebastiano Bernuzzi and David Hilditch. Constraint violation in free evolution schemes: comparing BSSNOK with a conformal decomposition of Z4. *Phys. Rev.*, D81:084003, 2010.
- [73] Carsten Gundlach, Jose M. Martin-Garcia, Gioel Calabrese, and Ian Hinder. Constraint damping in the Z4 formulation and harmonic gauge. *Class. Quant. Grav.*, 22:3767–3774, 2005.
- [74] Oliver Rinne. *Axisymmetric Numerical Relativity*. PhD thesis, University of Cambridge, Cambridge, England, 13 September 2005. gr-qc/0601064.
- [75] Erik Schnetter, Peter Diener, Nils Dorband, and Manuel Tiglio. A multi-block infrastructure for three-dimensional time-dependent numerical relativity. *Class. Quantum Grav.*, 23:S553–S578, 2006.
- [76] Pedro Marronetti et al. Binary black holes on a budget: Simulations using workstations. *Class. Quant. Grav.*, 24:S43–S58, 2007.
- [77] Marsha J. Berger and Joseph Olinger. Adaptive mesh refinement for hyperbolic partial differential equations. *J. Comput. Phys.*, 53:484–512, 1984.
- [78] Ezra T. Newman and Roger Penrose. An approach to gravitational radiation by a method of spin coefficients. *J. Math. Phys.*, 3(3):566–578, 1962. erratum in *J. Math. Phys.* 4, 998 (1963).
- [79] S. Chandrasekhar. *The Mathematical Theory of Black Holes*. Oxford University Press, Oxford, England, 1983.
- [80] Ian Hinder, Barry Wardell, and Eloisa Bentivegna. Falloff of the Weyl scalars in binary black hole spacetimes. 2011.
- [81] A. KURGANOV and S. TSYNKOV. On spectral accuracy of quadrature formulae based on piecewise polynomial interpolation. 2005.
- [82] S. A. Teukolsky, W. T. Vetterling, and B. P. Flannery. Numerical recipes in c. 1997.
- [83] J. P. Boyd. Chebyshev and fourier spectral methods. 1989.
- [84] L. N. Trefethen. Spectral methods in matlab. 2000.
- [85] R. P. Kerr. Gravitational field of a spinning mass as an example of algebraically special metrics. *Phys. Rev. Lett.*, 11:237–238, 1963.

- [86] R. A. Hulse and J. H. Taylor. Discovery of a Pulsar in a Binary System. *ApJ*, 195:L51–55, 1975.
- [87] J. M. Weisberg and J. H. Taylor. Gravitational radiation from an orbiting pulsar. *General Relativity and Gravitation*, 13:1–6, January 1981.
- [88] Miguel Alcubierre et al. Dynamical evolution of quasi-circular binary black hole data. *Phys. Rev.*, D72:044004, 2005.
- [89] Harald P. Pfeiffer et al. Reducing orbital eccentricity in binary black hole simulations. *Class. Quant. Grav.*, 24:S59–S82, 2007.
- [90] John G. Baker et al. Mergers of non-spinning black-hole binaries: Gravitational radiation characteristics. *Phys. Rev.*, D78:044046, 2008.
- [91] Yuk Tung Liu, Zachariah B. Etienne, and Stuart L. Shapiro. Evolution of near-extremal-spin black holes using the moving puncture technique. *Phys. Rev.*, D80:121503, 2009.
- [92] Bela Szilagyi, Lee Lindblom, and Mark A. Scheel. Simulations of binary black hole mergers using spectral methods. *Phys. Rev.*, D80:124010, 2009.
- [93] Michael Kesden, Guglielmo Lockhart, and E. Sterl Phinney. Maximum black-hole spin from quasi-circular binary mergers. *Phys. Rev.*, D82:124045, 2010.
- [94] M. Turner. Gravitational radiation from point-masses in unbound orbits - Newtonian results. *Astrophysical Journal*, 216:610–619, September 1977.
- [95] Irwin I. Shapiro, Gordon H. Pettengill, Michael E. Ash, Richard P. Ingalls, D. B. Campbell, and R. B. Dyce. Mercury’s perihelion advance: Determination by radar. *Phys. Rev. Lett.*, 28(24):1594–1597, Jun 1972.
- [96] Nicolas Yunes and Emanuele Berti. Accuracy of the Post-Newtonian Approximation: Optimal Asymptotic Expansion for Quasi-Circular, Extreme-Mass Ratio Inspirals. *Phys. Rev.*, D77:124006, 2008.
- [97] Zhongyang Zhang, Nicolas Yunes, and Emanuele Berti. Accuracy of the post-Newtonian approximation. II. Optimal asymptotic expansion of the energy flux for quasicircular, extreme mass-ratio inspirals into a Kerr black hole. 2011.
- [98] Clifford M. Will. On the unreasonable effectiveness of the post-Newtonian approximation in gravitational physics. 2011.
- [99] Curt Cutler, Daniel Kennefick, and Eric Poisson. Gravitational radiation reaction for bound motion around a schwarzschild black hole. *Phys. Rev. D*, 50(6):3816–3835, Sep 1994.
- [100] Simon Portegies Zwart and Stephen McMillan. Black hole mergers in the universe, 1999.

## Bibliography

- [101] M. J. Benacquista, S. Portegies Zwart, and F. A. Rasio. Lisa sources in globular clusters. *Classical and Quantum Gravity*, 18:4025, 2001.
- [102] D. Pooley, W. H. G. Lewin, S. F. Anderson, H. Baumgardt, A. V. Filippenko, B. M. Gaensler, L. Homer, P. Hut, V. M. Kaspi, B. Margon, S. McMillan, S. Portegies Zwart, M. van der Klis, and F. Verbunt. Dynamical formation of close binary systems in globular clusters, 2003.
- [103] M. Coleman Miller and Douglas P. Hamilton. Four-body effects in globular cluster black hole coalescence, 2002.
- [104] Warren R. Brown. Hypervelocity stars and the galactic center, 2008.
- [105] Simon Portegies Zwart, Holger Baumgardt, Stephen L. W. McMillan, Junichiro Makino, Piet Hut, and Toshi Ebisuzaki. The ecology of star clusters and intermediate mass black holes in the galactic bulge, 2005.
- [106] Omer Blaes, Man Hoi Lee, and Aristotle Socrates. The kozai mechanism and the evolution of binary supermassive black holes. *The Astrophysical Journal*, 578:775, 2002.
- [107] Clovis Hopman and Tal Alexander. The orbital statistics of stellar inspiral and relaxation near a massive black hole: characterizing gravitational wave sources. *The Astrophysical Journal*, 629:362, 2005.
- [108] Karl Martel. Detection of gravitational waves from eccentric compact binaries, 1999.
- [109] Karl Martel and Eric Poisson. Gravitational waves from eccentric compact binaries: Reduction in signal-to-noise ratio due to nonoptimal signal processing. *Physical Review D*, 60:124008, 1999.
- [110] Ilya Mandel, Duncan A. Brown, Jonathan R. Gair, and M. Coleman Miller. Rates and characteristics of intermediate mass ratio inspirals detectable by advanced ligo. *The Astrophysical Journal*, 681:1431, 2008.
- [111] Pablo Galaviz and Bernd Brügmann. Characterization of the gravitational wave emission of three black holes. 2010.
- [112] Pablo Galaviz, Bernd Brügmann, and Zhoujian Cao. Numerical evolution of multiple black holes with accurate initial data. 2010.
- [113] Masaki Iwasawa, Yoko Funato, and Junichiro Makino. Evolution of massive blackhole triples i – equal-mass binary-single systems, 2005.
- [114] Marta Volonteri, Francesco Haardt, and Piero Madau. The assembly and merging history of supermassive black holes in hierarchical models of galaxy formation. *The Astrophysical Journal*, 582:559, 2003.



- [115] M. J. Valtonen, H. J. Lehto, K. Nilsson, J. Heidt, L. O. Takalo, A. Sillanpaa, C. Villforth, M. Kidger, G. Poyner, T. Pursimo, S. Zola, J. H. Wu, X. Zhou, K. Sadakane, M. Drozd, D. Koziel, D. Marchev, W. Ogloza, C. Porowski, M. Siwak, G. Stachowski, M. Winiarski, V. P. Hentunen, M. Nissinen, A. Liakos, and S. Dogru. A massive binary black-hole system in oj287 and a test of general relativity, 2008.
- [116] Frans Pretorius. Binary Black Hole Coalescence. 2007.
- [117] Mark A. Scheel, Harald P. Pfeiffer, Lee Lindblom, Lawrence E. Kidder, Oliver Rinne, and Saul A. Teukolsky. Solving Einstein’s equations with dual coordinate frames. *Phys. Rev. D*, 74:104006, 2006.
- [118] M. J. Fitchett. The influence of gravitational wave momentum losses on the centre of mass motion of a newtonian binary system. *MNRAS*, 203:1049–1062, 1983.
- [119] James Healy et al. Superkicks in Hyperbolic Encounters of Binary Black Holes. *Phys. Rev. Lett.*, 102:041101, 2009.
- [120] M. Megevand, M. Anderson, J. Frank, E. W. Hirschmann, L. Lehner, S. L. Liebling, P. M. Motl, and D. Neilsen. Perturbed disks get shocked: Binary black hole merger effects on accretion disks. *Phys. Rev. D*, 80(2):024012–+, July 2009.
- [121] Kostas Glampedakis and Daniel Kennefick. Zoom and whirl: eccentric equatorial orbits around spinning black holes and their evolution under gravitational radiation reaction. *Phys. Rev.*, D66:044002, 2002.
- [122] James Healy, Janna Levin, and Deirdre Shoemaker. Zoom-Whirl Orbits in Black Hole Binaries. *Phys. Rev. Lett.*, 103:131101, 2009.
- [123] Ivan R. King. The Structure of star clusters. 3. Some simple dynamical models. *Astron. J.*, 71:64, 1966.
- [124] Dean E. McLaughlin et al. HST Proper Motions and Stellar Dynamics in the Core of the Globular Cluster 47 Tucanae. *Astrophys. J. Suppl.*, 166:249, 2006.
- [125] S. Chandrasekhar. *The Mathematical Theory of Black Holes*. Oxford University Press, USA, 1983.
- [126] Karl Martel. Gravitational waveforms from a point particle orbiting a schwarzschild black hole. *Physical Review D*, 69:044025, 2004.
- [127] Janna Levin and Gabe Perez-Giz. A periodic table for black hole orbits, 2008.
- [128] Steve Drasco and Scott A. Hughes. Gravitational wave snapshots of generic extreme mass ratio inspirals. *Physical Review D*, 73:024027, 2006.

## Bibliography

- [129] Roland Haas. Scalar self-force on eccentric geodesics in Schwarzschild space-time: a time-domain computation. *Phys. Rev.*, D75:124011, 2007.
- [130] Janna Levin and Becky Grossman. Dynamics of black hole pairs i: Periodic tables. *Physical Review D*, 79:043016, 2009.
- [131] Rebecca Grossman and Janna Levin. Dynamics of black hole pairs ii: Spherical orbits and the homoclinic limit of zoom-whirliness. *Physical Review D*, 79:043017, 2009.
- [132] Scott A. Hughes, Steve Drasco, Éanna É. Flanagan, and Joel Franklin. Gravitational radiation reaction and inspiral waveforms in the adiabatic limit. *Phys. Rev. Lett.*, 94(22):221101, Jun 2005.
- [133] Michael E. Pati and Clifford M. Will. Post-Newtonian gravitational radiation and equations of motion via direct integration of the relaxed Einstein equations. II. two-body equations of motion to second post-Newtonian order, and radiation reaction to 3.5 post-Newtonian order. *Phys. Rev. D*, 65:104008, 2002.
- [134] U. Sperhake, E. Berti, V. Cardoso, J. A. Gonzalez, B. Bruegmann, and M. Ansong. Eccentric binary black-hole mergers: The transition from inspiral to plunge in general relativity. *Physical Review D*, 78:064069, 2008.
- [135] Ian Hinder, Birjoo Vaishnav, Frank Herrmann, Deirdre Shoemaker, and Pablo Laguna. Circularization and Final Spin in Eccentric Binary Black Hole Inspirals. *Phys. Rev.*, D77:081502, 2008.
- [136] M. C. Washik, J. Healy, F. Herrmann, I. Hinder, D. M. Shoemaker, P. Laguna, and R. A. Matzner. Binary black hole encounters, gravitational bursts and maximum final spin. *Physical Review Letters*, 101:061102, 2008.
- [137] James Healy, Janna Levin, and Deirdre Shoemaker. Zoom-Whirl Orbits in Black Hole Binaries. 2009.
- [138] James Healy, Frank Herrmann, Ian Hinder, Deirdre M. Shoemaker, Pablo Laguna, and Richard A. Matzner. Superkicks in hyperbolic encounters of binary black holes. *Physical Review Letters*, 102:041101, 2009.
- [139] Birjoo Vaishnav, Ian Hinder, Deirdre Shoemaker, and Frank Herrmann+n. Gravitational waves from eccentric intermediate mass binary black hole+mergers. *Classical and Quantum Gravity*, 26(20):204008, 2009.
- [140] Miguel Alcubierre, Werner Benger, Bernd Bruegmann, Gerd Lanfermann, Lars Nergel, Edward Seidel, and Ryoji Takahashi. The 3d grazing collision of two black holes. *Physical Review Letters*, 87:271103, 2001.

- [141] Masaru Shibata, Hirotada Okawa, and Tetsuro Yamamoto. High-velocity collision of two black holes. *Phys. Rev.*, D78:101501, 2008.
- [142] U. Sperhake et al. Cross section, final spin and zoom-whirl behavior in high-energy black hole collisions. 2009.
- [143] U. Sperhake, V. Cardoso, F. Pretorius, E. Berti, and J. A. Gonzalez. The high-energy collision of two black holes. *Physical Review Letters*, 101:161101, 2008.
- [144] Emanuele Berti et al. Semianalytical estimates of scattering thresholds and gravitational radiation in ultrarelativistic black hole encounters. 2010.
- [145] U. Sperhake et al. Ultra-relativistic grazing collisions of black holes. 2010.
- [146] Roman Gold and Bernd Brügmann. Radiation from low-momentum zoom-whirl orbits. *Class. Quantum Grav.*, 27(084035), 2009.
- [147] James Healy, Pablo Laguna, Richard A. Matzner, and Deirdre M. Shoemaker. Final mass and spin of merged black holes and the golden black hole, 2009.
- [148] Benny Walther, Bernd Brügmann, and Doreen Müller. Numerical black hole initial data with low eccentricity based on post-Newtonian orbital parameters. *Phys. Rev.*, D79:124040, 2009.
- [149] William H. Press, Saul A. Teukolsky, William T. Vetterling, and Brian P. Flannery. Numerical recipes in c: The art of scientific computing. second edition, 1992.
- [150] M. Burgay, N. D’Amico, A. Possenti, R.N. Manchester, A.G. Lyne, B.C. Joshi, M.A. McLaughlin, M. Kramer, J.M. Sarkissian, F. Camilo, V. Kalogera, C. Kim, and D.R. Lorimer. An increased estimate of the merger rate of double neutron stars from observations of a highly relativistic system. *Nature*, 426:531–533, 2003.
- [151] Joey Shapiro Key and Neil J. Cornish. Characterizing Spinning Black Hole Binaries in Eccentric Orbits with LISA. 2010.
- [152] J. Hough. Lisa: Laser interferometer space antenna for gravitational wave measurements. 1994. Prepared for Edoardo Amaldi Meeting on Gravitational Wave Experiments, Rome, Italy, 14-17 Jun 1994.
- [153] Editor B. Schutz. Proceedings of the 3rd international lisa symposium. *Class. Quantum Grav.*, 18:3965–4164, 2001.
- [154] E. S. Phinney. Lisa science requirements. 2002. <http://www.its.caltech.edu/esp/lisa/LISTwg1.req-pr.pdf>.

## Bibliography

- [155] Stanislav Babak, Mark Hannam, Sascha Husa, and Bernard Schutz. Resolving Super Massive Black Holes with LISA, 2008.
- [156] Mark Hannam and Ian Hawke. Numerical relativity simulations in the era of the einstein telescope, 2009.
- [157] Chris Van Den Broeck. Compact binary coalescence and the science case for Einstein Telescope. 2010.
- [158] Nicolas Yunes, K. G. Arun, Emanuele Berti, and Clifford M. Will. Post-circular expansion of eccentric binary inspirals: Fourier-domain waveforms in the stationary phase approximation. *Physical Review D*, 80:084001, 2009.
- [159] Ian Hinder, Frank Herrmann, Pablo Laguna, and Deirdre Shoemaker. Comparisons of eccentric binary black hole simulations with post-Newtonian models. *Phys. Rev.*, D82:024033, 2010.
- [160] Luc Blanchet. Post-newtonian theory and the two-body problem, 2009.
- [161] Gerhard Schafer. Post-newtonian methods: Analytic results on the binary problem, 2009.
- [162] Thibault Damour, Alessandro Nagar, Mark Hannam, Sascha Husa, and Bernd Brügmann. Accurate effective-one-body waveforms of inspiralling and coalescing black-hole binaries. *Phys. Rev.*, D78:044039, 2008.
- [163] T. Cokelaer and D. Pathak. Searching for gravitational-wave signals emitted by eccentric compact binaries using a non-eccentric template bank: implications for ground-based detectors. *Class. Quant. Grav.*, 26:045013, 2009.
- [164] U. Sperhake. Colliding black holes and gravitational waves. *Lect. Notes Phys.*, 769:125–175, 2009.
- [165] U. Sperhake, E. Berti, V. Cardoso, J. A. González, B. Brügmann, and M. Ansong. Eccentric binary black-hole mergers: The transition from inspiral to plunge in general relativity. *Phys. Rev.*, D78:064069, 2008.
- [166] Ulrich Sperhake, Vitor Cardoso, Frans Pretorius, Emanuele Berti, and Jose A. González. The high-energy collision of two black holes. *Phys. Rev. Lett.*, 101:161101, 2008.
- [167] S.W. Hawking. Gravitational radiation from colliding black holes. *Phys. Rev. Lett.*, 26:1344–1346, 1971.
- [168] Mark Hannam, Sascha Husa, Denis Pollney, Bernd Brügmann, and Niall Ó Murchadha. Geometry and regularity of moving punctures. *Phys. Rev. Lett.*, 99:241102, 2007.

- [169] Peter Diener, Frank Herrmann, Denis Pollney, Erik Schnetter, Edward Seidel, Ryoji Takahashi, Jonathan Thornburg, and Jason Ventrella. Accurate evolution of orbiting binary black holes. *Phys. Rev. Lett.*, 96(12):121101, March 30 2006.
- [170] Marcus Thierfelder, Sebastiano Bernuzzi, and Bernd Brügmann. Numerical relativity simulations of binary neutron stars. 2011.
- [171] Jose M. Martí, Jose M. Ibanez, and Juan A. Miralles. Numerical relativistic hydrodynamics: Local characteristic approach. *Phys. Rev.*, D43:3794–3801, 1991.
- [172] Francesc Banyuls, Jose A. Font, Jose M. A. Ibanez, Jose M. A. Martí, and Juan A. Miralles. Numerical 3+1 General Relativistic Hydrodynamics: A Local Characteristic Approach. *Astrophys. J.*, 476:221, 1997.
- [173] J.M. Ibáñez, M.A. Aloy, J.A. Font, J.M. Martí, J.A. Miralles, and J.A. Pons. In E.F. Toro, editor, *Godunov methods: theory and applications*, New York, 2001. Kluwer Academic/Plenum Publishers.
- [174] Eleuterio F. Toro. *Riemann Solvers and Numerical Methods for Fluid Dynamics*. Springer-Verlag, 2<sup>nd</sup> edition, 1999.
- [175] L. Del Zanna, O. Zanotti, N. Bucciantini, and P. Londrillo. ECHO: an Eulerian Conservative High Order scheme for general relativistic magnetohydrodynamics and magnetodynamics. 2007.
- [176] L. Del Zanna and N. Bucciantini. An efficient shock-capturing central-type scheme for multidimensional relativistic flows. I. Hydrodynamics. *Astron. Astrophys.*, 390:1177, 2002.
- [177] A. Harten, B. Engquist, S. Osher, and S. R. Chakrabarty. Uniformly high order accurate essentially non-oscillatory schemes III. *J. Comput. Phys.*, 71:2311, 1987.
- [178] C.W. Shu and S. Osher. Efficient implementation of essentially non-oscillatory shock-capturing schemes, ii. *J. Comput. Phys.*, 83:32–78, 1989.
- [179] C.W. Shu and S. Osher. Efficient implementation of essentially non-oscillatory shock-capturing schemes, i. *J. Comput. Phys.*, 77:439–, 1989.
- [180] H. Nessyahu and E. Tadmor. Non-oscillatory central differencing for hyperbolic conservation laws. *J. Comp. Phys.*, 87:408–463, 1990.
- [181] Alexander Kurganov and Eitan Tadmor. New high-resolution central schemes for nonlinear conservation laws and convection-diffusion equations. *J. Comp. Phys.*, 160:214–282, 2000.

## Bibliography

- [182] Barry Merriman. Understanding the shu-osher conservative finite difference form. *J. Sci. Comput.*, 19(1-3):309–322, 2003.
- [183] A. C. Fabian, J. E. Pringle, and M. J. Rees. Tidal capture formation of binary systems and X-ray sources in globular clusters. *Royal Astronomical Society, Monthly Notices*, 172:15P–+, August 1975.
- [184] William H. Lee, Enrico Ramirez-Ruiz, and Glenn van de Ven. Short gamma-ray bursts from dynamically-assembled compact binaries in globular clusters: pathways, rates, hydrodynamics and cosmological setting. *Astrophys. J.*, 720:953–975, 2010.
- [185] I. Kowalska, T. Bulik, K. Belczynski, M. Dominik, and D. Gondek-Rosinska. The eccentricity distribution of compact binaries. *Astronomy & Astrophysics*, 527:A70+, March 2011.
- [186] Kent Yagi and Naoki Seto. Detector configuration of DECIGO/BBO and identification of cosmological neutron-star binaries. *Phys. Rev.*, D83:044011, 2011.
- [187] Branson C. Stephens, William E. East, and Frans Pretorius. Eccentric Black Hole-Neutron Star Mergers. 2011.
- [188] C. W. Lincoln and C. M. Will. Coalescing binary systems of compact objects to (post)<sup>5/2</sup>-Newtonian order: Late-time evolution and gravitational-radiation emission. *Phys. Rev. D*, 42:1123–1143, 1990.
- [189] J. P. A. Clark and D. M. Eardley. *Astrophys. J.*, 215:311, 1977.
- [190] B. Mashhoon. Tidal Gravitational Radiation. *Astrophysical Journal*, 185:83–86, October 1973.
- [191] B. Mashhoon. Tidal radiation. *Astrophysical Journal*, 216:591–609, September 1977.
- [192] Dong Lai and Yanqin Wu. Resonant Tidal Excitations of Inertial Modes in Coalescing Neutron Star Binaries. *Phys. Rev.*, D74:024007, 2006.
- [193] L. Bildsten and C. Cutler. *Astrophys. J.*, 400:175, 1992.
- [194] Keisuke Taniguchi, Thomas W. Baumgarte, Joshua A. Faber, and Stuart L. Shapiro. Black hole-neutron star binaries in general relativity: effects of neutron star spin. *Phys. Rev. D*, 72:044008, 2005.
- [195] William H Lee and Enrico Ramirez-Ruiz. The progenitors of short gamma-ray bursts. *New Journal of Physics*, 9(1):17, 2007.
- [196] Stephen D. H. Hsu. The QCD phase diagram and explosive astrophysics. 2001.

## Acknowledgments

I would like to thank Bernd Brügmann for his thorough supervision and the introduction to this fascinating topic. The freedom he gave me has enabled me to also learn about aspects of numerical relativity that are not directly related to the work in this thesis. In particular, I am grateful for many useful and insightful discussions.

It is a pleasure to express my gratitude to David Hilditch for many interesting discussions on hyperbolicity, well-posedness and the implications for numerics. With the knowledge and experience he shared with me in these numerous, informal discussions he had a large impact on the way I think about my work. I always appreciate his constructive criticism and advice.

Many thanks to Sebastiano Bernuzzi whose comments and suggestions substantially improved my thesis. With his ideas and support for initial data and interpretation of matter spacetimes he enabled me to progress faster.

I would like to thank Pablo Galaviz, Marcus Thierfelder and Doreen Müller for their support regarding the BAM code.

Further gratitude goes to Frans Pretorius who hosted me at Princeton University. I had a great research stay and found the discussions with him most helpful. His idea to study eccentric neutron star binaries revealed fascinating physics, which he foresees long before the project had begun.

I express many thanks to Ulrich Sperhake for many discussions, for answering various questions and requests at the earliest instant. I highly appreciate his attitude and commitment to share his ideas and experiences.

I am very grateful to the DFG research grant for providing financial support, which allowed me to attend many interesting international conferences.

I am very grateful to the Graduate School "Quantum- and Gravitational Fields", in particular for their financial support, which enabled my research stay at Princeton University.

I thank my wife for her continued support.

Finally, my gratitude goes to my parents for their encouragement and enthusiasm for what I am doing.





# Ehrenwörtliche Erklärung

Ich erkläre hiermit ehrenwörtlich, dass ich die vorliegende Arbeit selbstständig, ohne unzulässige Hilfe Dritter und ohne Benutzung anderer als der angegebenen Hilfsmittel und Literatur angefertigt habe. Die aus anderen Quellen direkt oder indirekt übernommenen Daten und Konzepte sind unter Angabe der Quelle gekennzeichnet. Auch die Ergebnisse, die in Zusammenarbeit mit den Mitgliedern des Lehrstuhles für Quantenfeldtheorie in Jena und anderen Kooperationen entstanden sind, sind in der Arbeit entsprechend benannt.

Weitere Personen waren an der inhaltlich-materiellen Erstellung der vorliegenden Arbeit nicht beteiligt. Insbesondere habe ich hierfür nicht die entgeltliche Hilfe von Vermittlungs- bzw. Beratungsdiensten (Promotionsberater oder andere Personen) in Anspruch genommen. Niemand hat von mir unmittelbar oder mittelbar geldwerte Leistungen für Arbeiten erhalten, die im Zusammenhang mit dem Inhalt der vorgelegten Dissertation stehen. Die Arbeit wurde bisher weder im In- noch im Ausland in gleicher oder ähnlicher Form einer anderen Prüfungsbehörde vorgelegt.

Die geltende Promotionsordnung der Physikalisch-Astronomischen Fakultät ist mir bekannt.

Ich versichere ehrenwörtlich, dass ich nach bestem Wissen die reine Wahrheit gesagt und nichts verschwiegen habe.

Jena, 20.6.2011

Roman Gold



# Curriculum vitae, Roman Gold

## Personal

- Born on July 10th, 1981
- Married

## Education

- 2011/02 - 2011/04: Research stay at Princeton University (collaboration with Prof. Frans Pretorius)
- 2008/08 - 2011/07: PhD student in Physics at the University of Jena, advisor: Prof. Bernd Brügmann
- 2008/07 : Diploma in physics (grade "very good") at the University of Heidelberg  
Diploma thesis on "MHD-turbulence in accretion disks around black holes"
- 2002/10 : Beginning of physics studies at the University of Heidelberg
- 2001/08 - 2002/07: Civil service
- 2001/07 : Graduation from High School, Oberursel, Germany

## Publications

- R. Gold and B. Brügmann,  
"Low-momentum zoom-whirl orbits of black hole binaries,"  
Journal-ref: Class.Quant.Grav.27:084035,2010  
arXiv:0911.3862 [gr-qc].
- R. Gold and B. Brügmann,  
"Eccentric black hole binaries, zoom-whirls and gravitational radiation in full GR,"  
in preparation, to be submitted to Phys. Rev. D.

## Teaching experience

- University of Jena
  - Tutorial on Relativistic Physics (Winter terms 2008,2009,2010)
  - Course on "Astrophysics and black holes" for schoolgirls (2010)
- University of Heidelberg
  - Tutorial on Relativistic Astrophysics (2008)

## Schools and conferences

- Midwest Relativity Meeting (Guelph, Canada, November 2010)
- GR19 conference (Mexico City, Mexico, July 2010)
- DPG spring conference (Bonn, Germany, Spring 2010)
- Workshop of the Research Training Group "Quantum- and gravitational fields" (Oppurg, Germany, 2009)
- 12th Marcel Grossman meeting (Paris, France, July 2009)
- 8th Edoardo Amaldi conference (New York, USA, June 2009)
- Several semi-annual SFB/TR7 meetings (Jena/Garching/Hannover/Potsdam/Tübingen, Germany, 2009/10)
- DPG spring conference (Munich, Germany, Spring 2009)
- Modelling of astrophysical sources of gravitational radiation (Valencia, Spain, 2008)
- Post-Newton 2008 (Jena, Germany, 2008)
- Heidelberg Graduate Days (2007)

## Talks

- "Radiation properties of eccentric black hole binaries"  
(GR19, Mexico, July 2010)
- "Zoom-whirl orbits of binary black holes"  
(12th Marcel Grossman Meeting, Paris, July 2009; 8th Edoardo Amaldi Conference, New York, June 2009; SFB/TR7 semi-annual meeting 2009; DPG Spring Conference, Munich, March 2009)
- "Zoom whirl orbits and eccentric black hole binaries"  
(Midwest Relativity Meeting, Guelph, November 2010)
- "Phase space of eccentric black hole binaries" (DPG Spring Conference, Bonn, March 2010; Graduate School Workshop, Oppurg, October 2009; )